AN ABSTRACT OF THE THESIS OF

Paul H. Ruscher for the degree of Doctor of Philosophy in Atmospheric Sciences presented on October 2, 1987.

Title: An Examination of Structure and Parameterization of Turbulence in the Stably-Stratified Atmospheric Boundary Layer

Abstract approved: Redacted for Privacy

The very stable boundary layer is a region of the atmosphere typified by large vertical gradients of temperature and momentum. Analysis of very stable atmospheric flows is complicated by the presence of nonlinear interactions among gravity waves, shear-driven overturning circulations, two-dimensional vortical modes and intermittent turbulence in various stages of development. This study examines the horizontal structure of a very stable atmospheric boundary layer, using data obtained primarily from terrain-following aircraft flights over central Oklahoma.

Several diagnostic procedures are applied to the aircraft data, including classical and rotary spectral analysis, principal component analysis, and structure functions. Coherent structures with sharp boundaries are examined with a new conditional sampling technique which requires little *a priori* specification of sampling criteria. Because the flows involve sharp boundaries, spectral techniques do not provide as much useful information as other more localized procedures. The edges of the coherent structures are regions of significant vertical heat transport, a feature not often emphasized in studies of gravity waves and vortical modes in the stable boundary layer.

The presence of significant turbulence even for large stability has implications for modelling of the very stable boundary layer. Forecasts of minimum temperature, boundary layer height, inversion characteristics, and pollutant dispersal are all significantly affected by turbulent mixing. Many models of the stable boundary layer artificially arrest the mixing under stable conditions, resulting in, for example, overestimates of nocturnal cooling. A new parameterization of the stable boundary layer is studied here by incorporating it into an existing model of the planetary boundary layer. The model is then run with one-dimensional sensitivity tests for an idealized atmosphere and with data from Wangara day 33. A simulation over snow cover is also examined. The tests substantiate the role of vertical mixing in ameliorating nocturnal cooling. An additional improvement is a more realistic boundary layer height for moderate wind speeds.

An Examination of Structure and Parameterization of Turbulence in the Stably-Stratified Atmospheric Boundary Layer

by

Paul H. Ruscher

A THESIS
submitted to
Oregon State University

in partial fulfillment of
the requirements for the
degree of

Doctor of Philosophy

Completed October 2, 1987
Commencement June 1988

APPROVED:

Redacted for Privacy

Professor of Atmospheric Sciences in charge of major

Redacted for Privacy

Chairman of Department of Atmospheric Sciences

Redacted for Privacy

Dean of Graduate School

Date thesis is presented October 2, 1987

Acknowledgements

This success of this research can be attributed in large part to the guidance of my advisor and friend, Larry Mahrt. Without his dedication, patience, understanding, and assistance, this research could not have been completed. I would also like to thank two other faculty members who provided a great deal of help along the way, Hua-Lu Pan and Steven Esbensen. I thank also the other members of my committee, Profs. Grigsby, Murphy, and Laursen for their suggestions on improving the final manuscript.

Thanks also go to Jim Deardorff, who provided the spark which got me involved in boundary layer research. Yochanan Kushnir and Nimal Gamage were often available for helpful information. Michelle Burrier provided some assistance in preparation of the final manuscript. Computer programming and graphics assistance was provided along the way by Bill McKie and Wayne Gibson. Early computations were carried out at the Climatic Research Institute (PDP 11/70); the use of these facilities were made available to me by its director, Prof. Larry Gates. Other computations were made on the CRAY computers at the National Center for Atmospheric Research (NCAR), which is supported by the National Science Foundation (NSF). Most of all, I would like to thank my wife, Donna, and children for their sacrifice — a great deal of time went into this research that was, by all rights, theirs.

Support for this research was provided by NSF grant ATM8306141 and contract F-19628-84-K-0044 from the Air Force Geophysics Laboratory. The Departments of Meteorology at Texas A & M University and Florida State University and the Department of Atmospheric Sciences at Creighton University also provided facilities for my research while I was away from Corvallis.

Table of Contents

Table of Contents/continued Page

List of Figures

List of Tables

An Examination of Structure and Parameterization of Turbulence in the Stably-Stratified Atmospheric Boundary Layer

Paul H. Ruscher

Chapter I

Introduction

There have been many investigations into the structure of the planetary boundary layer (PBL). Most of the theoretical work done in turbulence dynamics involves homogeneous, stationary turbulence over relatively flat terrain. The stability characteristics of the boundary layer are often discussed in terms of the vertical gradient of potential temperature (θ), defined as

$$\theta \equiv T \left(\frac{p_o}{p} \right)^{\kappa} , \tag{1}$$

where T is the air temperature, p is atmospheric pressure, p_o is a reference pressure, usually taken to be 100 kPa, and κ is the ratio of the gas constant for dry air (R_d = 287 J kg^{-1} K^{-1}) to the specific heat of air at constant pressure (c_p = 1004 J kg^{-1} K^{-1}). The classification of the unsaturated boundary layer based on vertical gradients of mean potential temperature is as follows:

$$\frac{\partial \theta}{\partial z} \begin{cases} > 0 , & \text{stable} \\ = 0 , & \text{neutral} \\ < 0 , & \text{unstable} \end{cases} . \qquad (2)$$

Through a process known as convective adjustment, unstable temperature gradients are not maintained for very long in the atmosphere except near the surface, and we can usually restrict our attention to two types of boundary layers—the near-neutral boundary layer, which is well mixed by heating and/or mechanical mixing, and the stable boundary layer, in which potential temperature increases with height and vertical motion is suppressed. A better criteria involves classification based on the direction of the vertical heat flux, which gives a big difference between the neutral and heated boundary layer.

The convective boundary layer (CBL) has been studied most thoroughly. The NBL is often studied in terms of cold-air drainage (Blumen, 1984), the nocturnal jet (Thorpe and Guymer, 1977), and accumulation of air pollutants (Lamb, 1982). When the boundary layer is stably-stratified, the depth of the boundary layer is usually quite shallow, yet vertical gradients are much larger than for the convective case (Caughey, 1982).

The governing dynamics of the stable boundary layer (SBL) are indeed quite different from the factors which control development and growth of the CBL. The CBL's growth is due to positive surface heat flux. Turbulence in the CBL is usually quite anisotropic and thermals are numerous (Lenschow and Stephens, 1980). These thermals are buoyantly-driven warm updrafts which transport heat upwards (one example for which the vertical heat flux is postive) and serve as the primary mixing mechanism.

The turbulent kinetic energy equation is quite useful for studying the dynamics of the vertical structure of the boundary layer. The equation governing the time evolution of the turbulence kinetic energy (TKE) per unit mass is

$$\frac{\partial \bar{e}}{\partial t} + \overline{U_j}\frac{\partial \bar{e}}{\partial x_j} = \delta_{i3}\frac{g}{\overline{\theta_v}}\overline{u_j'\theta_v'} - \overline{u_i'u_j'}\frac{\partial \overline{U_i}}{\partial x_j} - \frac{\partial(\overline{u_j'e})}{\partial x_j} - \frac{1}{\overline{\rho}}\frac{\partial}{\partial x_j}\overline{u_j'p'} - \varepsilon \quad , \tag{3}$$

where the Einstein notation is used for implied summation over repeated indices (i, j = 1,2,3). The first term on the left of (3) is the time rate of change of TKE, where the TKE is defined as

$$\bar{e} \equiv \frac{1}{2}(\overline{u_i'^2}) \, . \tag{4}$$

The second term is advection of TKE by the mean wind. The first term on the right hand side is the buoyancy production term; Kronecker's delta is used here to indicate this terms contribution to TKE changes for the vertical velocity component only (δ_{i3} = 1 if i=3, 0 otherwise). The next term is the mechanical production term, followed by the redistribution term, also called the divergence of turbulent flux term. The term involving the correlation of pressure with velocity components is a term thought to be important particularly in wave fields (Carruthers and Hunt, 1986, Zhou *et al.*, 1985) and in microfront zones (Schols and Wartena, 1986). Finally, ε represents the turbulence dissipation rate.

Usually additional assumptions are made before carrying out such a budget study, including (*i*) only variations in the vertical are allowed, i.e., the turbulent flow is horizontally homogeneous and (*ii*) subsidence is neglected. An analysis of the TKE budget for the CBL typically shows generation of TKE by buoyancy and TKE destruction by transport and dissipation (Caughey and Wyngaard, 1979). The shear generation term is often dominated by the buoyancy generation, but there is quite a lot of variation in the TKE budget, depending on the environmental conditions (Caughey, 1982).

In the case of the SBL, mechanical production of TKE by the shear generation term is balanced and sometimes overwhelmed by buoyancy *destruction*; there usually exists a downward (negative) heat flux. As previously mentioned, the depth of the SBL is usually

quite shallow and fluxes are quite weak, making them more difficult to measure. Complicating the analysis of the turbulence are buoyancy (internal gravity) waves[1] which are often present in the SBL (Busch *et al.*, 1969), because of their own non-linear interactions and their interactions with the turbulence. Attempts to quantify these interactions have been successful on occasions only when the gravity waves are particularly strong and fit the linear theoretical model (Axford, 1971, Caughey and Readings, 1975, Finnigan and Einaudi, 1981).

Waves may break via Kelvin-Helmholtz instability into turbulent patches, which may then decay into two-dimensional turbulence or fossil turbulence (Woods *et al.*, 1969). Evidence for this type of wave breaking in the atmosphere comes from observations (Gossard and Hooke, 1975; Fuà et al., 1982) and numerical simulations (Tanaka, 1975; Weinstock, 1984). In addition, the effects of the underlying topography on the stratified flow can not be ignored, but assessment of its effects are uncertain.

While in the CBL, turbulence is usually organized by thermals, the SBL plays host to a multitude of phenomena, often acting on the same spatial scales. In addition to the simple linear gravity waves types and nonlinear waves mentioned above, regions of active turbulence may be present under significant stratification, with the turbulence being organized by transverse modes or longitudinal modes (Eymard, 1984; Shirer, 1986). Two dimensional turbulence is the complementary mode to the gravity wave mode in the analysis of Lilly (1983); in his analysis and also the calculations of Riley *et al.* (1981); the energy is equally-partitioned between the two modes. The presence of this two dimensional vortical mode if often overlooked by investigators (Müller *et al.*, 1986).

In an analysis of the interaction between buoyancy waves and stably-stratified flow in the PBL, Einaudi and Finnigan (1981) describe three primary mechanisms through which turbulence and waves interact. When nonlinear waves exist in the fluid, wave

[1]In accordance with the discussion of Gossard and Hooke (1975), I will sometimes use the less common but more logical terminology of buoyancy waves when referring to internal gravity waves.

breaking may occur, forming patches of turbulence. If shear layers are present in the PBL (as is often the case for stable stratification), additional waves may be generated at the level of the shear via Kelvin-Helmholtz instability (Turner, 1979) which have a smaller scale than the main or background gravity wave. In addition, convective instability due to overturning in the wave may occur.

In most studies of turbulence, the variables are partitioned into a mean and fluctuating part of the flow, so that

$$\varphi \equiv \bar{\varphi} + \varphi' \quad , \tag{5}$$

where φ may represent any variable. Einaudi and Finnigan, however, partition the flow into three parts: a mean flow (which can also interact with the wave field); a periodic component (the waves, represented by a tilde); and the turbulent component, so that

$$\varphi = \bar{\varphi} + \varphi' + \tilde{\varphi} \quad . \tag{6}$$

The last two terms of (6) comprise the fluctuating part of the flow (i.e., φ' in Eq. 5). This partition was successful because in each case there was a regular structure present in the boundary layer which organized the motion so that compositing brought out the dynamics of the structure (represented by the $\tilde{\varphi}$ in Eq. 6) quite well.

Finnigan and Einaudi (1981), in a separate paper, describe the effects that the waves have on the turbulence. Although heat and momentum fluxes are an order of magnitude larger for the turbulent part of the flow than for the periodic part, there is substantial interaction between the different scales which can not be neglected. Much of their work has been substantiated in another study of conditions at the Boulder Atmospheric Observatory 300 m tower (Finnigan *et al.*, 1984). Such interactions also occur in the surface layer of the ocean, as well, as documented extensively by Kitaigorodskii *et al.* (1983).

Spectral analysis is the traditional data analysis technique we can utilize to both make inferences about the physical processes occurring in the atmosphere and to compare

data with previous studies. Several papers have appeared in the last twenty years extolling the virtues of spectral analysis as a tool to separate buoyancy waves from turbulence (Busch *et al.*, 1969; Stewart, 1969; Fleer, 1983; de Baas and Driedonks, 1985; Dewan, 1985). The presence of a gap in the spectrum should be considered a prerequisite to relying solely on spectral analysis for interpretation purposes. The kinetic energy spectrum of the atmosphere has been studied quite extensively for a broad range of scales. In a fairly recent paper, Lilly (1983) sought to explain the behavior of the spectra of kinetic energy on scales of mesoscale phenomena. His work is an extension of Gage's (1979), which attempted to explain how three-dimensional turbulence in the presence of stratification is vertically suppressed, hence becoming effectively two-dimensional turbulence.

A well-established model of turbulence spectra exists which breaks down the total spectra of velocity and scalar components into three regions or scales (e.g., Panofsky and Dutton, 1984). The dissipation subrange is that part of the spectrum in which scales are smaller than the Kolmogorov microscale and controlled by viscosity. At the low-wave number end, the energy-containing subrange is found, where large eddies develop from instability of the mean shear. Here typical length scales are on the order of tens of meters to kilometers. In the intermediate inertial subrange, where energy is cascaded from low wave numbers (energy-containing range) down toward higher wave numbers (dissipation range), kinetic energy (~S(k)) depends on scale according to the relationship

$$S(k) = a\ \varepsilon^{2/3}\ k^{-5/3}\ , \tag{4}$$

where k is the wavenumber in the direction of the mean wind, ε is the energy dissipation rate, and a is a constant $O(1)$. For isotropic turbulence, the value of a for lateral velocity components (orthogonal to the mean flow) is $^4/_3$ times the value for longitudinal velocity components. Eq. 4 states the well-known $-^5/_3$ power law for microscale motions in the atmosphere.

While energy cascades down to smaller scales throughout the microscale portion of atmospheric motion, in the macroscale (wavelengths > 1000 km) portion of the spectrum

we find that energy may cascade upscale, while enstrophy (defined as mean-square vorticity) cascades down to smaller scales (Lilly, 1983). The mesoscale part of the total spectrum has been explained and is also upscale, as with larger macroscale transfer. In the macroscale, the dependence on wavenumber is $k^{-5/3}$, while in the mesoscale part, it has been observed to fall near k^{-3} (Gage, 1979).

Not yet mentioned is the presence (or absence) of the so-called buoyancy subrange, that part of the spectrum where buoyancy forces play a controlling influence on the turbulence. The existence of a buoyancy subrange depends on fully-turbulent flow with substantial work being done against gravitational forces. It is found at the low wavenumber end of the inertial subrange and involves transfer of TKE to turbulent potential energy. Two somewhat different theoretical treatments are presented by Bolgiano (1959, 1962), who predicts a spectral slope of $k^{-11/5}$, and Turner (1979), who predicts a slope of k^{-3} for velocity components.

In the literature, some papers have related three-dimensional turbulent decay, two-dimensional turbulence, fossil turbulence and stratification. Unfortunately, the turbulence textbooks do not generally contain adequate treatments of the interaction between turbulence and other phenomena of similar scale. In Panofsky and Dutton (1984), only two paragraphs are given to the treatment of the interaction between turbulence and low-frequency motions, tentatively identified as gravity waves. In Tennekes and Lumley (1972), we find the following (p. 99):

> N is called the Brunt-Väisälä frequency; it is the frequency of gravity waves in a stable atmosphere. In an unstable atmosphere, gravity waves are unstable and break up into turbulence.

The above quotation may mislead the reader on two counts. Firstly, N is the *upper* limit to the frequency of the buoyancy waves which are occurring in the fluid; it is rarely the case that there is even one dominant wave mode taking place in the boundary layer. Secondly, one of the major problems we have in analyzing stratified turbulence is that

waves may break in the stable PBL, too, into patches of turbulence. A good but now dated treatment is found in an earlier text (Lumley and Panofsky, 1964), while the discussion of Caughey (1982) includes a fairly detailed discussion of linear gravity waves.

Most of the discussion to this point has concentrated on the distinction between waves and turbulence. Unfortunately, not much work has appeared in the literature on the dynamics of the other structures likely to be found in the stable boundary layer. This is easy to understand in light of the tremendous expense involved in studies of stable layer turbulence; measurements made with enought accuracy and for enough observations to prevent sampling errors present formidable barriers. While similarity theory has played an important role in the understanding of the convective and surface layer, a theory known as local similarity theory is gaining renewed attention in recent years (Nieuwstadt, 1984; Holstag and Nieuwstadt, 1986; Sorbjan, 1987), and appears to be able to model the vertical structure of the weakly stable boundary layer quite well.

Just as there a large number of stability parameters which are used in characterizing the atmosphere's potential for generation of severe convective storms, there are many which can be used in boundary layer studies. In air pollution studies, the Pasquill or Turner stability classes are often used (Panofsky and Dutton, 1984). However, a variable which is of more use for classification of boundary layer stability is the Richardson number; recently it has seen more widespread use in studies of atmospheric dispersion (e.g., Wratt and Homes, 1984). It is also widely used for prediction of clear-air turbulence (CAT), and is gaining acceptance in severe convection situations, as well. There are many forms, including the flux, layer, and bulk forms. The flux form is simply the ratio of the buoyancy term to the shear-generation term in the TKE equation (3). The other forms applicable to this study will be defined and used later in chapters III and VI. Another form exists called the radiation Richardson number (Mahrt and Ek, 1984) which will not be used here.

This study will focus on the horizontal structure of coherent structures of the very

stable boundary layer. The data under consideration is largely from one morning during the period immediately after sunrise, but before net positive heating develops. Chapter II contains a description of the experimental conditions under which the data was collected, and a discussion of the large-scale weather patterns immediately preceeding and coincident with the boundary layer data collection. The boundary layer vertical structure is briefly discussed. In chapter III, the data analysis procedures are described, and the results from spectral analysis and principal component analysis are presented and compared.

In order to better understand the dynamics of the very stable layer, the flow is studied by collecting samples from the original data set, based on the observation that there seems to be kind of coherent or repeating structure present in the data. In chapter IV, a new conditional sampling technique is developed, and the samples are composited. The composites illustrate some of the characteristics of the structure, but some characteristics are unavoidably smoothed over, as we might expect for intermittent turbulent flow. Chapter V is an attempt to analyze some of the individual samples which have particularly strong boundaries and sharp zones of transition. Despite the strong stratification, significant vertical transport is seen to occur; this has implications for modelling efforts.

In the very stable boundary layer, the turbulence flux is more associated with the *edges* of the two-dimensional eddies and not the entire region occupied by them. This turbulence is very small scale and may lead to net turbulent flux even if the Richardson number is large. This suggests that models allow for turbulent transport even if the stability is large; also the models can not resolve such small-scale turbulence, which implies that the parameterizations be kept simple. The very stable case is important as it represents conditions where some of the most significant weather associated with synoptic-scale high pressure systems occurs, for example cold minimum temperatures (early frosts in fall, for instance) and severe air pollution episodes, where the suppression of turbulence keeps pollutants near their source.

Motivated by these and other observations and recent theoretical developments, an

existing model of the PBL is modified to improve the treatment of turbulence in the stable boundary layer. Finally, concluding remarks and suggestions for further research are to be found in chapter VII.

Chapter II

Presentation of Data

1. Project SESAME/Nocturnal Boundary Layer

During the spring of 1979, an atmospheric experiment entitled the Severe Environmental Storms and Mesoscale Experiment (SESAME; Alberty *et al.*, 1979) was conducted with the cooperation of many federal agencies and universities. The broad purpose of this study was to obtain a large amount of atmospheric data in the mesoscale space and time domain; that is data which will adequately describe atmospheric phenomena whose features extend from about 2 km in size up to 2000 km in size (Orlanski, 1975) and whose lifetimes range from about 1 hour up to a couple of days.

The project has produced extremely valuable data in particular on severe convection and mesoscale atmospheric structure (e.g., Vincent and Homan, 1983; Fuelberg and Meyer, 1984; Keyser and Carlson, 1984). Although the major emphasis of the project, centered in Oklahoma, was the collection and analysis of data in severe storm situations, an experiment was carried out from 4-6 May to study the NBL during fair and pre-severe weather evenings and mornings.

Figure 2.1 shows the SESAME storm-scale domain, and includes the sites for the data collection. The important locations include the Ft. Sill Military Reservation, where a tethered balloon was in operation, collecting mean profiles of boundary layer wind, temperature, and moisture. Radiosoundings were also carried out from this and other locations on the map. The surface automated mesonetwork was centered about Hinton, Oklahoma, and consisted of 27 stations. Doppler radar was only available for severe-storm or other interesting precipitation events and is not available for analysis of clear-air situations in this experiment.

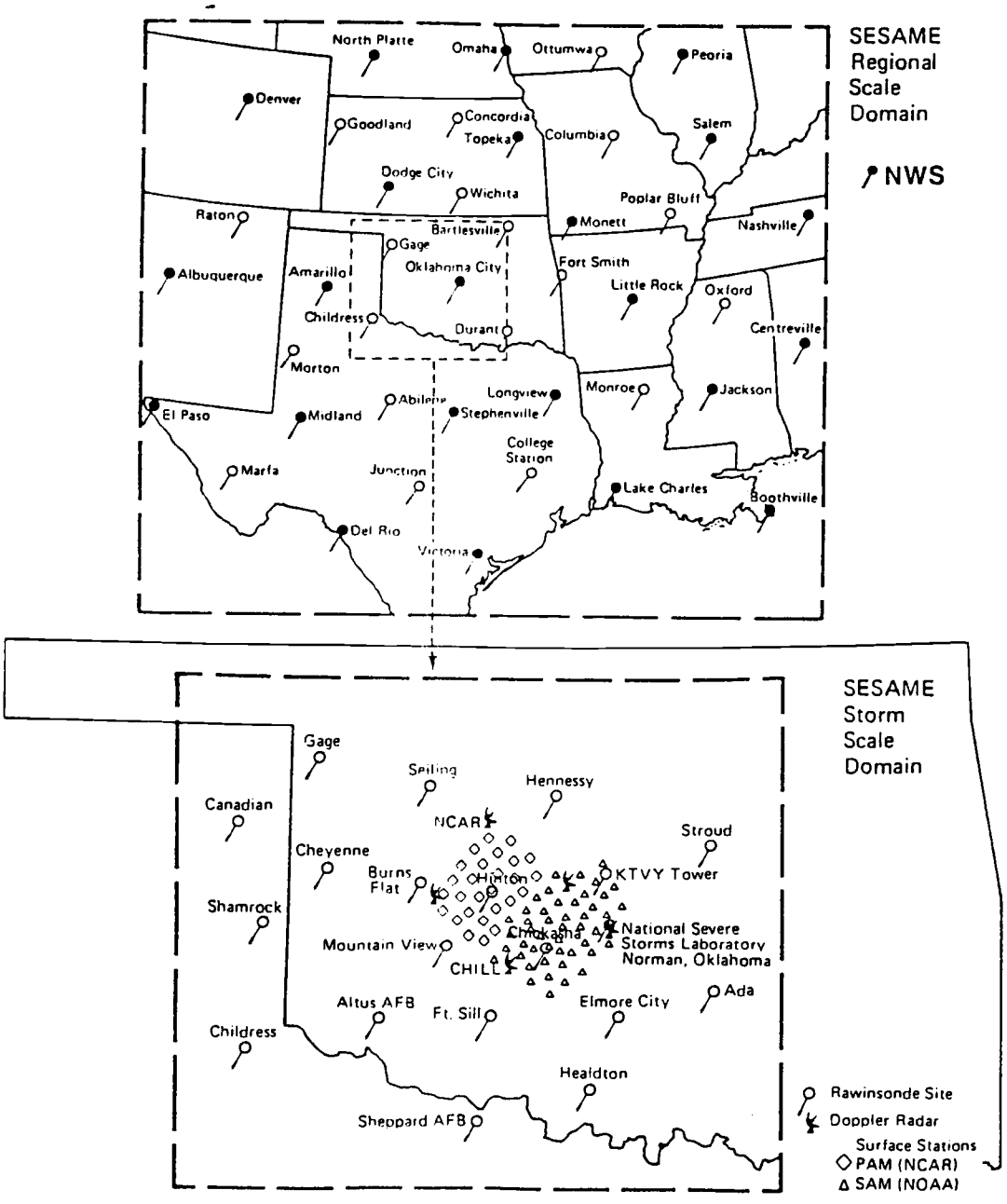

Figure 2.1. SESAME regional scale and storm-scale experimental domains (from Barnes, 1979).

On 2 May, a cold front approached the region from the northwest, triggering severe convection which included large hail, six tornadoes, strong straight-line winds, and heavy rains. After the cold front passed through the storm-scale region, it slowed substantially and produced a period of overrunning precipitation in central Oklahoma that persisted for nearly 48 hours after precipitation began. Over the three day period from 2-5 May, Oklahoma City received 3.41" of rainfall, a very typical value for stations within the region. As the large area of precipitation moved southeastward on the 4th of May, high pressure gradually began to develop over the area and the NBL experiment began on the evening of the 4th. By the morning of 5 May, high pressure was well-established just to the south of the SESAME domain (fig. 2.2), allowing for significant nocturnal cooling. By morning, temperatures in the region were below 5°C as the surface winds were quite weak due to the close proximity of the high pressure system. The PAM stations suggested the presence of significant drainage flow, as we would expect with clear skies and weak ambient wind. The tethersonde soundings for the morning of 5 May indicated substantial directional shear with weak winds in the boundary layer (fig. 2.3); a pronounced surface-based temperature inversion is also noted.

By late on the fifth of May, the high pressure had begun to move eastward and an upper level trough was being established over the western United States. A pronounced nocturnal jet developed over central Oklahoma during the night, with winds at 3000 ft MSL (above mean sea level) from the Mountain View radiosonde reported at 52 kt by 0500 CST. The sounding from Ft. Sill indicated winds of about 37 kt at the same time. Figure 2.4 shows the national surface chart from the morning of 6 May. The presence of significant synoptic-scale forcing drastically altered the character of the nocturnal boundary layer observed on this second morning of SESAME NBL. With the large increase in ambient wind, drainage flow was not established at the surface. Whereas the depth of the NBL was only about 60 m on 5 May, it was about 300 m on 6 May (fig. 2.5). The inversion on 5

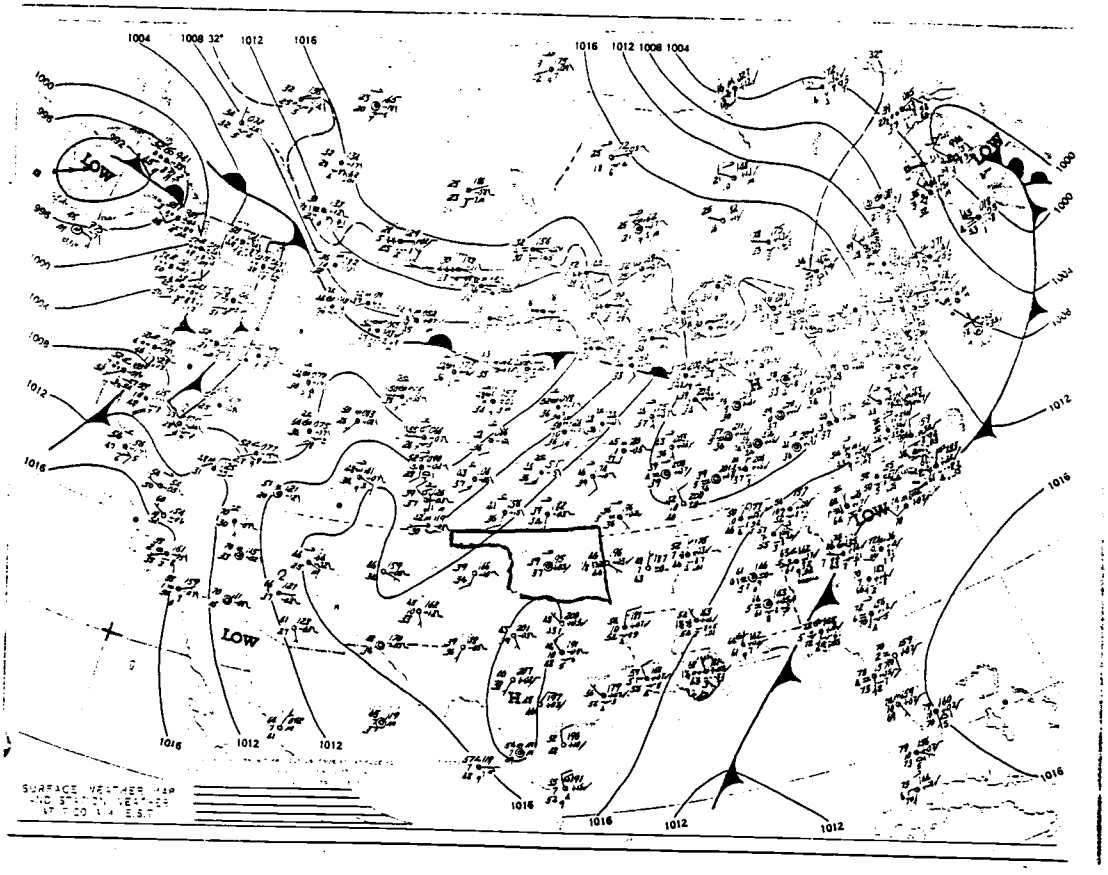

Figure 2.2. Surface chart and sea-level isobaric analysis for 1200 GMT on 5 May 1979.

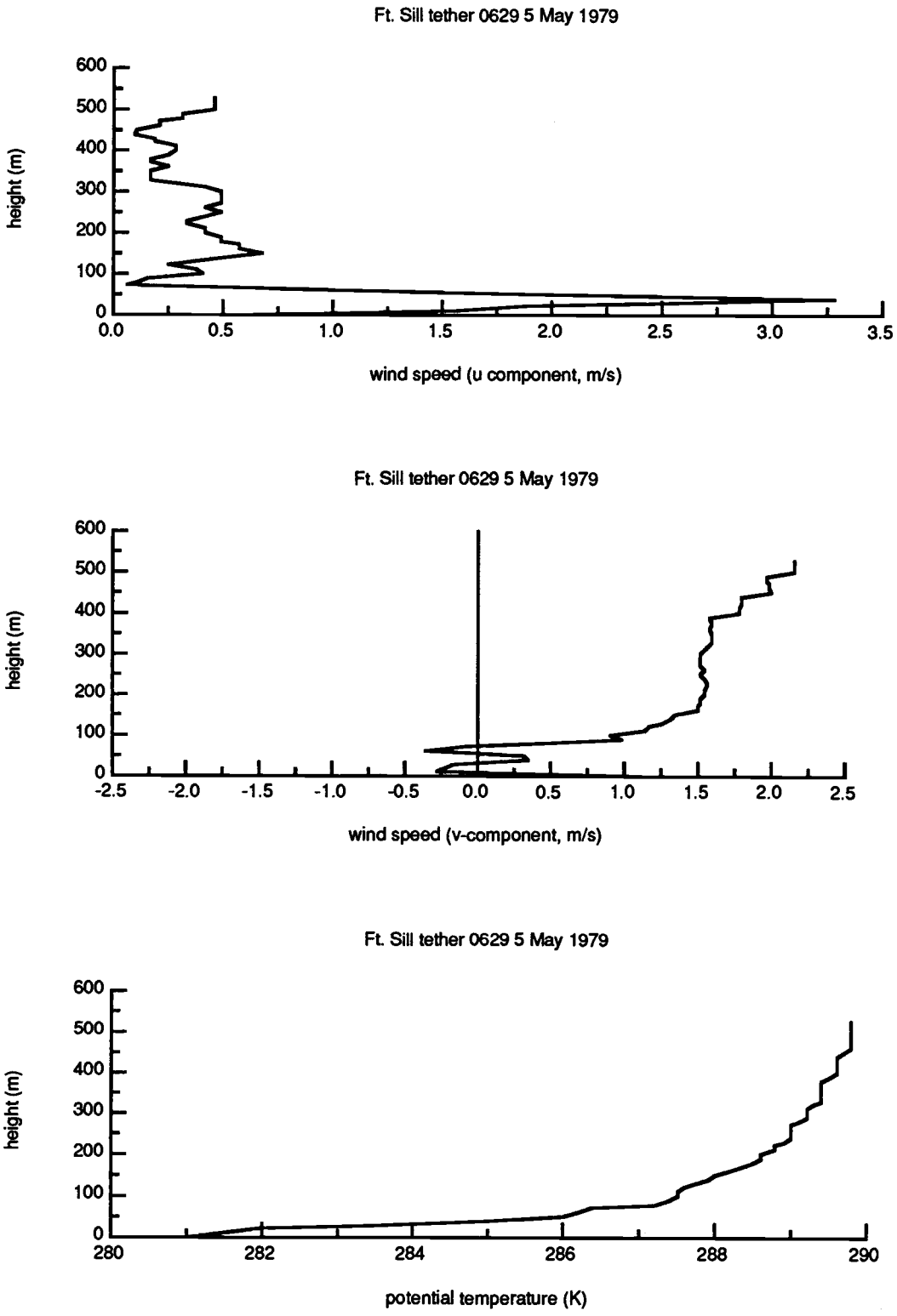

Figure 2.3. Vertical profiles from the Ft. Sill tethersonde at 1129 GMT on 5 May 1979.

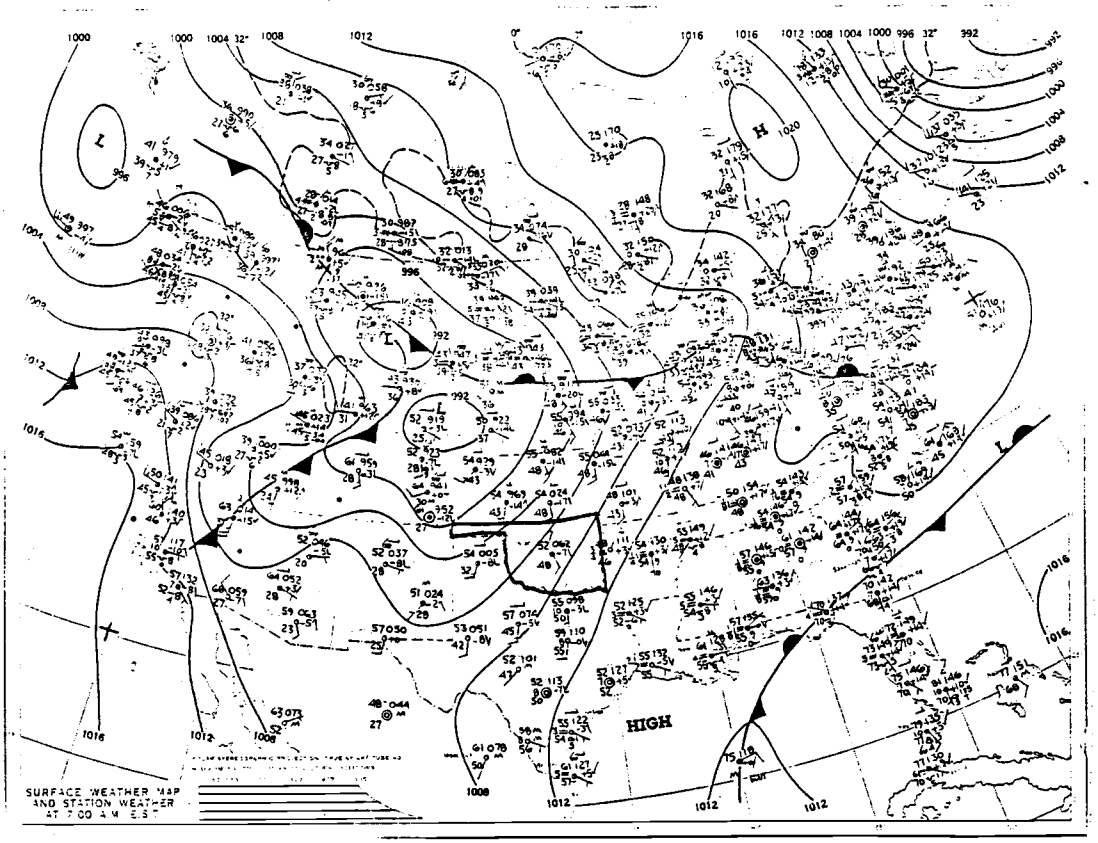

Figure 2.4. As in Figure 2.2 but for 6 May 1979.

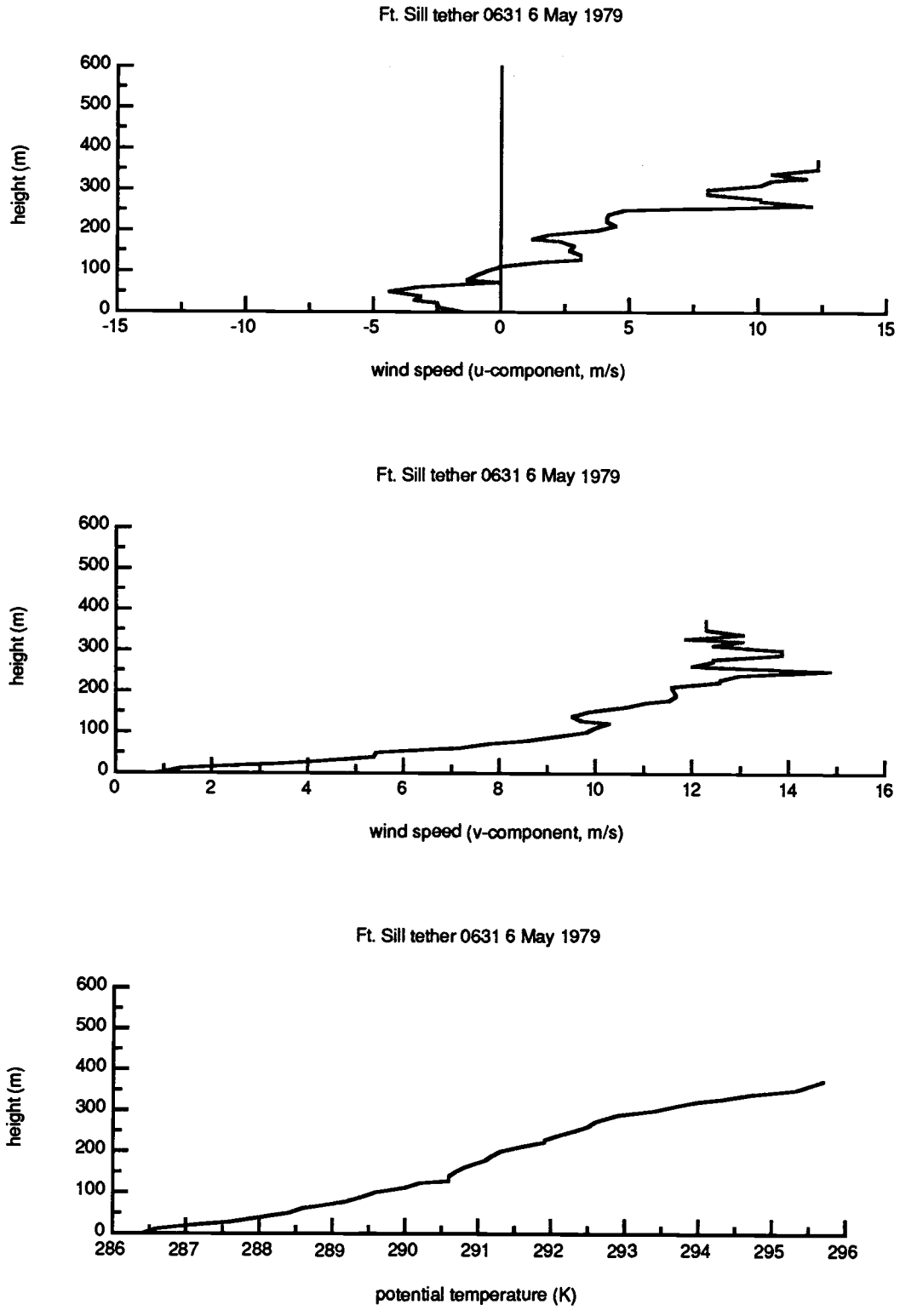

Figure 2.5. Vertical profiles from the Ft. Sill tethersonde at 1131 GMT on 6 May 1979.

May is characterized by a directional shear zone, while significant directional and speed shear are both present on the following morning. The NBL experiment ended as the stong upper level trough moved closer, ultimately spawning more severe weather on 9 May.

An acoustic sounder was also in opeartion at Ft. Sill during the NBL experimental phase (fig. 2.6). The sounder is particularly well-suited for descriptions of the structure of the cloud-free turbulent boundary layer; velocity and temperature fluctuations scatter sound waves. Many dynamical features of the SBL have been revealed by a variety of remote sensing devices such as the acoustic sounder, frequency-modulated continuous-wave (FM-CW) radar (Gossard *et al.*, 1970), and lidar (Crum *et al.*, 1987). The record of 5 May (fig. 2.6a) reveals a structure similar to the intermittent turbulent record of Crease *et al.* (1977); there is only slight evidence here of anything visually similar to breaking waves or occasional pulses, corresponding to increased backscattered energy. Note how at about 0640 CST the boundary layer began to grow slowly, with irregular pulses most likely corresponding to surface based thermals.

The occasional linear slanted segments are echoes off the tethersonde. The heating of the boundary layer and subsequent growth of a CBL did not begin in earnest until about 0830. On 6 May (fig. 2.6b), we see a classical example of a SBL with strong surface winds (Crease *et al.*, 1977). These two figures summarize nicely the very different structure of the SBL on the two mornings under examination here.

This study concentrates on a period of weak, highly intermittent turbulence during the period beginning roughly at sunrise but before the boundary layer felt the effects of the strong daytime heating. The aircraft data is used almost exclusively, in particular the horizontal structure of the boundary layer will be emphasized here. Some use will be made of the data from the morning of 6 May, but only data collected high in the boundary layer will be seen to have correspondence to the bulk of the data from 5 May.

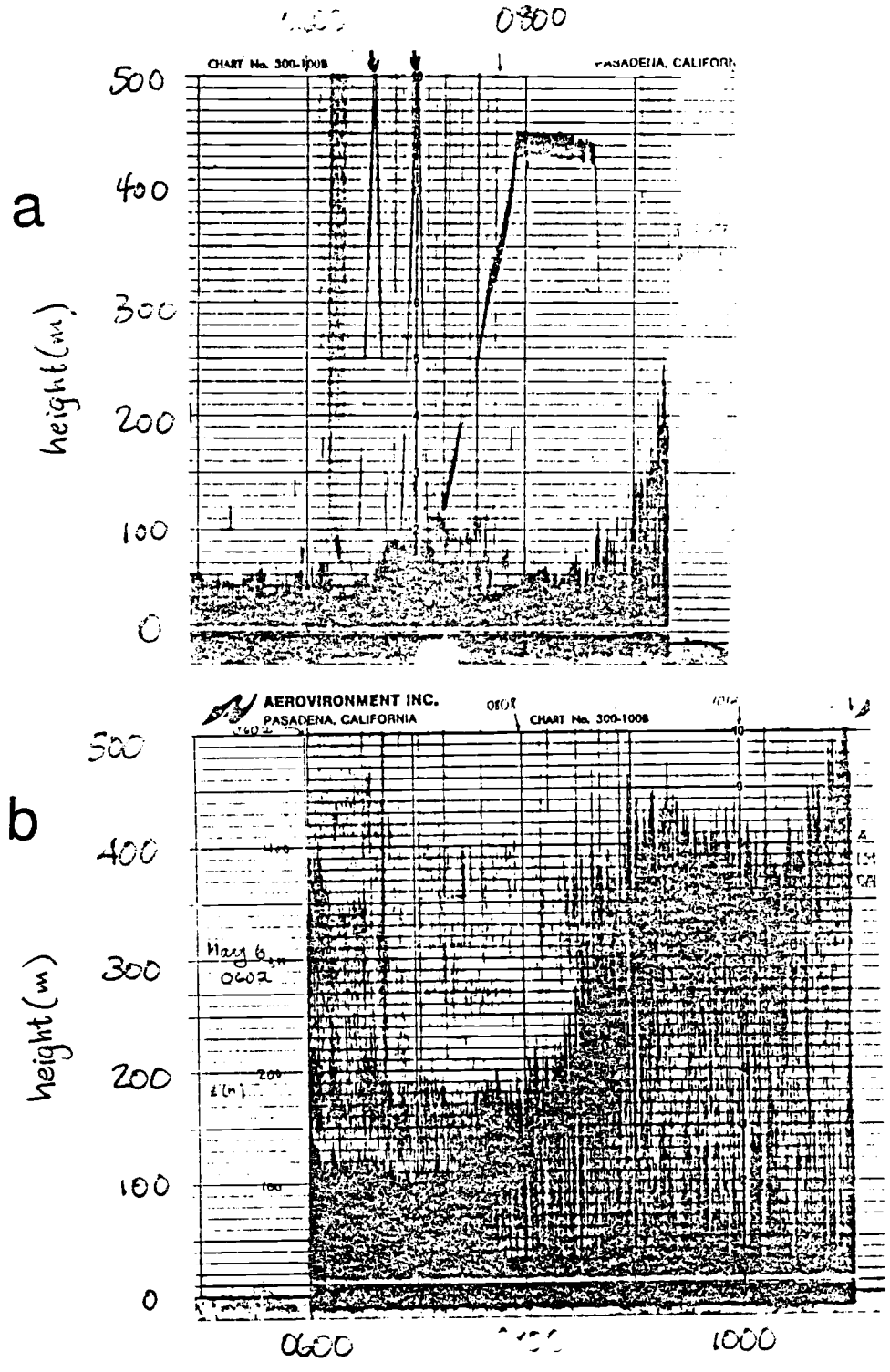

Figure 2.6. Acoustic sounder records from Ft. Sill. (a) morning of 5 May 1979. (b) morning of 6 May 1979.

2. Description of data

Most of the present research will be involved in diagnosing the physical mechanisms which are occurring on the morning of the fifth of May, in particular before convective development begins. During the mornings of 5 and 6 May, the NCAR Queen Air instrumented aircraft was flown in and above the boundary layer. Due to flight restrictions, observations were limited to periods of daylight visibility over the Ft. Sill Military Reservation in south-central Oklahoma; flights lasted approximately 2.5 hr. During these flights, atmospheric turbulence data were collected in two primary modes of operation over gently rolling terrain: 1) slant soundings which penetrated the nocturnal inversion, during which time the aircraft descended or ascended at a slope of about 1.5%; and 2) horizontal legs, during which time the aircraft was flown such that the distance between aircraft and the rolling hills was approximately constant. The average air speed of the plane was 70 m/s and the legs were from 10 to 20 km in length, flown in a north-south direction.

Among the parameters sampled from the aircraft were air temperature, absolute humidity, surface radiation temperature, air pressure, and wind velocity in terms of the scalar components u (west-east), v (south-north), and w (positive upwards). Each of these parameters were sampled at a rate of 20 Hz, then filtered with a low-pass tangent-Butterworth filter (Kaylor, 1977) with a frequency cutoff of 10 Hz to eliminate the effects of aliasing at very high frequencies. Details of the instrumentation are contained in a paper by Wyngaard *et al.* (1978). Taking into account the sampling interval and the average airspeed of the Queen Air, data points are 3.5 m apart in space. The turbulent fluctuations of these parameters are obtained by using a high-pass tangent-Butterworth filter (e.g., $\lambda_c \sim 1$ km) and the mean quantities by applying a low-pass filter (same cutoff). Because a drift problem existed with the microwave refractometer, which is used to sample absolute humidity at 20 Hz, the structure of the mean humidity field was obtained from a dew-point

hygrometer, which did not have the drift problem; it did have poor response characteristics at high frequencies, however. In addition to this data, at Ft. Sill a tethersonde was operated which obtained several soundings of the temperature and wind fields. An acoustic sounder record is also available.

Another set of data available for this experiment is data from an array of 27 Portable Automated Mesonet (PAM) stations, operated by NCAR (Brock and Govind, 1977). These stations collected air temperature and wet-bulb temperature, horizontal wind speed (in terms of u and v components), air pressure, and precipitation. The data was sampled at 1 Hz and saved for later use as one-minute averages (or totals for the precipitation). There was also an array of rawinsonde stations in operation during this period; one of these is located at Ft. Sill. Unfortunately, the morning sounding on 5 May, the day on which much of my research will concentrate, is not available. One additional complication is that the PAM stations were not overflown because they lie outside of the allowable flight area.

The aircraft data for slant soundings during the morning of 5 May, 1979 over Ft. Sill provides useful information about the vertical structure of the SBL. In the Appendix descriptions of the flight legs are given, including times, aircraft heading, and initial and final height above the ground. There are a total of 45 slant soundings interspersed with 12 horizontal segments. The Appendix gives additional information, including the initial and final position (latitude and longitude of the aircraft). Inspection of these appendices verify that the legs are largely north-south runs over the same geographic area. The 7.5´ United States Geologic Survey (USGS) quadrangle (Arbuckle Hill) for this area shows that the flights were taken over a plateau (elevation > 1200 ft) about 7 km across which runs north-south. The area has many hills and ridges and the relief differences along the flight track are up to about 40 m. On a broader scale, there are rolling hills with elevation generally increasing to the northwest; these hills have a horizontal scale of about 2 km.

Figure 2.7 depicts the time-evolution of potential temperature of the morning

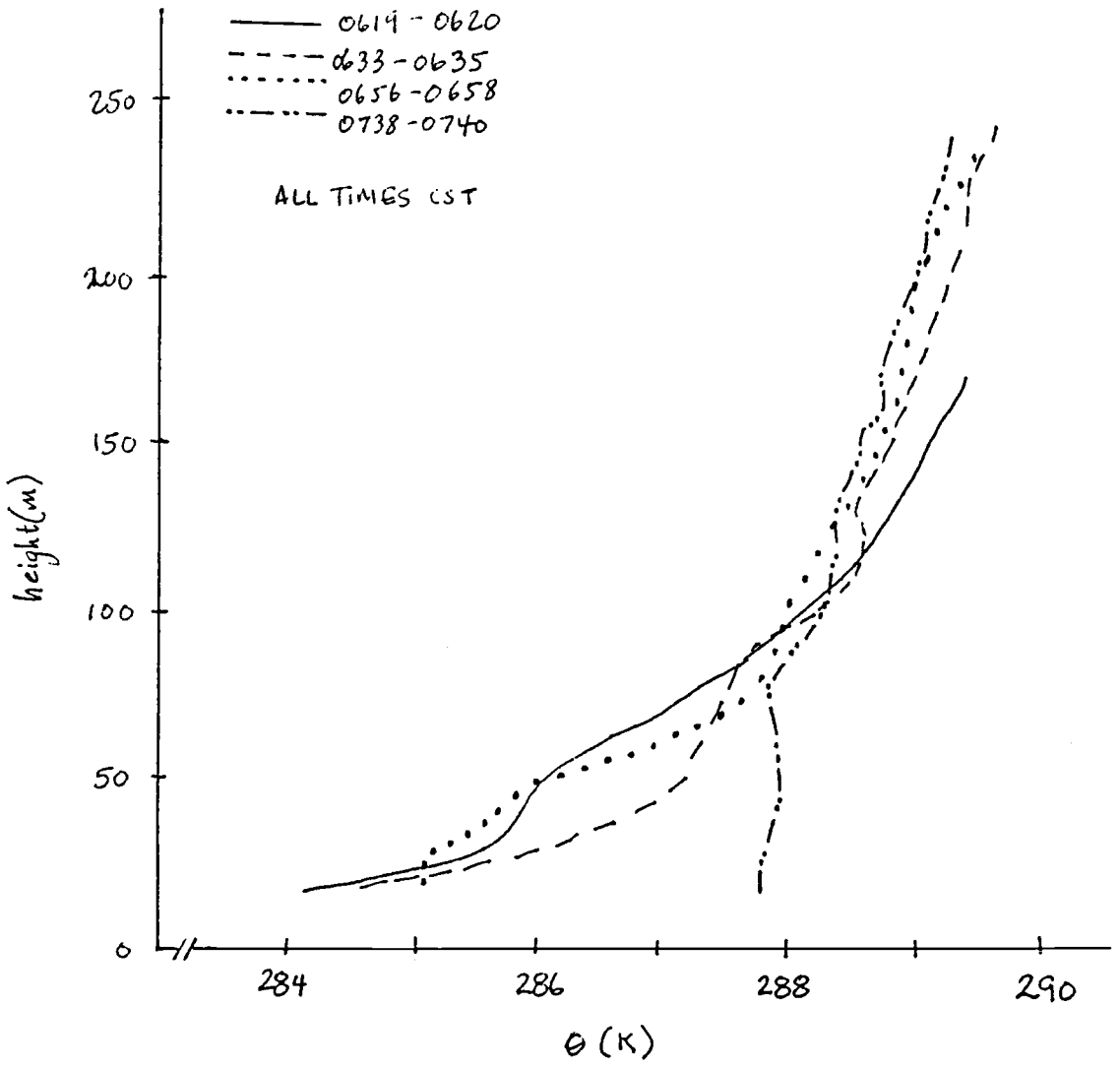

Figure 2.7. Time evolution of vertical profile of potential temperature from aircraft flight soundings, 5 May 1979.

transitional boundary layer, based on selected slant soundings. On some occasions, there appears to be a mixed sublayer within the SBL, as discussed by Mahrt (1985). The mixing is presumably caused by shear-generation of turbulence; not due to strong wind speed gradients but due to the nearly 180° shift in wind direction (from weak northwesterly drainage flow at the surface to weak southerly flow aloft due to synoptic-scale forcing). One can see that the boundary layer is undergoing warming after about 0700. The surface is reasonably moist as there was very heavy rain in the area on 4 May; the land is generally used for agricultural purposes and the clay soils have high water retention. Despite the availability of surface moisture, the boundary layer is relatively dry (in terms of absolute moisture content). For this reason, effects of moisture on the heat flux (i.e. using θ rather than θ_e or θ_v) are neglected.

Table 2.1 contains some selected information from the slant soundings, including the height(s) and magnitudes of maximum vertical velocity variance, kinematic heat flux, and kinematic moisture flux, as well as the height where turbulence vanishes. All 45 legs are not shown because some of the legs did not penetrate the nocturnal inversion and in some others virtually no heat, moisture, or momentum fluxes were found. Some caution should be exercised here before placing too much weight on individual slant soundings, as they are subject to significant sampling problems (Mahrt, 1985).

Moisture fluxes are uniformly small throughout the morning, with some higher values near the end of the flight, especially for legs 35, 36, and 42. The average of the vertical velocity variance is a good indicator of turbulence; analysis of the data in Table 2.1 shows that there is substantial variation from flight segment to flight segment. There are many possible explanations for this result. The aircraft does not always descend/ascend at the same location; if there are preferred locations for turbulence, then we might expect horizontal inhomogeneity is the cause. The transitional boundary layer is also undergoing substantial modification during these soundings, hence nonstationarity may be a factor.

Table 2.1

Flight 3 "flux" maxima – slant soundings

leg	$\overline{w'^2}$ $(\frac{m}{s})^2$	height m, AGL	$\overline{w'\theta'}$ $(\frac{dm\ K}{s})$	ht m	$\overline{w'q'}$ $(\frac{gm\ m}{kgm\ s})$	ht m	ht where $\overline{w'^2} \rightarrow 0$
5	0.030	40	–0.028	40	—		100
7	0.014	49	-0.014	49	—		69
8	0.004	19	-0.010	19	—		79
			0.008	29			
11	0.016	58	-0.015	58	—		98
13	0.018	69	0.023	79	—		149
16	0.005	43	-0.008	23	—		153
	0.006	123	-0.010	123			
19	0.030	60	0.037	60	0.003	60	100
20	0.019	40	-0.030	40	—		60
21	0.016	31	-0.019	31	—		211
	0.009	51	0.021	43			
22	0.018	22	-0.028	32	—		82
23	0.014	27	-0.009	27	0.004	27	137
24	0.008	22	-0.034	32	—		52
26	0.036	23	-0.042	53	0.012	23	103
	0.036	43	0.018	63	0.009	53	
27	0.024	25	-0.013	25,35	0.014	25	55
28	0.027	28,38	—	—			58
29	0.020	37	-0.011	27	—		57
	—		-0.020	47			
33	0.047	73	-0.029	73	0.013	73	103
35	0.061	45	-0.037	35	0.028	15-35	95
36	0.098	59	-0.045	59	0.041	59	139
	0.034	89	-0.035	89	0.008	89	
37	0.056	20	0.061	20	0.009	20	100
	0.081	50	0.008	50	0.015	50	
	--		-0.024	80	—		
38	0.056	29	0.044	29	0.015	29	109
	—		-0.018	49	—		
	0.017	69	0.022	79	—		
39	0.057	28	0.063	28	0.011	28	118
	0.026	68	0.034	78	0.008	78	
40	—		0.014	38	0.005	38	98
	0.021	48	-0.007	48	—		
	0.019	68	0.015	68	-0.007	68	
41	0.040	17	0.064	17	0.015	17	147
	0.070	47	0.020	47	0.013	47	
	—		-0.011	57,77	—		
42	—		0.036	17	—		97
	0.109	37		—	0.026	37	
	0.031	77	-0.009	87	0.016	77	
43	0.086	19	0.046	19	0.017	19	199
	0.046	39	0.020	39	0.010	39	
	0.083	69	0.039	79	0.011	79	
	0.014	159	0.010	159	—		
	0.020	189	-0.006	189	—		

All fluxes were computed using 10-m vertical averages with the midpoint of the lowest layer at 5 m higher than the lowest point in the sounding.

Finally, in stratified boundary layers, turbulence is usually quite intermittent (e.g. Shaw, 1983 and many others).

The above statements make it difficult to generalize about the evolving structure of the morning transitional boundary layer of 5 May. The magnitude and intensity of the turbulence has no apparent systematic relationship with elapsed time. After about 0720, however, the peak value of vertical velocity variance does remain at a fairly high value, on the order of 0.1 $m^2 s^{-2}$; this is not surprising since this is when a CBL is beginning to be established. The height where this variance vanishes, taken at this point only as a qualitative measure of the NBL height, does not seem to show any discernible trend.

Until about 0725, the peak values of the kinematic heat flux are almost uniformly negative (downward), after which positive values take over, again as expected for CBL growth. There remain, however, significant negative values (usually at a progressively higher elevation) throughout the flying period. The large positive value for leg 13 (about 0630) is due to a fairly intense thermal evident in the raw time series plot. The transport of heat is changing sign fairly close to the ground while the level at which there is significant downward heat flux appears to be gradually lifting; its magnitude also decreasing with time. Figure 2.8 contains some profiles of the quantities mentioned above. Note that some legs illustrate a double- or triple-peaked structure. The heat flux is largely downward except late in the morning when penetrating thermals are present.

Now that the synoptic-scale forcing, vertical SBL structure, and data collection methods have been described, the analysis of aircraft data can proceed. Chapter III initiates the analysis of the horizontal structure of the SBL of 5 May, using several different analytical techniques.

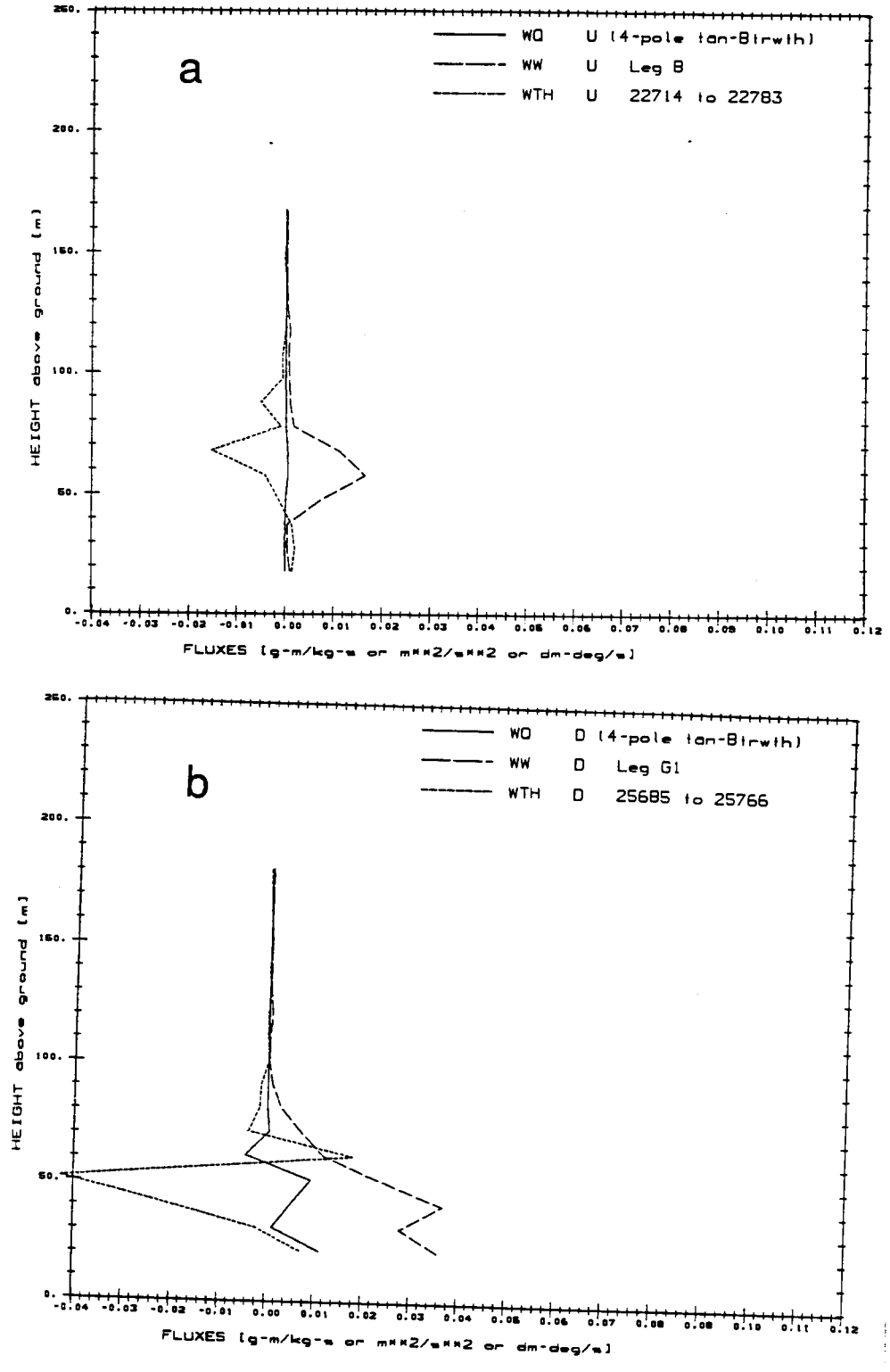

Figure 2.8. Vertical profiles of heat and moisture fluxes and vertical velocity variance for morning aircraft slant soundings, 5 May 1979. (a) before significant surface heating; (b) during mixed-layer development.

Chapter III

Data Analysis Techniques

1. Introduction and Review

This section describes several different procedures utilized for processing the data (from the Queen Air, in particular) from the SESAME NBL experiment. Filtering methods, removal of trends, spectral analysis, principal component analysis, and analysis of the joint frequency distribution are among the techniques discussed.

a. Filtering methods

In the initial stages of the data analysis, it was desirable to obtain information about the relative strengths of the turbulence in the PBL on the morning of the fifth of May. Aircraft data from this morning will henceforth be referred to as flight 3 data. After plotting the time series of height above ground, potential temperature, temperature, absolute humidity, and the three velocity components, it became apparent that the turbulence was highly intermittent until near the end of the flight (some 2.5 hr after sunrise). There appeared to be substantial nonstationarity in the time series (with cooling taking place until about 0700 followed by gradual warming for the rest of the aircraft observations). The quasi-horizontal legs also illustrate spatial inhomogeneity, related to the intermittency of the turbulence already mentioned.

Applying a low-pass filter will provide mean flow information, while a high-pass filter will provide information about the "turbulent" part of the flow. In choosing the cutoff wavelength, we must realize that a filter of this type may not exactly satisfy Reynolds rules of averaging (Charnock, 1957); in particular, this means expressions like $\overline{w'\bar{\theta}}$ will not equal zero, as expected. Charnock's analysis shows that the actual spectrum for our data

must have a fairly wide spectral gap in the vicinity of our chosen cutoff frequency, for cross terms like $\overline{w'\bar{\theta}}$ to vanish, a situation rarely encountered in the PBL very far from the surface.

Each level leg was filtered separately and was analyzed for the presence of a spectral gap. The legs either had ill-defined gaps of uncertain significance on a range of wavelengths from 200 m to 1 km, or no gap at all. In many turbulence investigations, it is necessary to assume the validity of Taylor's hypothesis of frozen turbulence, which allows a transformation from the frequency domain to the wavenumber domain. This is not required in our case, however, because our data is sampled from an aircraft moving at a high rate of speed in the boundary layer. At an average speed of 70 m/s, the instruments move through even the largest of the turbulent eddies in a matter of only a few seconds. This is much smaller than the advective time scale of the turbulent eddies themselves (ℓ/U is about 100 s); therefore we are effectively directly measuring quantities in the spatial domain.

Fluxes and variances are obtained by first high-passing the parameters needed for the flux calculations. The filter is a symmetric 4-pole tangent-Butterworth filter, described by Kaylor (1977). It has a desirable sharp cut-off, as discussed by Kushnir (1984). The three velocity components are obtained directly from the data tapes provided by the Research Aviation Facility staff at NCAR. Specific humidity (q) is calculated from the absolute humidity (dew-point hygrometer) and potential temperature (θ) is obtained from the static pressure and ambient air temperature. Once the high passed quantities have been calculated, the various fluxes are found by multiplying high-pass variables and then applying a low-pass filter to the product. So-called leg fluxes are found by averaging the product of high-pass filtered variables over the entire flight leg. As mentioned earlier, the mean profiles of moisture, velocity, and potential temperature are found by applying a low-pass filter to the data available from the slant soundings.

b. Removal of trends

It is necessary at this point to briefly treat the subject of prewhitening or detrending of the data. As would be expected in a transitional boundary layer, the data is hardly stationary, and we see distinct trends in the data. In many cases, the trends are quite pronounced, with very high correlations with time; the nonstationarity can be reduced by linearly detrending the data before proceeding with any spectral analysis or analysis of the probability density function. This trend is removed (via a least squares algorithm resident in the IMSL program library) routinely for the legs because the correlation coefficients between data and time (space) are so large (Table 3.1). Of note in particular are warmer temperatures on the southern end of the horizontal flight segments. Elimination of a mesoscale feature such as this one is crucial before any analysis of the microscale features can proceed.

Table 3.1

Correlation of Boundary Layer Parameters with Time

flight / leg # obs	parameter	r
3 / 1	u	–0.56
	v	–0.15
3780	w	0.58
	T	0.22
	q	–0.75
3 / 2	u	–0.71
	v	–0.38
3960	w	–0.64
	T	0.54
	q	0.44
3 / 3	u	–0.05
	v	–0.08
4020	w	0.16
	T	–0.01
	q	–0.58
3 / 4	u	0.62
	v	–0.29
2580	w	0.50
	T	–0.36
	q	–0.15
3 / 5	u	–0.40
	v	–0.05
3900	w	–0.16
	T	0.17
	q	–0.60
3 / 6	u	0.38
	v	0.16
3420	w	0.51
	T	0.02
	q	0.31
3 / 9	u	–0.60
	v	0.62
3780	w	–0.03
	T	0.80
	q	–0.65
3 / 10	u	–0.57
	v	–0.73
3420	w	–0.10
	T	–0.64
	q	0.30
3 / 11	u	0.79
	v	0.90
4020	w	0.27
	T	0.93
	q	–0.64

2. Spectral Analysis

a. Classical methods

Analysis of time series is facilitated by utilizing spectral analysis (Jenkins and Watts, 1968). The techniques are well–documented and have been applied successfully to many types of atmospheric data. The basic procedure involves computation of the spectrum, defined as

$$S(\omega) = \frac{1}{\pi} \int_{-\infty}^{\infty} e^{it\omega} R(t)\ dt\ , \tag{4}$$

where R(t) is the autocorrelation function, ω is the frequency and t is the time (here, a continuous variable). In practice, our data is discrete and we use the efficient FFT method to obtain an estimate of the spectrum. Then we would rewrite (4) as

$$S(\omega) = \frac{1}{\pi} \sum_{t=0}^{n-1} \varphi(t)\ e^{it\frac{\omega}{n}}\ ,\ \omega = 0, 1, \ldots, n-1\ , \tag{5}$$

with n being the record length and $\varphi(t)$ representing the time series. By studying the shape of the resulting spectrum, we can infer at what frequencies the physical processes are most active. We often look for large peaks in the spectrum as well as spectral gaps (frequencies at which there is relatively little power in the spectrum) which might be suitable for choosing a cutoff frequency for any filtering. To obtain a more stable spectrum, smoothing should be performed or the time series may be broken up into several shorter segments, whose individual spectra are averaged.

Cross-spectral analysis can be utilized to establish relationships between two variables. The cospectrum is the real part of the cross-spectrum and is defined by

$$L(\omega) = \frac{1}{\pi} \int_{-\infty}^{\infty} R_{u,v}(t)\ \cos\ \omega t\ dt\ , \tag{6}$$

where $R_{u,v}(t)$ is the cross-correlation function for variables u and v. The cospectrum is due to the in-phase correlation, which is responsible for fluxes. The quadrature is the complementary part of the cospectrum; it involves power where the two parameters are out-of-phase. It is defined by

$$Q(\omega) = \frac{1}{\pi} \int_{-\infty}^{\infty} R_{u,v}(t) \sin \omega t \, dt \, . \tag{7}$$

The quadrature spectrum is important in studies of wave motions, where there is often a substantial phase lag between variabless.

Two other useful quantities are the coherency spectrum, a measure of the total correlation between the two variables at each frequency, and the phase angle spectrum, which illustrates phase angle between variables. Coherency and phase angle are defined by

$$Co(\omega) = \frac{\left(L(\omega)\right)^2 + \left(Q(\omega)\right)^2}{S_u(\omega) \; S_v(\omega)} \tag{8}$$

and

$$\phi(\omega) = \tan^{-1} \left\{ \frac{Q(\omega)}{L(\omega)} \right\} \quad , \tag{9}$$

respectively.

Spectral analysis of turbulence in the PBL has several uses. We can analyze the spectra for ranges at which the spectra exhibits a power dependency on frequency, e.g. we could look for a range over which the spectra falls off at a slope of $k^{-5/3}$, as predicted for the inertial subrange. We can also analyze the cross-spectra for the presence of waves vis-à-vis stratified turbulence. At least for linear buoyancy waves, we would expect a phase relationship between w and θ to show a phase lag of 90° (Busch *et al.*, 1969). As already alluded to, however, for nonlinear waves in particular, the phase lag may not be as pronounced in the cross-spectral analysis. On the scales of the main transporting turbulent

eddies, w and θ should be highly correlated with the phase angle small.

b. Rotary spectral analysis

Because some of the flow features in the stable boundary layer (SBL) are characterized by systematic rotation of the wind vector with distance, rotary spectral analysis should be applicable. Pioneering papers by Fofonoff (1969), Gonella (1972), and Mooers (1973) all contributed to the theory of rotary spectral analysis and applications to oceanography. Rotary spectral analysis is included in a summary of vector spectral methods by Calman (1978a, 1978b). The analysis of time series by rotary spectral methods is quite similar to space-time spectral analysis, which has seen use extensively in analysis of general circulation model output (Pratt, 1976) and in analysis of data retrieved from satellites (Hayashi, 1980).

One of the recent studies which includes this technique is a study of oceanic internal waves (Levine *et al.*, 1983). The technique has seen only limited application in the atmospheric sciences in studies of coastal winds in the western United States (O'Brien and Pillsbury, 1974 and Caldwell *et al.*, 1986, Halliwell and Allen, 1987). None of the papers cited are involved in studies of microscale motions.

The technique involves spectral analysis of a complex variable, say V, where V could be defined as

$$V = u + iv \ , \tag{10}$$

where u and v are the normal horizontal wind components, and $i \equiv (-1)^{1/2}$. The spectrum is related to the Fourier transform of V, which will be indicated by $\hat{V}$. It is assumed (Gonella, 1972) that the components of $\hat{V}$ may be expressed as

$$\hat{u}(l) = a_1(l) \cos(2\pi k l) + b_1(l) \sin(2\pi k l) \tag{11a}$$

and

$$\hat{V}(l) = a_2(l) \cos(2\pi k l) + b_2(l) \sin(2\pi k l) \quad , \tag{11b}$$

where l indicates spatial position and k is the wavenumber.

$\hat{V}(l)$ is therefore a complex oscillating two dimensional velocity vector which, as Mooers (1973) shows, can be decomposed for each wavenumber (or frequency) into anticlockwise and clockwise motions (positive and negative wavenumbers, respectively) in an elliptical hodograph plane. This effectively amounts to a coordinate translation; the interpretation of invariant quantities such as total spectra, quadrature, and coherence is fairly straightforward. The partitioned transformed velocity may be written as

$$\hat{V}_A = \frac{1}{2} [(a_1 + b_2) + i(a_2 - b_1)] \tag{12a}$$

and

$$\hat{V}_C = \frac{1}{2} [(a_1 - b_2) + i(a_2 + b_1)] \tag{12b}$$

where dependence on position is implicit, and subscripts A and C refer to anticlockwise and clockwise motions, respectively.

The parameters of interest are the counter-rotating components of the rotary spectrum,

$$S_A = \frac{1}{2} \hat{V}_A \hat{V}_A^* \tag{13}$$

and

$$S_C = \frac{1}{2} \hat{V}_C \hat{V}_C^* \, , \tag{14}$$

the total rotary spectrum $S_T = S_A + S_C$, the quadrature spectrum

$$Q_V = 2(S_C - S_A) \, , \tag{15}$$

the ellipse stability, whose magnitude is interpreted by Mooers to be coherence between the

counter-rotating components

$$E = \frac{\hat{V}_A \hat{V}_C}{\sqrt{4S_A S_C}} , \tag{16}$$

and the rotary coefficient

$$C_R = \frac{S_C - S_A}{S_T} . \tag{17}$$

The asterisk in (13) and (14) denotes a complex conjugate. These quantities have proven quite useful in interpretation of rotary spectra in studies of internal and inertial waves in the ocean and sea breezes in the atmosphere. In essence, the rotary spectral analysis is simply an alternative method of presentation of cross-spectra. Relationships can also be derived from the rotary spectrum for phase and magnitude of the cross-spectrum.

It is interesting to note in particular that there is a strong relationship between the quadrature spectrum and rotary spectrum (Eq. 15). Whether one approaches a problem using cross-spectral analysis and interprets the quadrature spectrum or chooses rotary spectral analysis, the results of such an analysis will be similar. However, the latter method's results seem to have a more straightforward physical interpretation. Quadrature between two variables indicates that there is a systematic phase difference between them at certain wavenumbers; one variable leading the other. If there is significantly more power at (for example) the negative wavenumber estimate of the rotary spectrum compared to the positive wavenumber estimate, there is said to be a preference for clockwise rotation. This is useful in verifying inferences on the nature of waves and shear-induced eddies which might be present. Furthermore, Lumley and Panofsky (1964) discuss the importance of the quadrature spectrum in determining relative position of an observer to turbulent eddies. This discussion will be alluded to when the results are presented later.

In this study, as in Gonella's, all calculations of the spectrum were carried out by first subdividing the record into four sub-records of equal length. After removing the mean

value and linear trend from each sub-record, a fast Fourier transform is utilized to obtain the spectrum for each sub-record, the results of which are then averaged over the four sub-records at each resolvable wavenumber. This amounts to loss of resolution in wavenumber space but the spectral estimates are more reliable (Jenkins and Watts, 1968).

Finally, Mooers suggests that rotary spectral analysis should be useful for parameters other than velocity components and that it could be applied to any scalar. While he mentions temperature-salinity relationships, one parameter pairing that comes to mind for the atmosphere is w and θ (potential temperature), since we would expect to find large quadrature (rotational preference) dominating the cross-spectrum for linear gravity waves but not for classical turbulence. The three velocity components will also be investigated, as we would expect to find rotation in vertical planes for shear-driven turbulence, but not for two-dimensional turbulence. Examples will be given as the data is analyzed in the next section.

c. Analysis of aircraft data

The data presented in this section was collected on the morning of 5 May from about 0530-0800 CST (1130-1400 GMT). This was flight number 3 for the Queen Air during the NBL portion of SESAME. Sunrise at Ft. Sill was at 0536 (henceforth all times mentioned will be CST). As mentioned previously, wind speeds were small and the level of turbulence was generally quite low. Inspection of plots of the data reveal patches of turbulence as well as wave-like motions; as an example the wind components and temperature for one leg of the flight (referred to as leg 4) is shown in Figure 3.1. This was a northbound leg flown at a relatively constant 55 m above ground level, at about 0554.

The vertical structure of the boundary layer near the time of leg 4 is depicted in Figure 3.2. This is the sounding immediately preceeding leg 4; simultaneous vertical profiles are not available. It shows that the boundary layer is very strongly stably-stratified, with a mixed sub-layer present about 60 m. Quantitatively, the strength of the

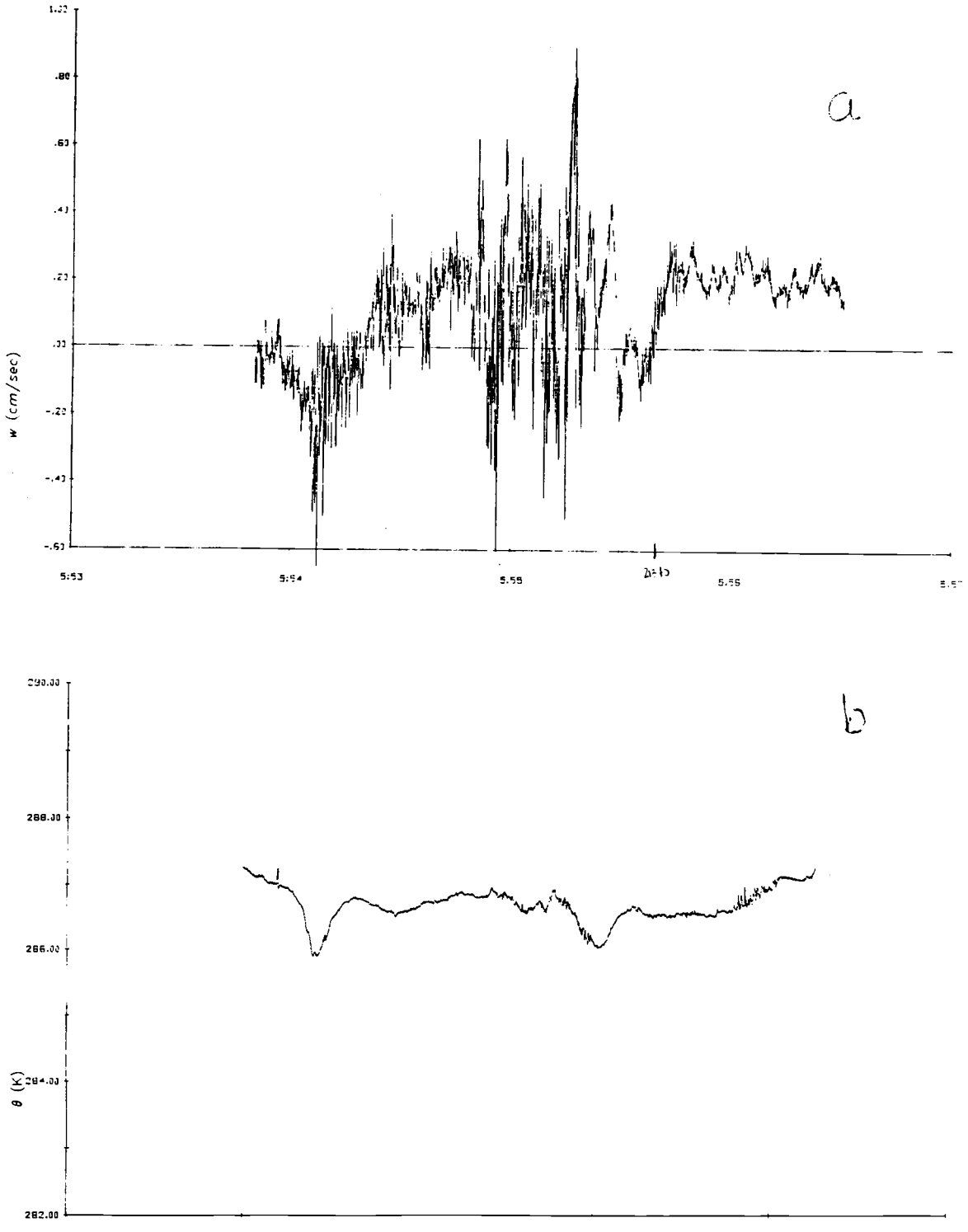

Figure 3.1. Time series of (a) w and (b) T for flight 3, leg 4 from the NCAR Queen Air.

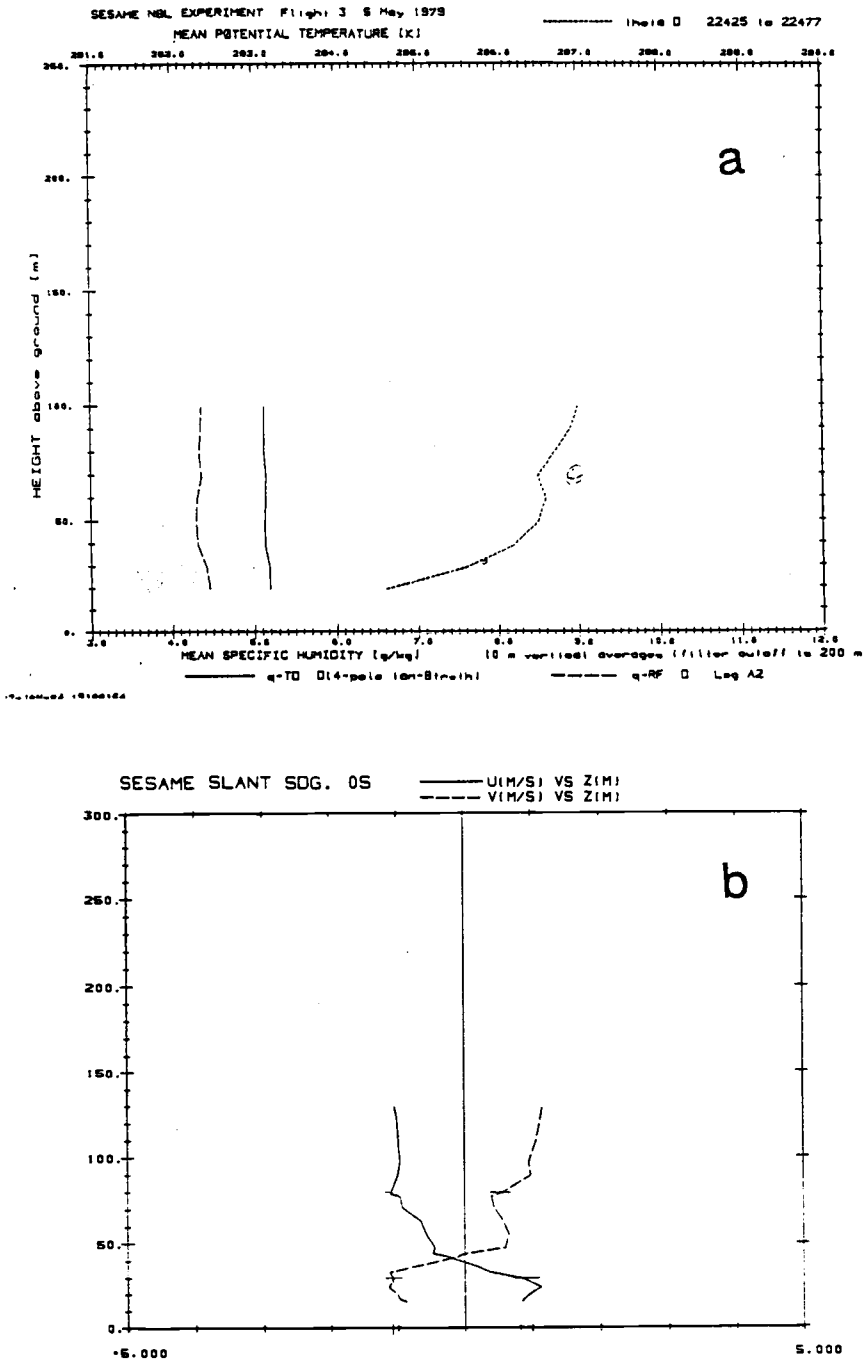

Figure 3.2. Vertical structure of potential temperature, specific humidity, and horizontal wind components from aircraft slant sounding closest to leg 4 a) potential temperature and specific humidity; b) horizontal velocity components (u and v).

stratification is determined by examining the Brunt-Väisälä frequency

$$N \equiv \sqrt{\frac{g}{\theta_0}\frac{d\theta}{dz}}\ , \tag{18}$$

where g is the acceleration due to gravity and θ_0 is the mean boundary layer potential temperature (the vertical potential gradient is assumed positive here as N is real only if the atmospheric layer is stably-stratified). Another important parameter is the wind shear,

$$\Xi \equiv \sqrt{\left(\frac{\Delta\bar{u}}{\Delta z}\right)^2 + \left(\frac{\Delta\bar{v}}{\Delta z}\right)^2}\ . \tag{19}$$

Estimating the local potential temperature gradient at 50 m to be 0.04 K m^{-1} (fig. 3.2a) gives a value of N of 0.037 s^{-1}. The wind profile indicates substantial shear locally, as well, with its magnitude at 50 m estimated to be 0.05 s^{-1} (fig. 3.2b), with much larger values for some slant soundings. The Richardson number is defined as

$$Ri = \frac{N^2}{\Xi^2}, \tag{20}$$

which, using the values for N and Ξ above gives Ri = 0.74, which is greater than the 0.25 critical value (Ri_c) above which flows are generally considered to be stable. Composite soundings are less subject to sampling problems and yield a Richardson number minimum as low as about 0.25 for the most turbulent profiles (Mahrt, 1985).

The unsmoothed power spectrum for u, v, w, and T from leg 4 is given in Figure 3.3. There is a peak in the spectrum at about 375 m for all the parameters, with the peak for v somewhat smaller than that for the other variables; the peak at w is broad and seems to be at a larger scale. Note also the lack of a spectral gap and the apparent lack of an inertial subrange. The fluctuations at the high wavenumber end of the temperature spectrum are most likely due to instrumental noise (Mahrt, 1985). The cospectrum and quadrature spectrum for four pairings of the variables of interest are given in Figure 3.4.

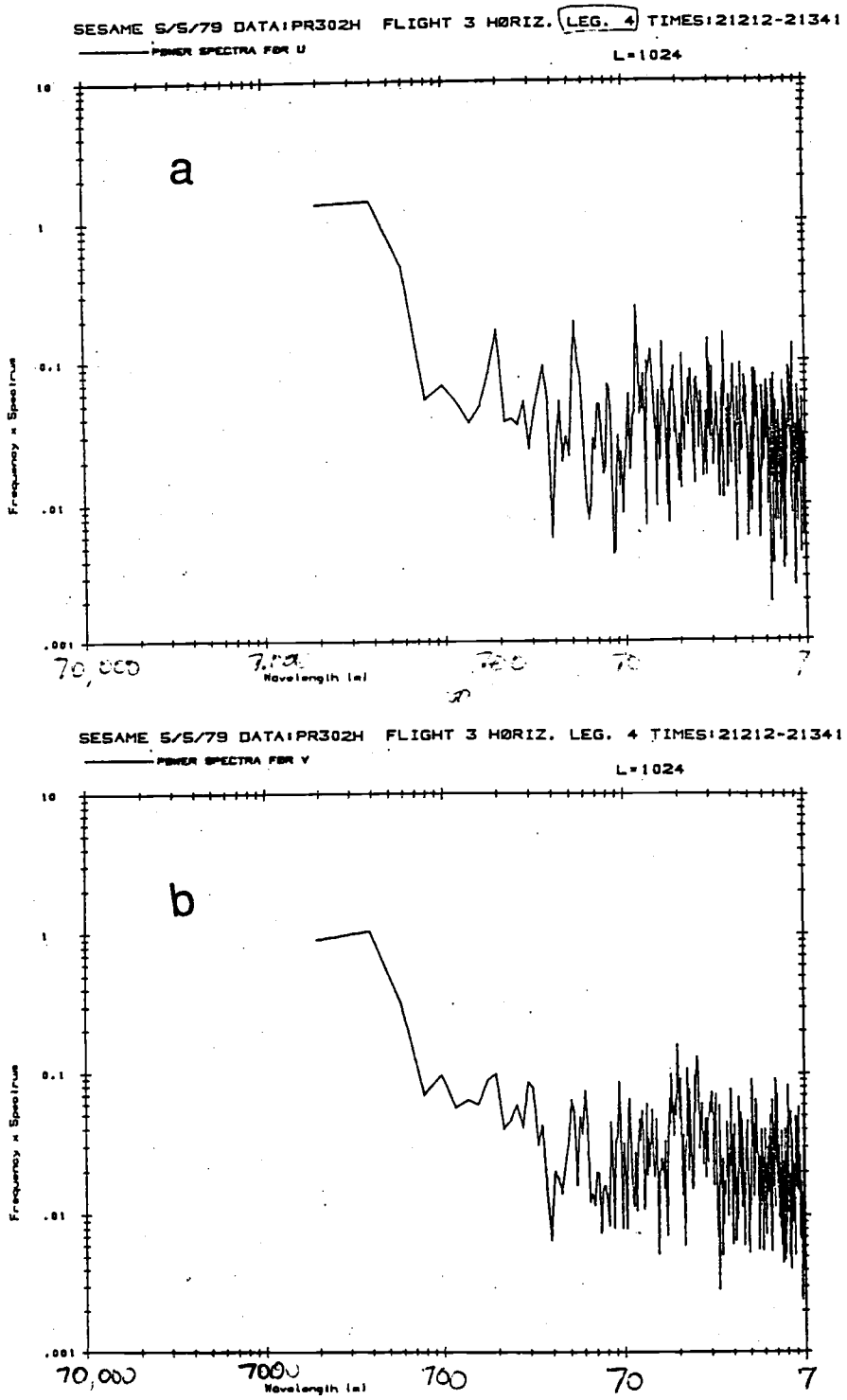

Figure 3.3. Power spectra for u, v, w, and T for leg 4, flight 3 (5 May 1979).

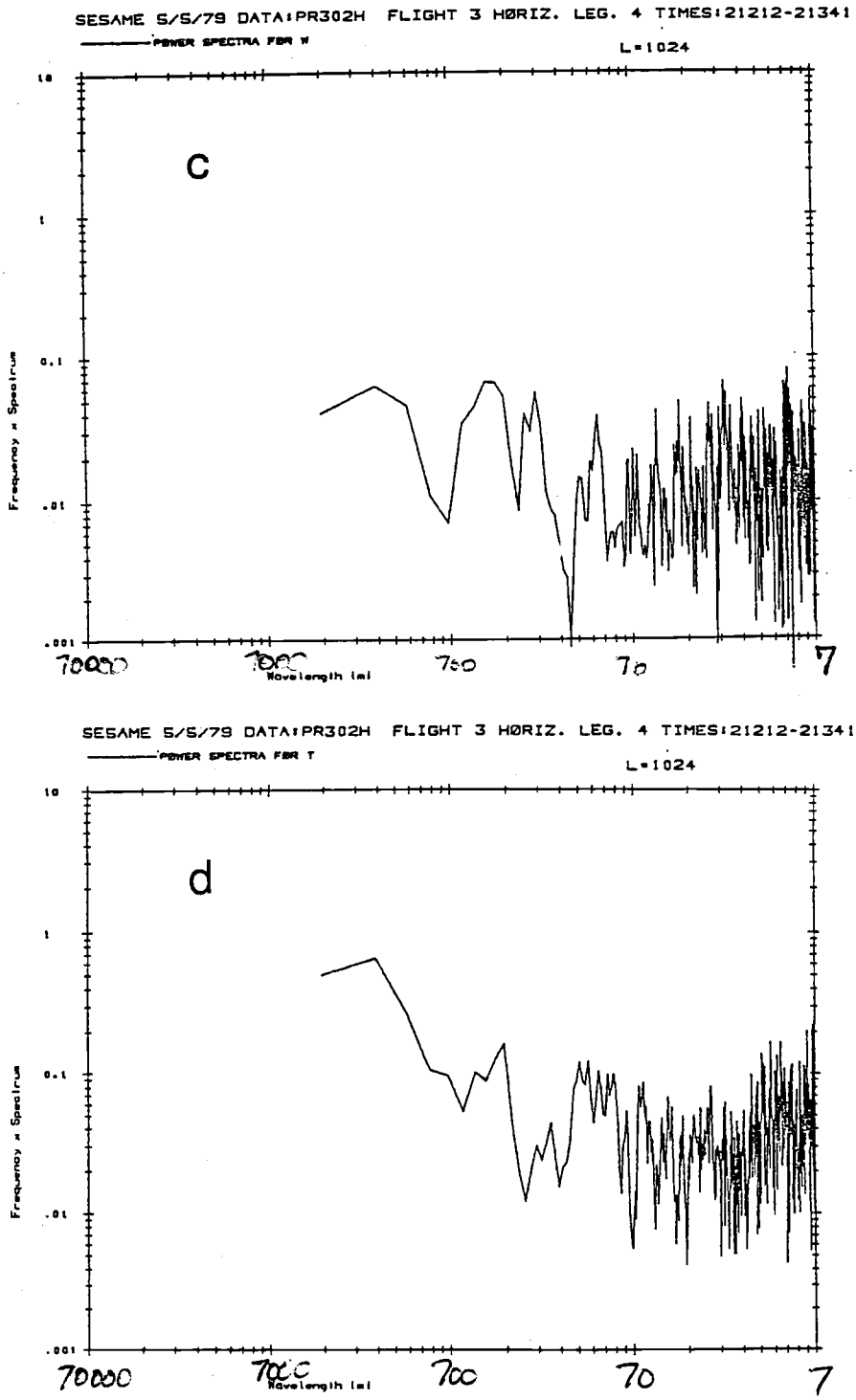

Figure 3.3/continued

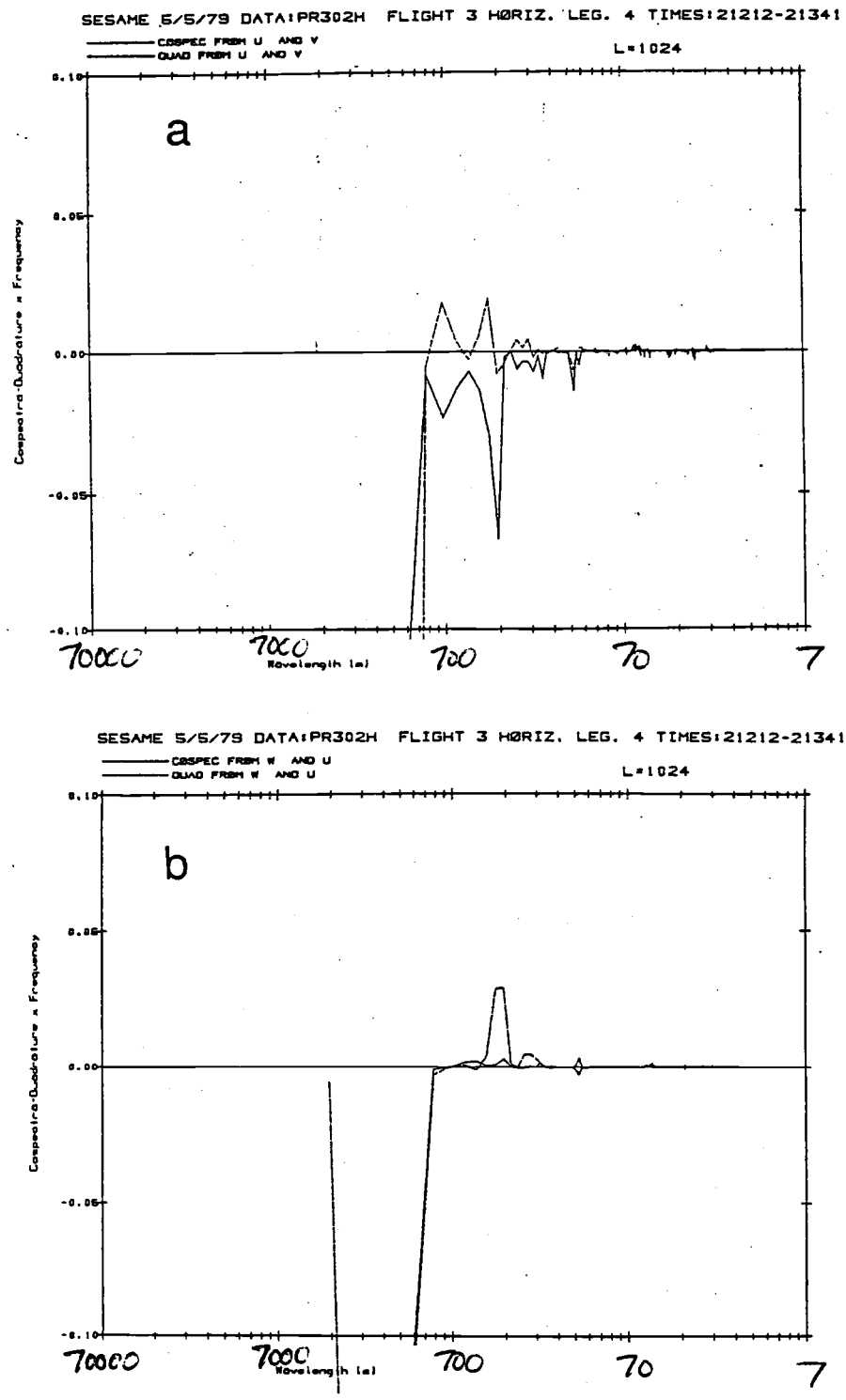

Figure 3.4. Cross-spectral analysis for selected data pairings for the data of Figure 3.1. Cospectrum is indicated by the solid line, quadrature by the dashed line. a) u and v; b) u and w; c) v and w; d) w and T.

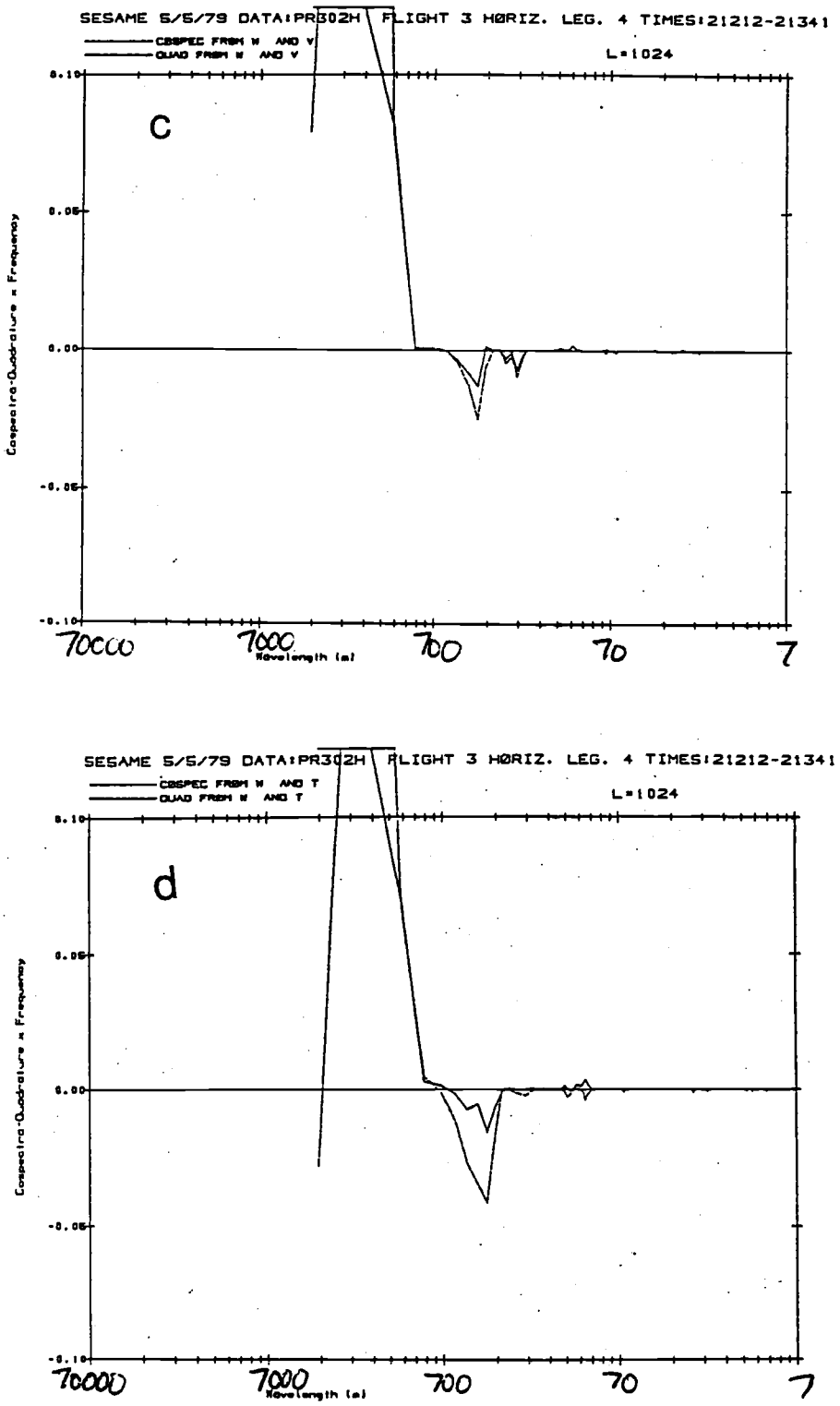

Figure 3.4/continued

Because this is a horizontal flight, it is assumed that T may be substituted for θ because there is no substantial pressure variation over the short flight paths.

Lumley and Panofsky (1964) show how one can analyze the quadrature spectrum between u and w to determine the position of observing instruments in an eddy (i.e. top, bottom, or center). Complicating the analysis, however, may be the presence of waves in the atmosphere. Busch *et al.* (1969), Stewart (1969), Fleer (1983), de Baas and Driedonks (1985), and Dewan (1985) have all given criteria for distinguishing waves from turbulence in stratified flows, based in large part on the result of cross-spectral analysis. Because velocity components are at least partially random in turbulent flows, there should be a fluctuating cospectrum and quadrature spectrum, with neither one dominating. Phase angles should range randomly between –180° and +180°. For (linear) gravity waves, phase angles for w and T will be about 90°, and the cross-spectrum will be dominated by quadrature. In addition, Caughey (1982) shows that the phase angle expected between u and w will be about 90° as part of a set of phase angles between u, w, and T. The phase angles corresponding to the cross-spectral plots in Figure 3.4 are shown in Figure 3.5.

Inspection of Figure 3.4 reveals a strong dominance of the quadrature spectrum over the cospectrum at about 375 m for each of the three cross-spectral peaks involving w. Because the quadrature spectrum is dominating the cross-spectrum (by factors ranging from two to five), it indicates that the two time series analyzed should be out of phase by 90° or 270°. In particular, the phase angles at 375 m (Figure 3.5) show tendencies for fairly constant phase angles of 90° and 270°, particularly for u-w and w-T. For the u-v cross-spectra, the phase angle is about 180°, indicating that u and v are 180° out-of-phase. As we would expect, the cospectrum (Figure 3.4a) exceeds the quadrature spectrum at the peak.

The rotary spectrum calculations for the data in Figure 3.1 are shown in Figure 3.6. In each of the figures, the data pairings are indicated. The total rotary spectrum (S_T) is given as the solid line, with the clockwise-rotating part of the spectrum (S_C) given by the

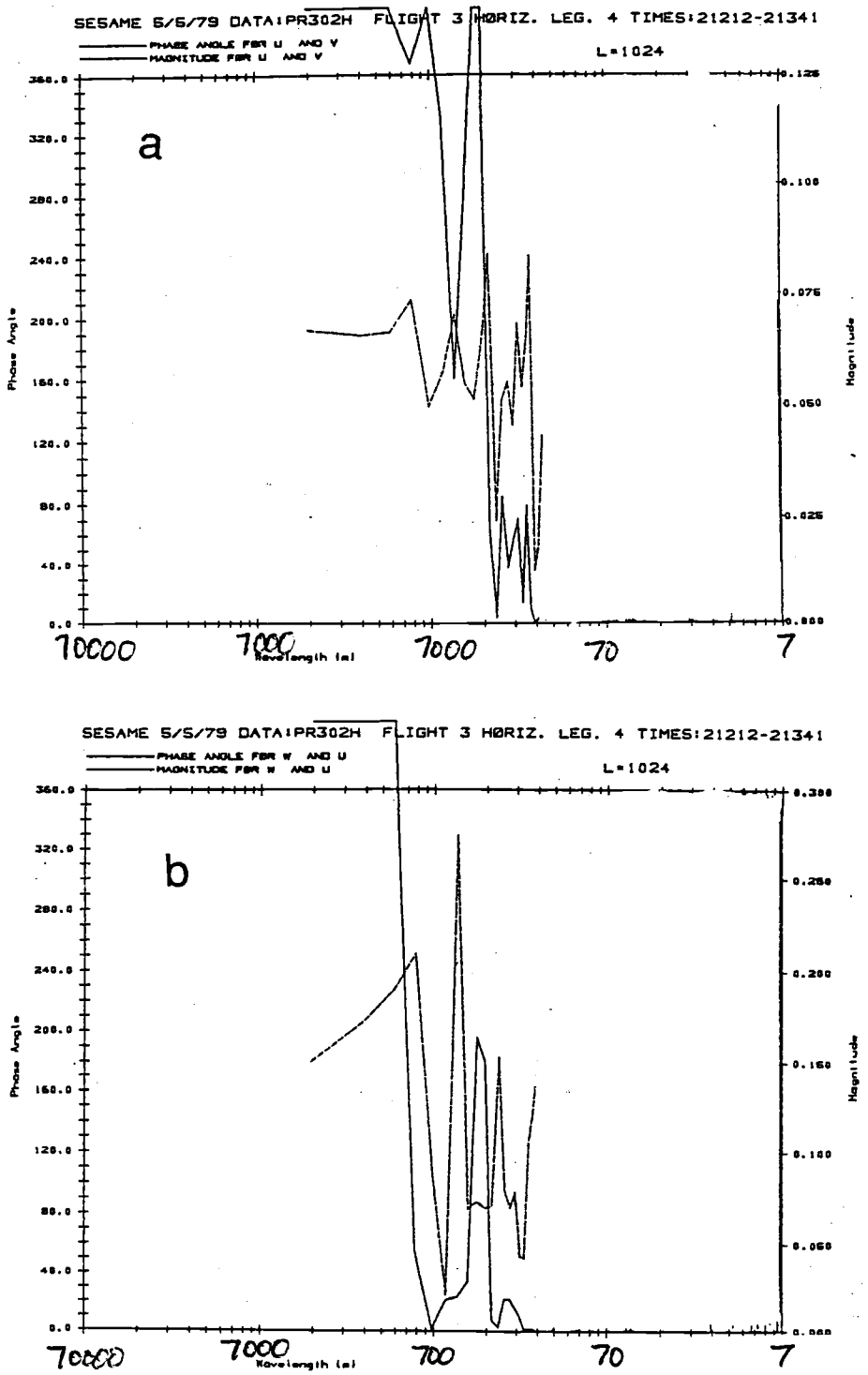

Figure 3.5. Phase angles for cross-spectra shown in Figure 3.4. Because phase angles fluctuate randomly in the turbulence at the smaller scales, only phase angles for wavelengths greater than 175 m are shown.

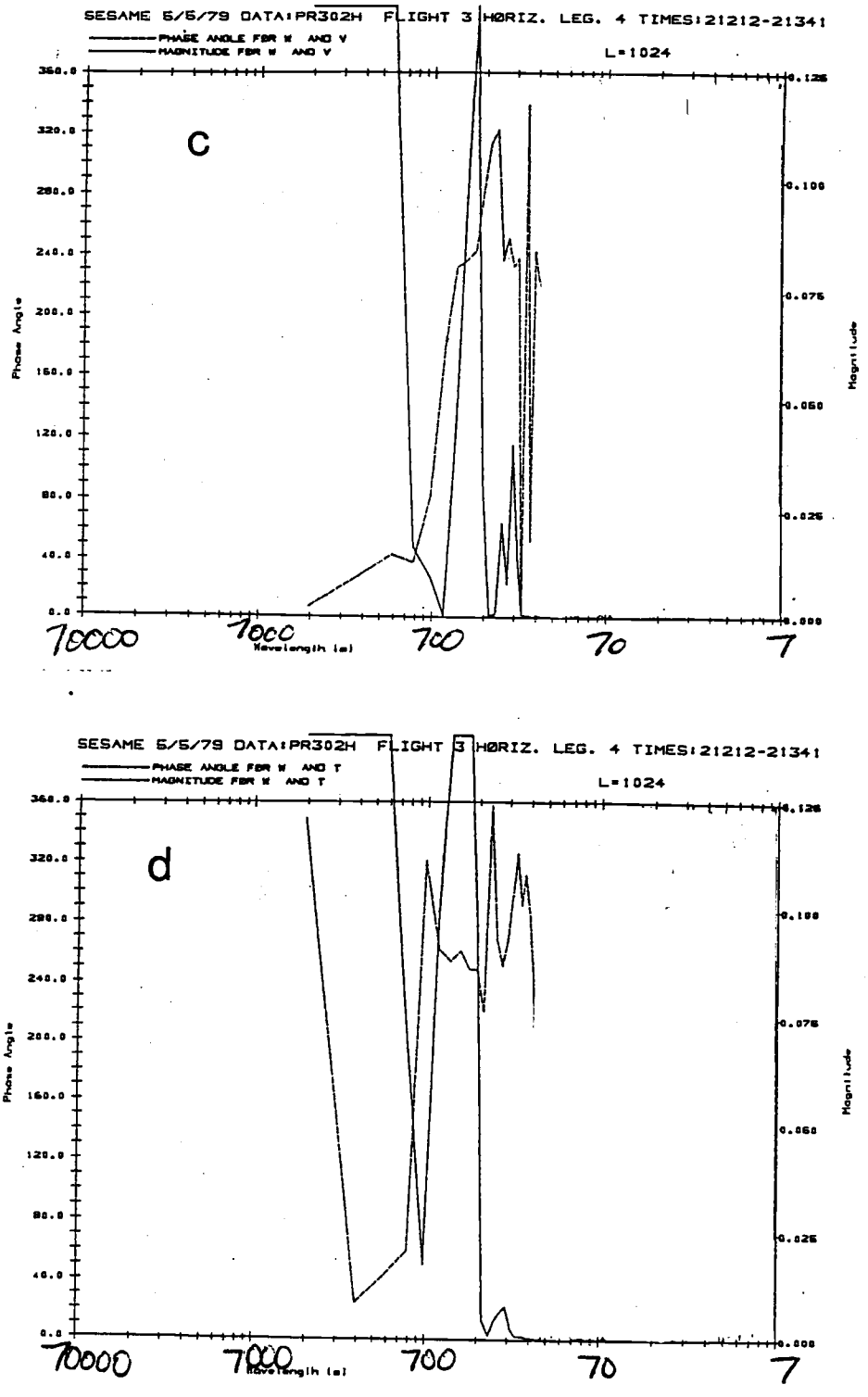

Figure 3.5/continued

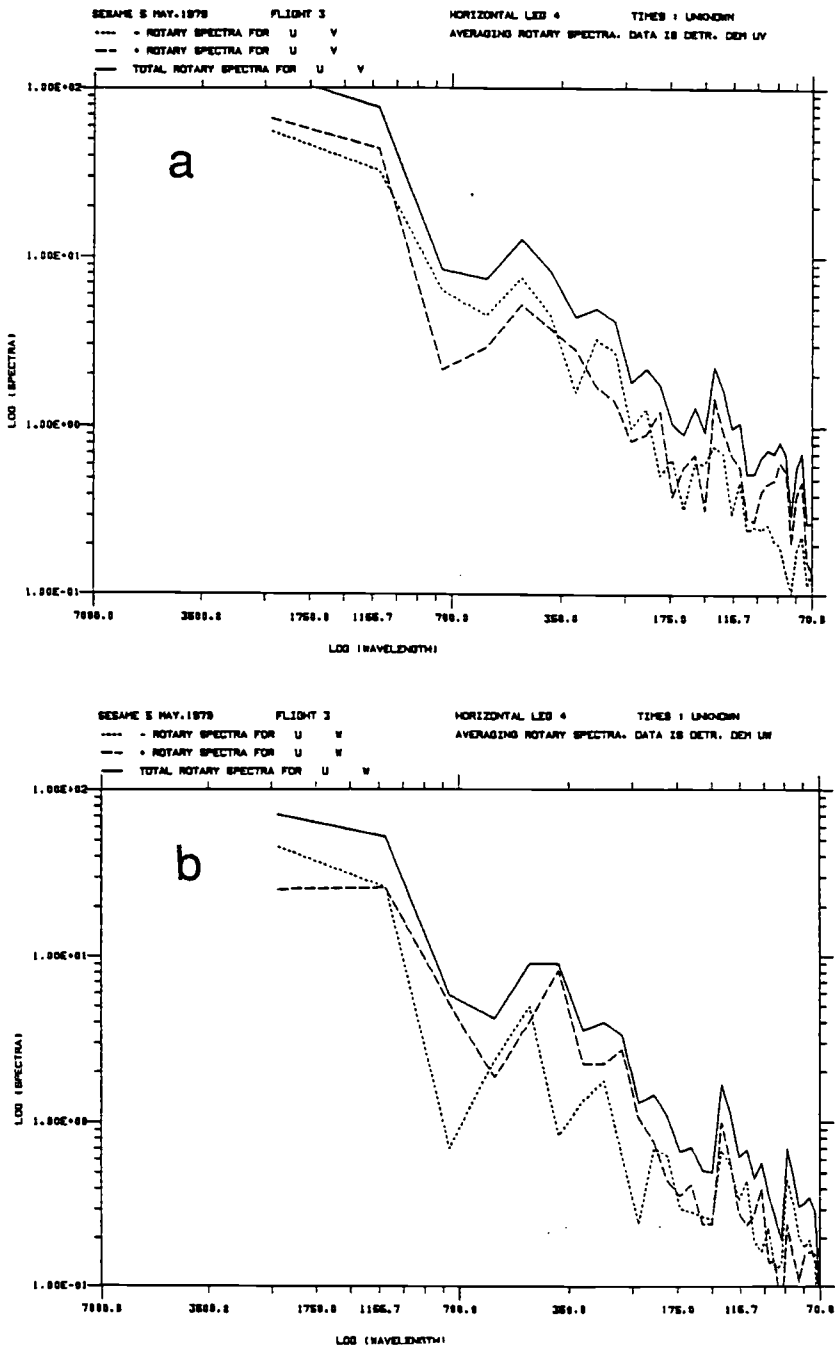

Figure 3.6. Rotary spectra for selected data pairings of leg 4. The total rotary spectra is given as the solid line. The spectrum is partitioned into the clockwise-rotating component (dotted line) and counterclockwise-rotating component (dashed line). (a) u and v; (b) u and w (including 95% confidence bands); (c) v and w; (d) w and T.

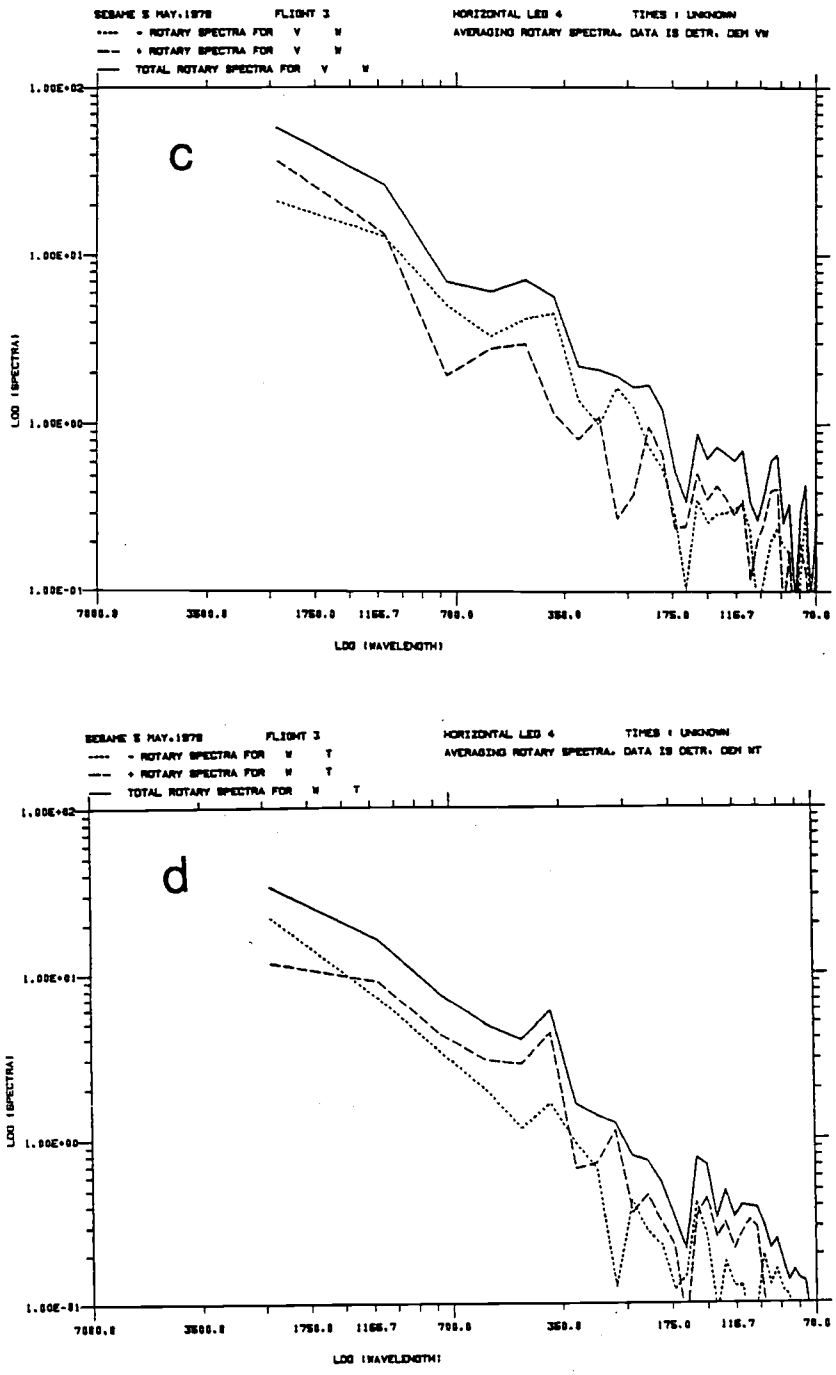

Figure 3.6/continued

dotted line and the counter-clockwise part (S_A) by the dashed line. In the horizontal plane (u-v), there is a significant peak in the total rotary spectrum at about[2] 375 m, but no preferred direction of rotation, as the two counter-rotating components of the rotary spectrum are not significantly different (Figure 3.6a); this indicates no preferred direction for horizontal rotation. The same peak appears in both the u-w and v-w rotary spectra, but in both cases it is characterized by pronounced rotation

In the u-w rotary spectrum (Figure 3.6b), there is a dominance of the counterclockwise rotating component. The opposite is true for the v-w spectrum. These are consistent with the quadrature plots in Figure 3.4 (this can be checked in Eq. 6). These calculations, in combination with the aircraft's heading, indicate that the aircraft is sampling in the top of turbulent eddies which are generated by the directional shear. In Figure 3.7 a schematic diagram illustrates how the shear-driven eddies are forced, as well as the rotation expected in the x-z and y-z planes.

An aircraft passing through a section near the top of the eddies indicated in Figure 3.7 would observe first upward motion, followed by southeasterly motion and finally by downward motion. In the x-z plane, this corresponds to positive w-negative u-negative w. Hence u leads w, which corresponds here to negative Q_{uw} (shown as positive Q_{wu} in Figure 3.4b) or, using (6), $S_A > S_C$, as shown in Figure 3.6b. Similarly, Figure 3.6c illustrates positive quadrature between v and w. In the y-z plane of the eddy, the motion is positive w-positive v-negative w which, in terms of the rotary spectrum, indicates clockwise rotation ($S_C > S_A$); in terms of the phase lag, v is lead by w. The observations taken along the aircraft's flight path appear qualitatively consistent with observations of billows in the atmosphere (Thorpe, 1973).

For vertical motion and temperature, we see there is a preference for counterclockwise rotation, which for w and T corresponds to positive w-negative T-

[2]As explained earlier, some resolution is lost in the averaging procedure. This is the wavelength which results from the averaging procedure. The true wavelength for this case may range from 345 m to 407 m.

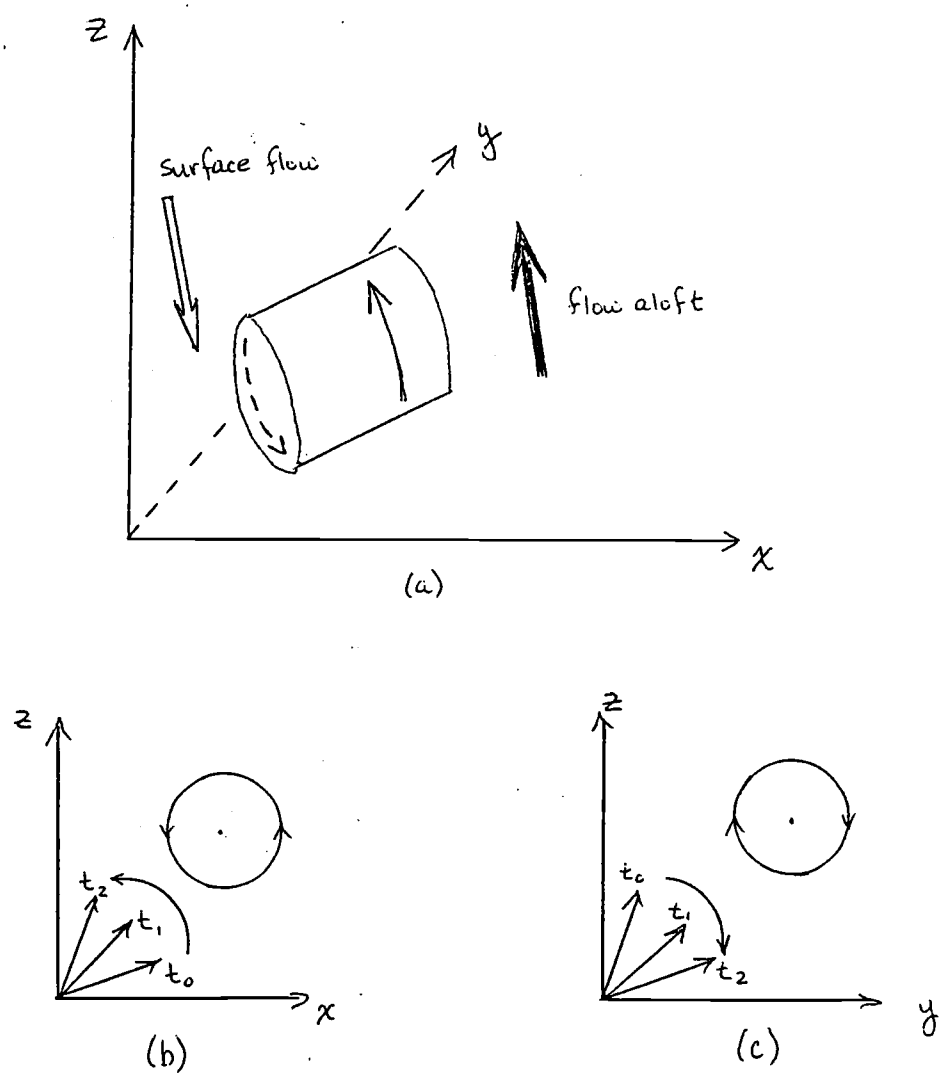

Figure 3.7. Schematic of the shear-driven eddies in the SBL and rotation in the overturning circulation as interpreted by the rotary spectra.

negative w. The corresponding phase angle for the above is 270° (see Figure 3.5d). Referring back to the cross-spectrum for w and T (Figure 3.4d), we note a large quadrature and somewhat smaller cospectrum at about the same wavelength. The presence of a peak in the cospectrum is an indication of transport (the heat flux is downward, as expected for the stable stratification). This is also an indicator of strong interactions between wave fields and turbulence (Hunt *et al.*, 1985). Since the local Richardson number is occasionally subcritical (indicating instability), any internal waves present may be breaking and overturning circulations should be observable. Kelvin-Helmholtz instability (Turner, 1979) is one mechanism which has been used to explain such a wave-turbulence interaction as noted here. For turbulence, however, we might have expected less dominance of the quadrature (and hence less tendency for rotation in the rotary spectra).

One additional note about leg 4 is that there is another spectral peak at about 750 m, twice the wavelength of the aforementioned one. This may simply be a modulation of the other peak or it may be another separate circulation. The power spectra for this leg (fig. 3.3) show only a modest peak at 750 m. Note that the u-w and v-w rotary spectra are similar but the u-v rotary spectrum has more pronounced rotation present. In addition, the asymmetry between rotary components is much less for the w-T 750 m peak than for the 375 m peak.

The next northbound leg (leg 6) was flown at approximately the same altitude about ten minutes later. There is a double-peaked rotary spectrum (fig. 3.8) at slightly larger wavelengths than the 375 m peak seen in leg 4. For these peaks (at about 420 and 490 m) and for leg 4 it appears that the aircraft is sampling consecutive eddies rotating in the same sense. The relationship between w and T is similar to that above except that the peaks for some of the rotary spectra are not deemed significant (Table 3.2 presents some statistics for these spectra and will be discussed in detail later).

In many wall-bounded shear flows, the eddies often occur in pairs which rotate about their axes in opposite directions (Mumford, 1982). In other situations, however,

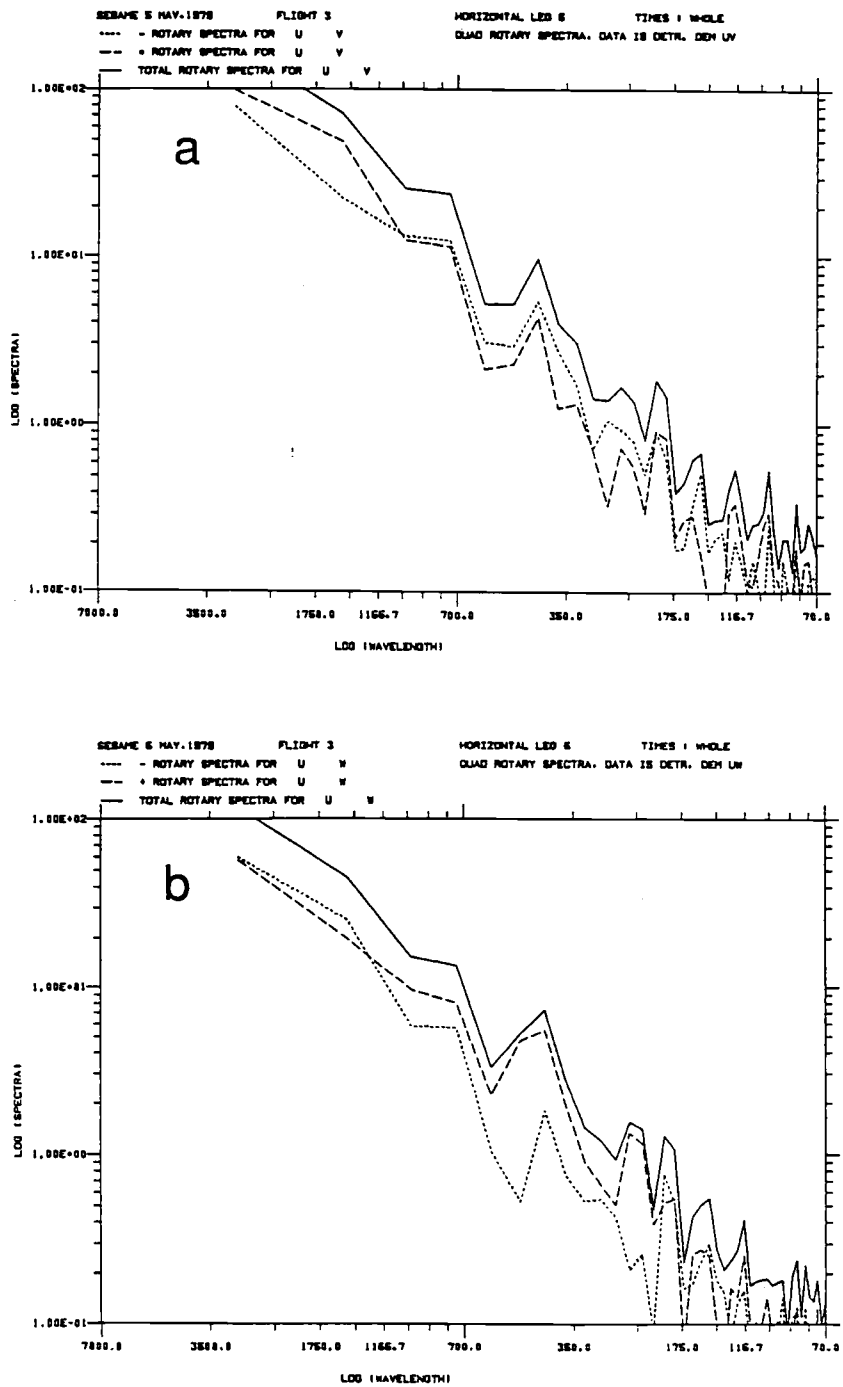

Figure 3.8. As in Figure 3.4 but for leg 6.

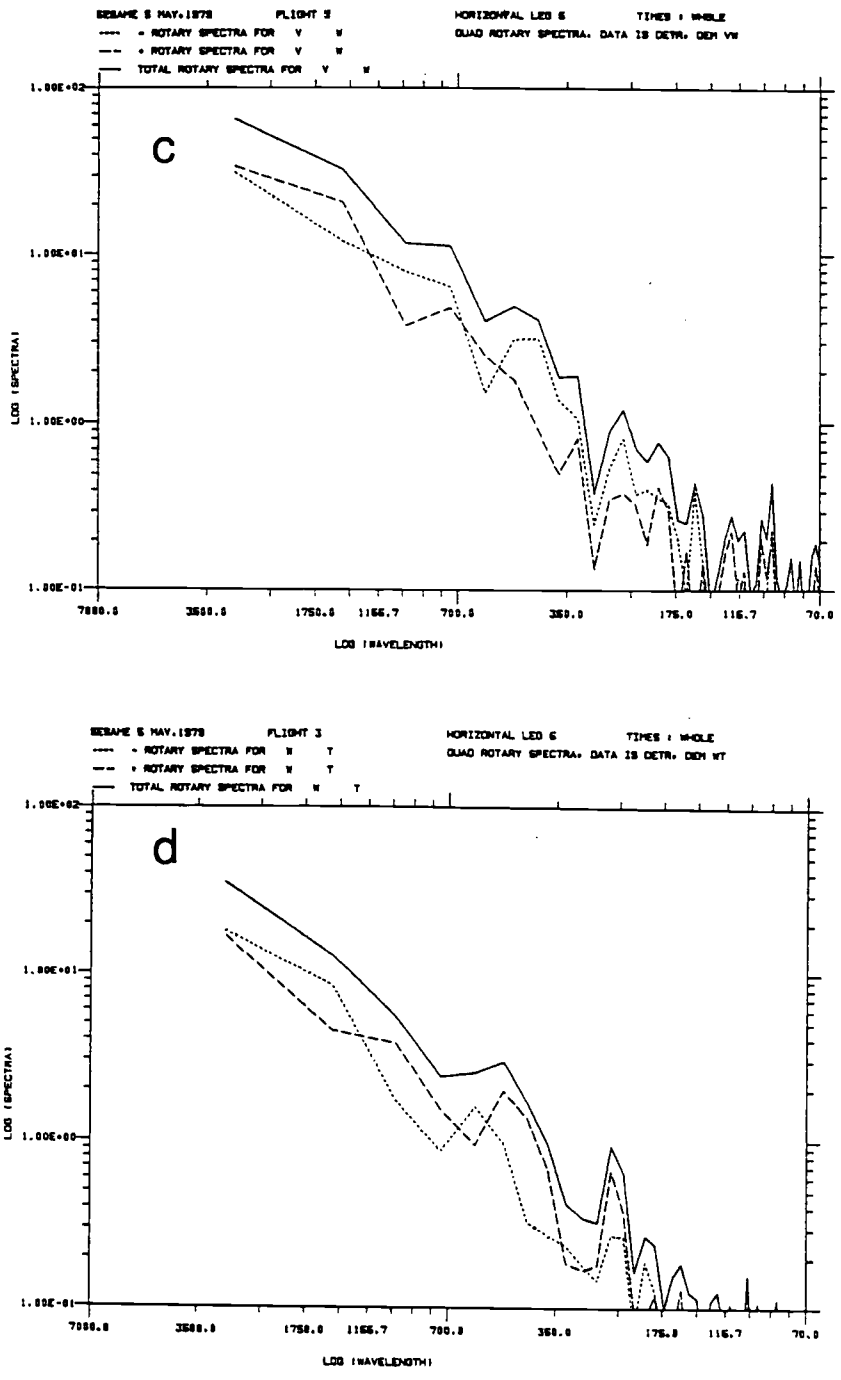

Figure 3.8/continued

such as that forced by the shear in this study, the eddies are all of the same sense with some weak compensation region probably occurring between the eddies. In actuality, these eddies are not directly analogous to eddies in wall-bounded shear flows, whose size is limited by their distance from the wall. The influence of strong stratification works to give much larger horizontal scales than vertical scales. The wavelengths observed here are much larger than their distance from the surface; in fact Mahrt (1985) points out that these types of circulations do not seem to have any connection to the surface.

Two other points should be noted with respect to the eddies. Transverse modes would be favored here over longitudinal modes, which generally are forced by substantial upward heat flux and are characterized by longer wavelengths (Asai, 1970; Eymard, 1985; Shirer, 1986). The aircraft is flying at a small angle to the shear direction and is therefore flying obliquely across the eddies. Hence the eddies are most likely smaller than the peaks indicated in the spectra. Variations in size of the sampled circulations will undoubtedly result from the aircraft not consistently flying at the same relative height in the eddies.

The rotary coefficient, C_R, is a number between –1 and 1 which illustrates the rotational behavior of the spectrum. As we can determine from examination of (8), it will be zero for those wavenumbers with no rotational preference. The closer its value to unity, the more prevalent will be the rotation in the vector (clockwise motions dominating for C_R positive; counterclockwise for negative values). The ellipse stability, E, whose modulus is analogous to a coherence (Gonella, 1972), should be significant for those wavenumbers which exhibit rotational preference of one sign or the other due to linear wave motion.

By way of summarizing the material in this section, Table 3.2 lists values for C_R and $|E|$ for the flight legs analyzed here. In general, the rotary coefficient values are quite small for u-v. This indicates no preferential direction of rotation in a horizontal plane for the entire leg. The signs of C_R for u-w and w-T are always the same for the legs analyzed, with generally large values for u-w. The values for w-T at times indicate significant phase lag (leg 6, flight 3); at other times this is not the case.

Coherent wave motions might be expected to yield large values for the magnitude of E. In previous studies (Caughey, 1982), coherences exceeding 0.9 are not uncommon. This is generally not the case here, which lends support for the earlier statement that wave motions do not appear to be dominating this particular flow, although they are likely to be an important aspect of it. The results of the spectral analysis are summarized in the next section.

Table 3.2

Statistics for Selected Rotary Spectra

Flight/Leg	Variables	Wavelength (m)	C_R	|E|
3/4	u-v	373	0.07	0.79
	u-w	373	-0.81	0.50
	v-w	373	0.62	0.27
	w-T	373	-0.47	0.55
3/4	u-v	747	0.45	0.32
	u-w	747	-0.81	0.66
	v-w	747	0.49	0.22
	w-T	747	-0.17	0.59
3/6	u-v	420	0.09	0.87
	u-w	420	-0.52	0.85
	v-w	420	0.56	0.57
	w-T*	420	-0.62	0.27
3/6	u-v*	490	0.11	0.49
	u-w	490	-0.84	0.14
	v-w	490	0.32	0.00
	w-T*	490	-0.38	0.53

*These combinations are given for completeness; the rotary spectral estimates here were not significant at the 95% level. None of the w-q spectra are significant.

d. Discussion

It has been shown that the rotary spectral analysis technique developed and first used in geophysical flows fifteen years ago is applicable to motions in a stably-stratified boundary layer. Despite rather limited information content of aircraft samples in such a boundary layer (one dimension only for horizontal legs), some useful physical insight is gained by applying rotary spectral analysis to the velocity components as well as scalars such as temperature (and potentially specific humidity in other experiments where analysis of the moisture flux is important). As suggested by Mooers (1973), the useful aspects of the technique are therefore shown not to be restricted to velocity components.

Internal waves are a very common occurrence in atmospheric boundary layers which are stably stratified. This statement is validated by the numerous case studies which have been undertaken (some of which have already been cited here). However, the lower atmosphere is usually much more complicated than a situation which allows linear gravity waves as the dominant mode of motion.

Theoretical and experimental work (summarized by Turner, 1979) shows that there are flow instabilities and shear effects which force waves to break down when the Richardson number is less than some critical value, usually taken to be 0.25. Complete descriptions of the strong wave-turbulence interactions which result have not been forthcoming and much more work needs to be done in this area.

The measurements reported here appear to illustrate the characteristics of periodic eddies, similar to shear-induced overturning and billows, which may result in part from an unstable internal wave regime affected by Kelvin-Helmoholtz instability. While much can be said for the use of quadrature as an aid in physical understanding of boundary layer data, in the author's opinion the interpretation of transport and phase interrelationships appears to be more straightforward for the rotary spectra.

As noted recently by many investigators (Chimonas, 1985; Lenschow and

Kristensen, 1985; Mahrt and Gamage, 1987), there are major limitations to the application of any spectral technique in the analysis of turbulence data. By Fourier-analyzing data, sharp gradients which are known to exist in the data contaminate the entire spectrum. Nevertheless, cross-spectral analysis has historically been an integral part of the analysis of the PBL.

It would be of interest to apply the rotary spectrum technique to tower observations such as those taken at the Boulder Atmospheric Observatory (BAO; Kaimal and Gaynor, 1983). These calculations would be of interest because they would provide direct observation of the vertical structure of phenomena such as the shear-induced eddies observed in this study. The BAO observations have proven quite successful in obtaining information on vertical structure of internal gravity waves, for example (Lu *et al.*, 1983; Finnigan *et al.*, 1984; Lu and Li, 1985). As part of an investigation of SBL turbulence under weak stratification or for strong gravity wave events, rotary spectral analysis could used.

3. Principal Component Analysis

a. Introduction

Empirical orthogonal function (EOF) analysis and its related eigen techniques — principal component analysis (PCA), factor analysis, and pattern recognition analysis — begin with eigenvectors of the correlation or covariance matrix of a set of variables. The background methodology was formalized by Loève (1963). Although each of the methods start with a similar procedure, they diverge substantially in application.

For the past thirty years, eigen techniques have been widely used in meteorological studies of large-scale interrelationships, beginning with Lorenz (1956). This type of technique is particularly useful for identifying relationships between different parameters when waves are present, as pointed out in Wallace and Dickinson (1972). Recent reviews of the use of principal component analysis (Richman, 1986; Ehrendorfer, 1987), have focussed on synoptic- and global-scale analyses.

PCA has also been widely used in the analysis of smaller-scale flow features. An early study by Lumley (1967) first used PCA to analyze motions in a turbulent flow. Other early work has involved modelling of turbulence, as discussed in Dutton and Deaven (1969, 1971) and Petersen (1976). Dutton (1970) first used an eigen technique in an application to design problems, and Panofsky and Dutton (1984) described how the technique can be used to predict the probability of occurrence of large wind gusts.

The analysis of turbulent motion by PCA has also been recently applied by Mahrt (1985) and Frank (1986). This particular application involves the "stacking" of variables into an observation vector ϕ, where

$$\phi = \begin{Bmatrix} u \\ v \\ w \\ T \end{Bmatrix} . \qquad (21)$$

Multivariate P-mode PCA[3] is then performed on the linear combination of variables in the stacked vector ϕ, following Mahrt (1985).

b. Methodology

The analysis procedure is as follows: each of the variables in the observation vector (21) has its mean removed. Then the demeaned series is high-pass filtered with a cutoff wavelength of 1 km. This eliminates the linear trend as well as any other mesoscale information. The correlation matrix is calculated, and its orthonormal eigenvectors are obtained using a standard statistical library subroutine. The standard eigenvalue problem entails the ordering of the four eigenvectors, according to the percent of variance each explains. The variables are then normalized by their standard deviation, both to ensure that a parameter with large variability will not dominate the multivariate analysis and also to avoid the problem of uncommon units of measurement. The principal components (PC scores) are formed from the eigenvectors and normalized observational vector as

$$Z_i(y) = \sum_{j=1}^{4} e_{ij}\, \phi_j(y) \quad , \quad i = 1, \ldots , 4, \tag{22}$$

where e_{ij} is the termed the i^{th} eigenvector element for the j^{th} variable. The meteorological variables have at this point undergone a transformation to a new set of four variables (the Z_i), which are linear combinations of the original four variables and which describe progressively smaller portions of the total multivariate variance.

The variance of each principal component is equal to the associated eigenvalue of the original correlation matrix,

$$\sum_{k=1}^{n} {Z_{ik}}^2 = \lambda_i \ , \ i = 1, \ldots , 4 \ , \tag{23}$$

where n is the number of observations. The proportion of variance explained by the i^{th}

[3]Richman, 1986; p. 315 has a description of the six different modes of PCA. P-mode involves the use of n_p parameters and n_o observations in a time or space series.)

eigenvector is sometimes used to assess statistical significance of the i^{th} eigenvector and its associated principal component; it may be found from

$$\frac{\lambda_i}{\sum_{i=1}^{4} \lambda_i} . \qquad (24)$$

The original variables can be recovered from the principal components from

$$\phi_j(y) = \sum_{i=1}^{4} e_{ij} Z_i(y) \quad , \quad j = 1, \ \ldots \ , 4. \qquad (25)$$

The eigenvectors do not represent necessarily any specific physical structure in the data, since the statistical technique is designed to recover maximum variance in the first eigenvector. Nonetheless, previous studies found this decomposition to partition the flow in a physically useful way.

The possibility of rotating the eigenvectors was rejected because each of the arguments for rotation cited by Richman (1986) is not applicable in this study. *Domain shape dependence* involves predictable, repeating patterns in the sign of the PCs. This is apparently a problem in some studies which use modes of PCA which include varying stations in a search for geographic patterns, in particular. In this study, we do find quite different sequences of the signs of the principal components, so they are apparently reflecting covariation in the data, rather than domain shape dependence.

The second factor is *subdomain stability*, which refers to the ability of the PCA to reproduce the results shown when only a subset of the data is used. This was tested by carrying out the PCA for each leg split into two and comparing with the PCA for the entire leg. The results were largely the same — legs with a predominant horizontal mode in EV #1 retained the horizontal mode, while legs with substantial vertical motion in EV #1 exhibited significant vertical motion there, as well.

The potential problem of *sampling errors* involves the retention of eigenvectors

with closely-spaced eigenvalues, which is not a problem here as we have only four eigenvectors with generally well separated eigenvalues; we are mostly interested in the leading eigenvector. The final factor to consider is the ability of the PC to reproduce relationships which are expressed in the original data and its correlation matrix. The results reported here follow quite closely our expectations upon examination of the time series plots and the correlation matrix. A final comment about rotation will be presented in the next section.

c. Results

Recall that flight 3 was largely dominated by a directional shear zone with some turbulent patches at the top of a shallow boundary layer, while flight 5 was characterized by substantial speed shear in the deeper boundary layer. Eigenvectors which have small coefficients for w are dominated by horizontal flow if u and/or v are large. Most of the legs for flight 3 exhibit such a behavior (figure 3.9), with the coefficients of w almost a factor of ten smaller than those for u and v. This is a result of the very strong stratification present in the SESAME cases analyzed here.

The first eigenvector of legs 1-6 reflect the suppression of vertical motion by the stratification. Beginning with leg 7 (one half-hour after sunrise), the turbulence begins to be influenced by the surface heating. Leg 9 and leg 4 on the subsequent morning (fig. 3.9b) seem to be high enough above ground to also represent suppression by stratification and are included in the analysis. The first eigenvector explains from 35 to 50% of the total variance, and its eigenvalue is much larger than the second eigenvalue (fig. 3.10).

For those legs where w is not important in EV #1, w is *the* dominant variable in EV #2 (fig. 3.11 and 3.12). A pattern of horizontal flow in EV #1 and vertical motion in EV #2 is quite common for the legs of 5 May. Mahrt (1985) shows how various flow features can be described based on the combination of signs recovered in the eigenvectors. A common feature of the legs is that the coefficients for v and T are of the same sign, while

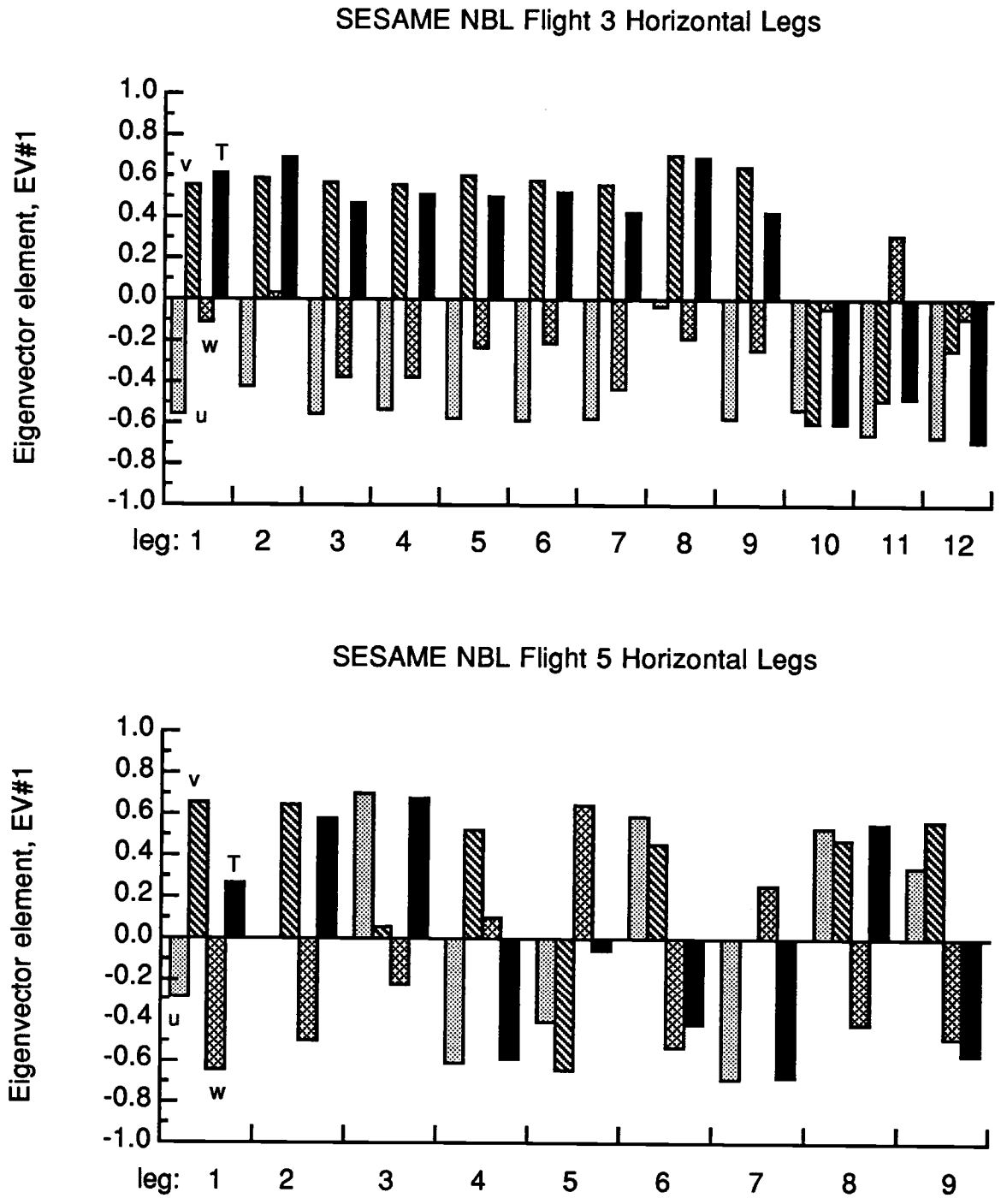

Figure 3.9. Elements of the first eigenvector for all horizontal legs (a) for flight 3 (5 May) and (b) for flight 5 (6 May).

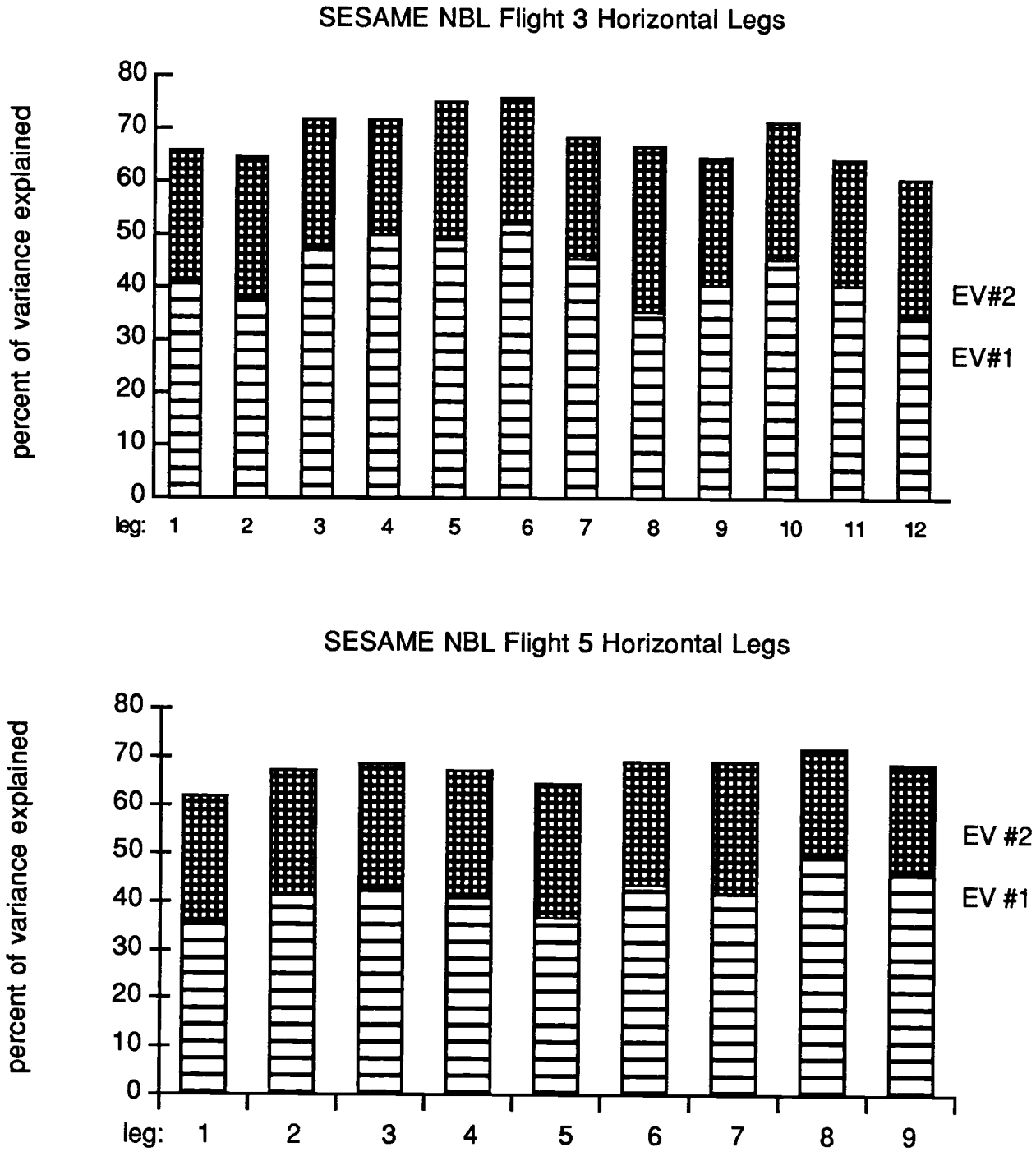

Figure 3.10. The percent of variance explained by the first two eigenvectors for all horizontal legs (a) for flight 3 and (b) for flight 5.

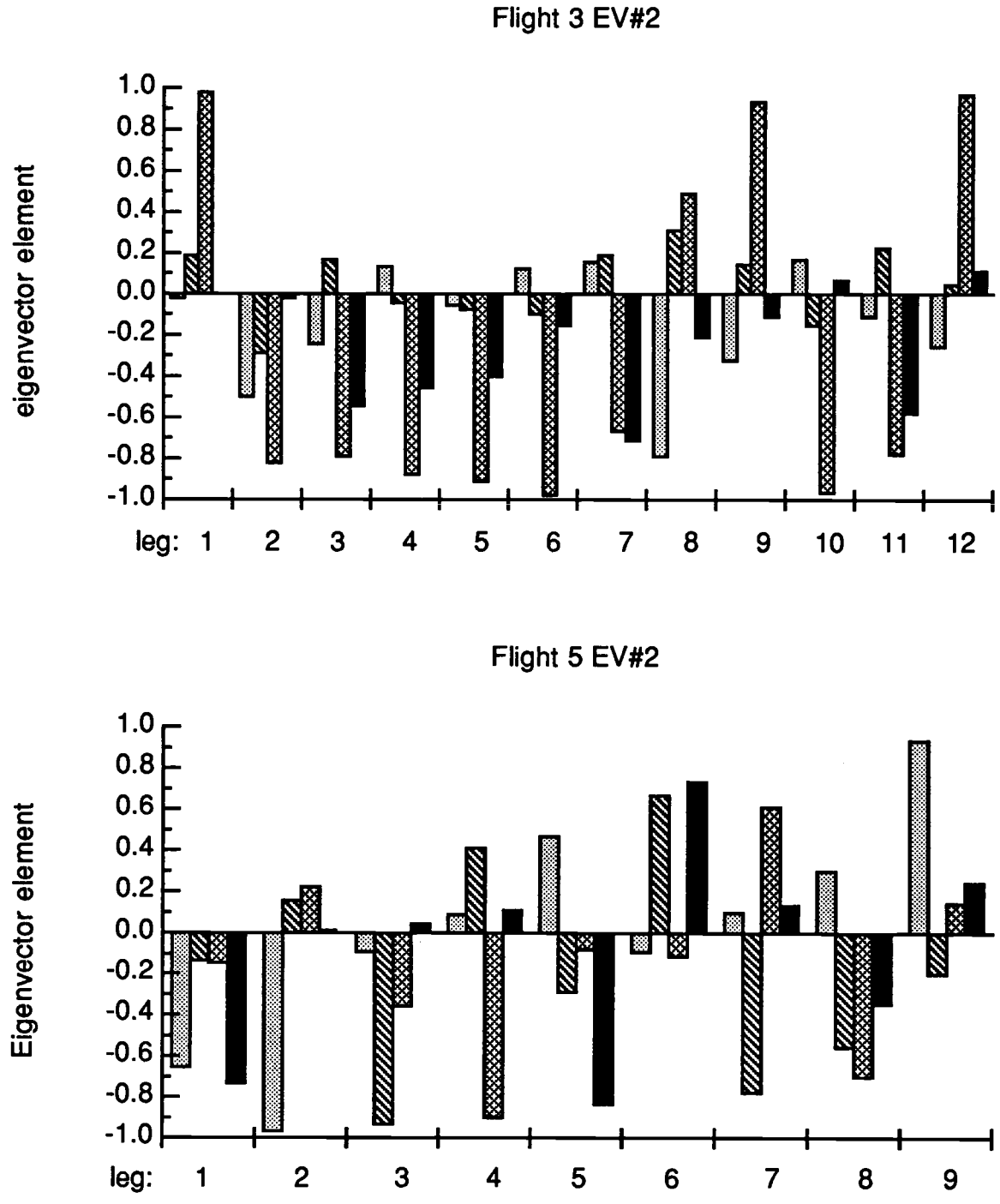

Figure 3.11. As in Fig. 3.9 but for the second eigenvector.

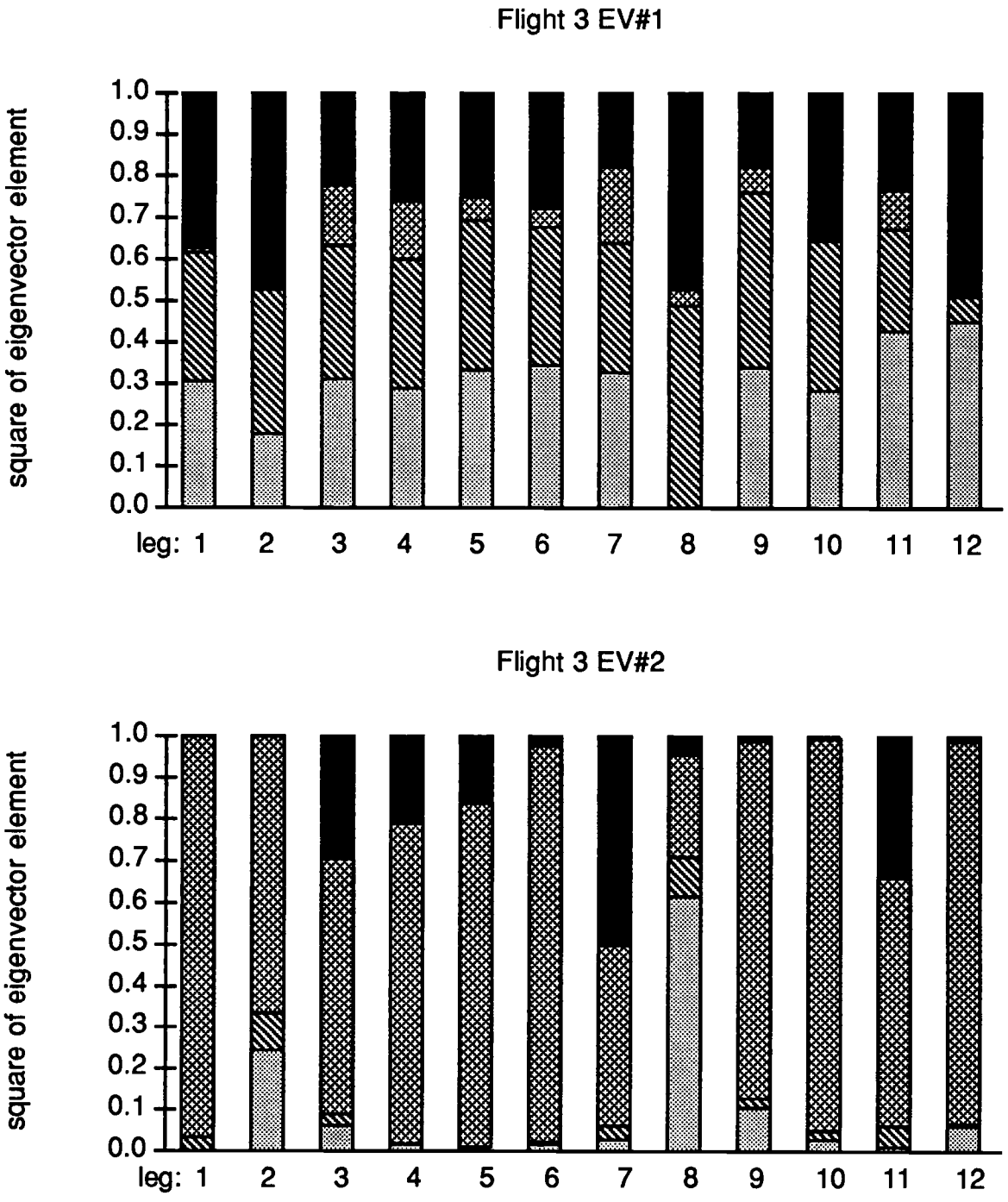

Figure 3.12. The composition of the eigenvector, depicted as the square of the eigenvector element. Shading convention is as shown in Fig. 3.9; stacking order from the bottom is u, v, w, and T. (a) the first eigenvector for flight 3; (b) the second eigenvector for flight 3; (c) the first eigenvector for flight 5; (d) the second eigenvector for flight 5.

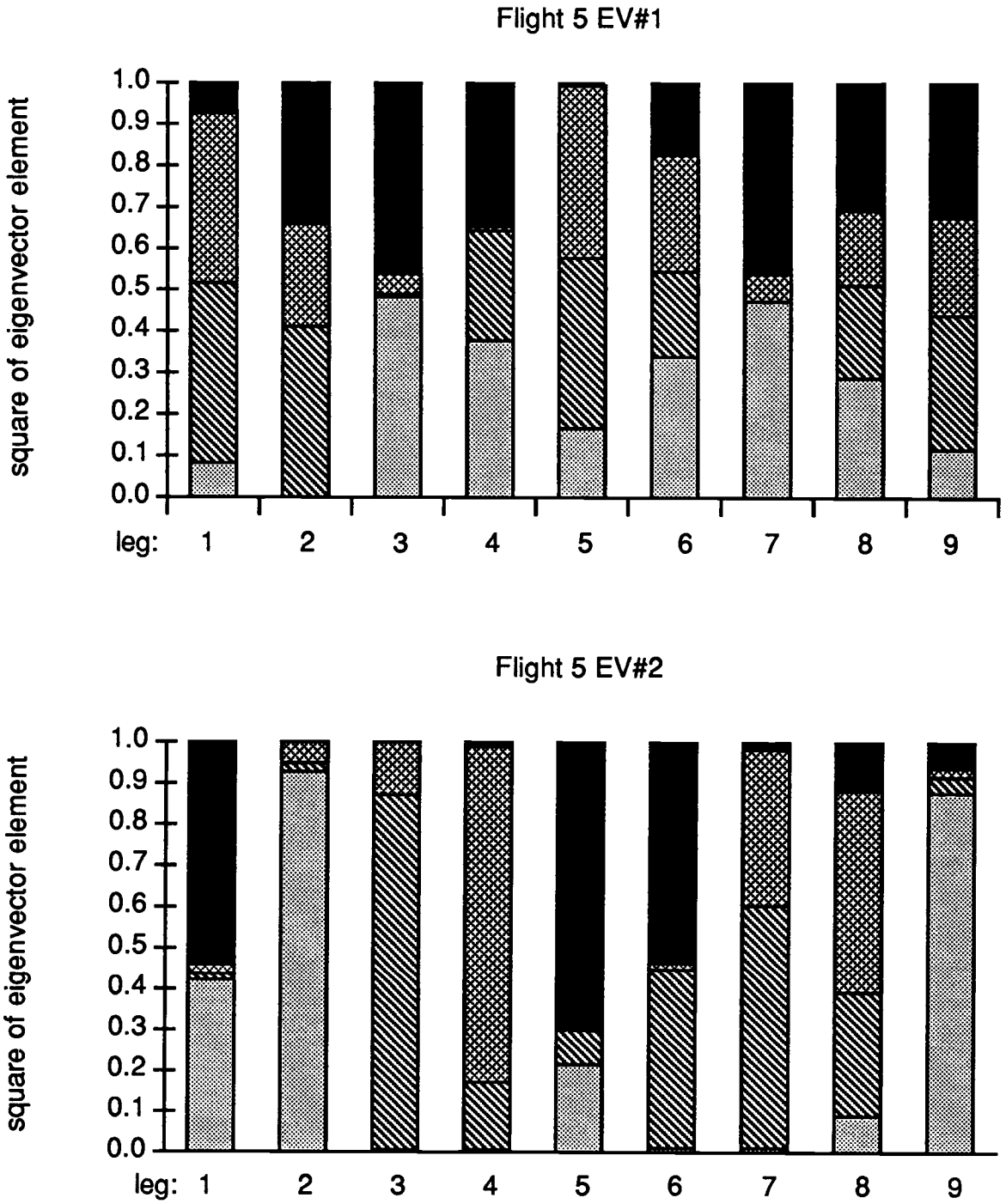

Figure 3.12/continued

u is of opposite sign. The horizontal dominance of the eigenvectors for most legs of 5 May is most clearly illustrated in fig. 3.12. The very small impact of w and balanced contribution of u and v is seen in only one leg from 6 May. The physical pattern suggested by this first eigenvector is one of alternating cold northwesterly/warm southeasterly flow, with little vertical motion. Of course, the entire eigenvector can be multiplied by minus one without changing the interpretation.

The time series of PC #1 for several legs (Fig. 3.13) suggests regular or periodic behavior. The pattern suggested by the EOF coefficients will not appear in the time series of the principal component, but instead will be seen in the loadings of the principal component, which are the elements of the correlation matrix between the i^{th} loading and the j^{th} variable. They are related to the so-called expansion coefficients (Mahrt, 1985); the square of the loadings can be used to assess statistical significance of each variable in each principal component (Wallace and Dickinson, 1972). Figure 3.14 shows the loadings of PC 1 plotted against PC 2 for all ten legs which are dominated by horizontal motion (in the first eigenvector). There are a total of 40 points plotted, as there are four loadings per leg, one for each variable. This type of plot is useful for making a determination of whether to rotate the PCs or not, as shown by Richman (1986). Clustering of points about the axes show structure in the EV matrix, while plots which show many points clustering on a diagonal would suggest that rotation of the eigenvectors is necessary. The points form an elliptical pattern, with clustering about the PC 1 axis, where the horizontal motion is dominating; these are the u, v, and T loadings of PC 1. The points clustering on the PC 2 axis are the w loadings for PC 2. The off-axis points are the remaining loadings. Although this plot does not clearly illustrate persistent simple structure, it does not suggest that the EV matrix was based on random input data, nor do we find points clustering on a diagonal line.

The repetitive flow structure illustrated in fig. 3.13 strongly the possibility of some type of wave motion or coherent structure (Lumley, 1981). This validates in part the

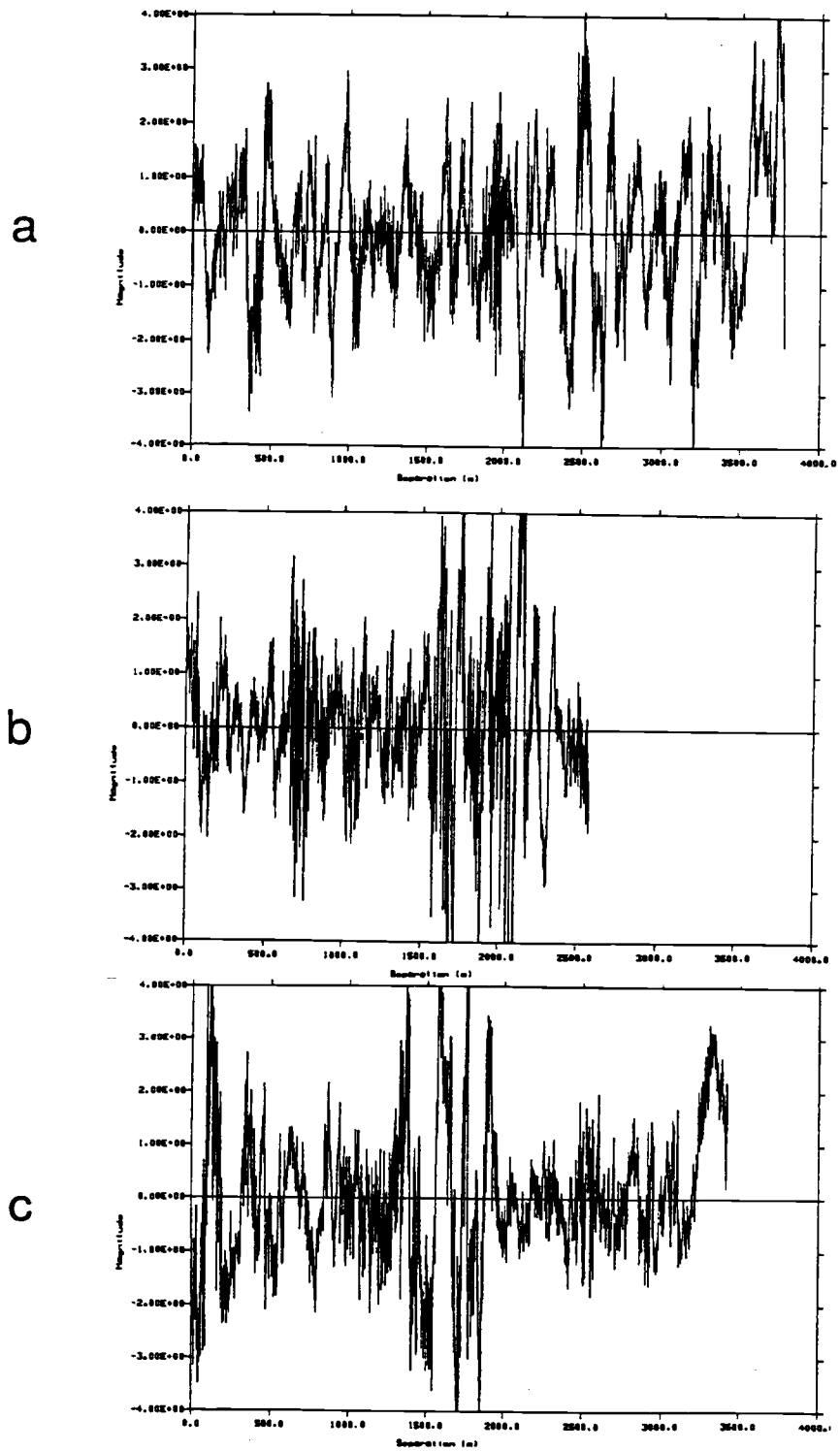

Figure 3.13. Time series of the unsmoothed first principal component for several legs from flight 3. (a) leg 1; (b) leg 4; (c) leg 10.

spectral analysis, which showed significant variance at wavelengths on the order of 400 m. The principal component analysis described in this section will be utilized further in Chapter IV as a sampling technique, in an effort to examine the dynamics of the these structures.

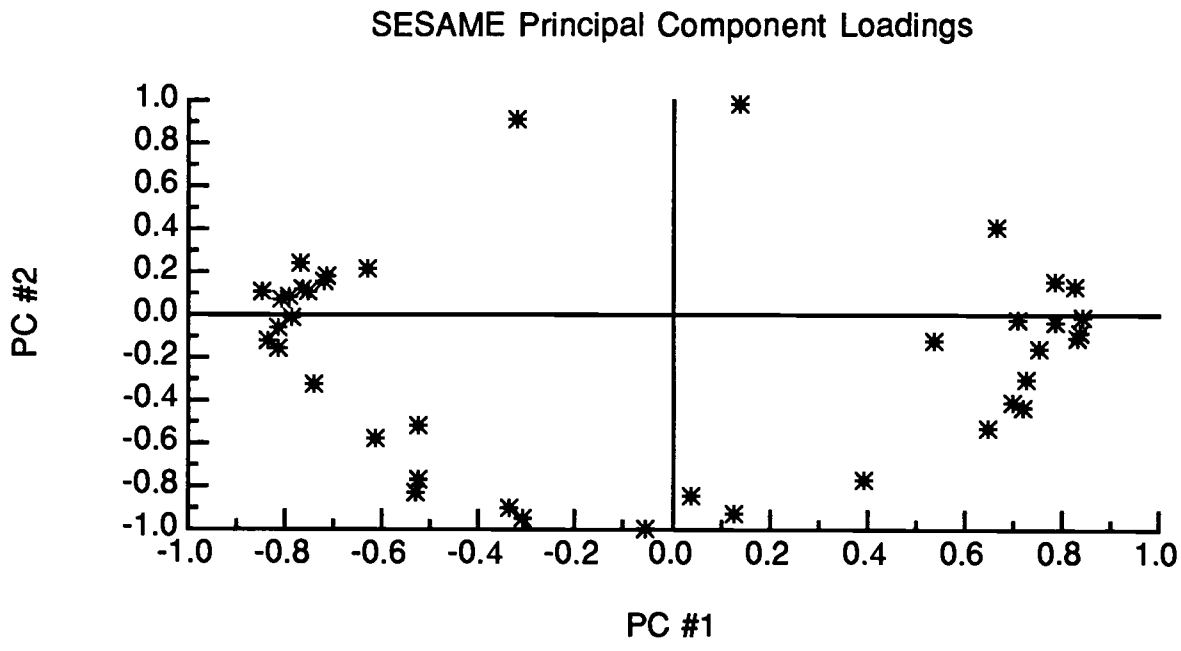

Figure 3.14. Loadings of the first and second principal components for all ten legs which are dominated by horizontal motion. The forty points plotted represent correlations between the i^{th} principal component and j^{th} variable, hence there are forty points. See text for more details.

4. Correlation and structure functions

Two final data analysis techniques that have received widespread popularity in the analysis of turbulence data are the correlation function and a statistic derived from it, the structure function. Some of the models of the autocorrelation function for turbulence are summarized by Townsend (1976). If turbulent eddies are present in the sample of data one has collected, the autocorrelation of variables such as the velocity components should start large and fall off to zero. This decay of the autocorrelation coefficient with separation distance should be quite rapid for small eddies and gradual for the larger eddies. The cross-correlation function can also be examined in a similar way. Those lags which have the highest cross-correlations are related to the phase lag of maximum coherence in classical spectral analysis.

The correlation function has seen much use in turbulence studies, both in analysis where it may serve as a test function for conditional sampling (Townsend, 1976) and modelling applications as in diffusion studies (Lamb, 1982). There are disadvantages to its application in diagnostic studies of stratified turbulence, however, as it performs well when gradients are smooth. Such a feature is not a characteristic of the data in this study.

While the correlation function analysis is sometimes useful, a related approach which also overcomes some of the problems of spectral analysis is available. The structure function was used by Kolmogorov (1941) in his pioneering analysis of turbulence in the inertial subrange. It may be defined as

$$D^n(r) = \overline{\left(\varphi(x+r) - \varphi(x)\right)^2}^{\frac{n}{2}} ; \qquad (26)$$

where r is the spatial lag or separation distance. Normalized structure skewness (n=3) and structure kurtosis (n=4) may also be studied, as in Frisch and Sulem (1978), although significant sampling problems mount as n gets large. It has been shown that D(r) has a 2/3 slope in the inertial subrange (compared to the -5/3 slope for conventional spectra), hence it

is a useful analytical tool for fully-developed turbulence.

Although the family of structure functions will not be used to any great extent in this study of highly intermittent turbulence, a form of structure function will be used in Chapter V to identify narrow zones of strong shear at boundaries of coherent structures.

5. Discussion

This chapter has described the data analysis techniques used in an exploratory investigation of the dynamics of resolvable microscale motion in the very stably-stratified boundary layer of SESAME NBL.

Spectral analysis is the standard analysis technique in turbulence investigations. For more than thirty years, spectra have been presented for motions on all spatial and temporal scales, and this has been particularly useful for intercomparison of experimental data. It is partially in this spirit that spectral analysis has been included in this study. The shortcomings of spectral analysis are often overlooked by researchers, and in the case of intermittent turbulence with no spectral gap, results are very tentative and dynamical inferences should be made carefully.

Analysis of the cross-spectrum is very important in studies which emphasize spectral analysis. However, interpretation of the quadrature spectrum is not very straightforward, in my view, so an analysis of the rotary spectrum is included in this study. The rotary spectrum provides a more intuitive framework for interpretation of the wind hodograph. The examples presented in this chapter show how useful this method can be for analysis of small-scale atmospheric motions, where it has not been used before. However, its promise lies more in application to data collected under conditions where sampling problems would be not as great, such as in well-developed turbulence with a well-defined spectral gap.

Eigen techniques have been shown in the past to be a useful approach for the analysis of turbulent flow fields. By computing the eigenvalues and eigenvectors of the unlagged correlation matrix for u, v, w, and T, it became immediately apparent that several of the horizontal flight segments flown during SESAME NBL were dominated by structures with wavelengths of about 500 m and very small aspect ratios. Principal component analysis has been carried out for the legs with horizontal structure, and some

features are brought out which are not readily apparent by simple examination of the time series of the data. The periodic nature of the horizontal structure is elucidated by the PCA, with a rather consistent pattern over the course of seven flight legs. The pattern is seen to repeat high up in the boundary layer on the following morning, when the synoptic-scale pattern is quite different and the boundary layer is much thicker than the previous morning.

The above analysis techniques are applied in the next three chapters. Chapter IV will present a new conditional sampling technique which is based on the principal component analysis. In Chapter V, some of the methods described and used in this chapter will be adapted for use in the zones of selected samples which appear to have concentrated dynamics. It will be seen that the results of this analysis and other studies of turbulence in the SBL strongly suggest improvements to existing formulations for the parameterization of turbulence in numerical models. Chapter VI is an initial effort to improve such a formulation for ultimate use in a global numerical weather prediction model.

Chapter IV

Analysis of Coherent Structures in SESAME NBL

In this chapter, an objective means of obtaining samples from the flight legs is described. The PCA of Chapter III strongly suggests the presence of a regular feature which should be investigated further. These samples will be first studied by averaging over each flight leg. The compositing procedure is discussed, and statistics of the composites obtained are analyzed. The motivation for further analysis of individual samples will also become apparent.

1. Sampling using a new conditional sampling technique

In this section, the sampling and compositing procedures are described. As mentioned previously, the variables u, v, w, and T are used in linear combination to form the principal components, which are then used to gain some physical insight into the types of phenomena being sampled.

Time series plots of the first principal component, such as the example shown in fig. 4.1, are quasi-periodic and suggest the presence of coherent structures. In order to examine this possibility, samples are obtained by finding local maxima and minima of the smoothed leading principal component. Each sample of twenty points contains ten equally-spaced points between adjacent maxima and minima (or vice versa) and another ten equally-spaced points from minima to maxima. Once the sample position is identified, actual samples are selected from un-normalized data as explained below. Table 4.1 provides information about the samples obtained using this procedure.

This method of utilizing the shape of the leading principal component to select the samples used for the composite amounts to a "natural" conditional sampling technique. Such a technique is desirable as no specific *a priori* assumptions about the scale of the data are necessary except for the detrending. Most conditional sampling techniques require

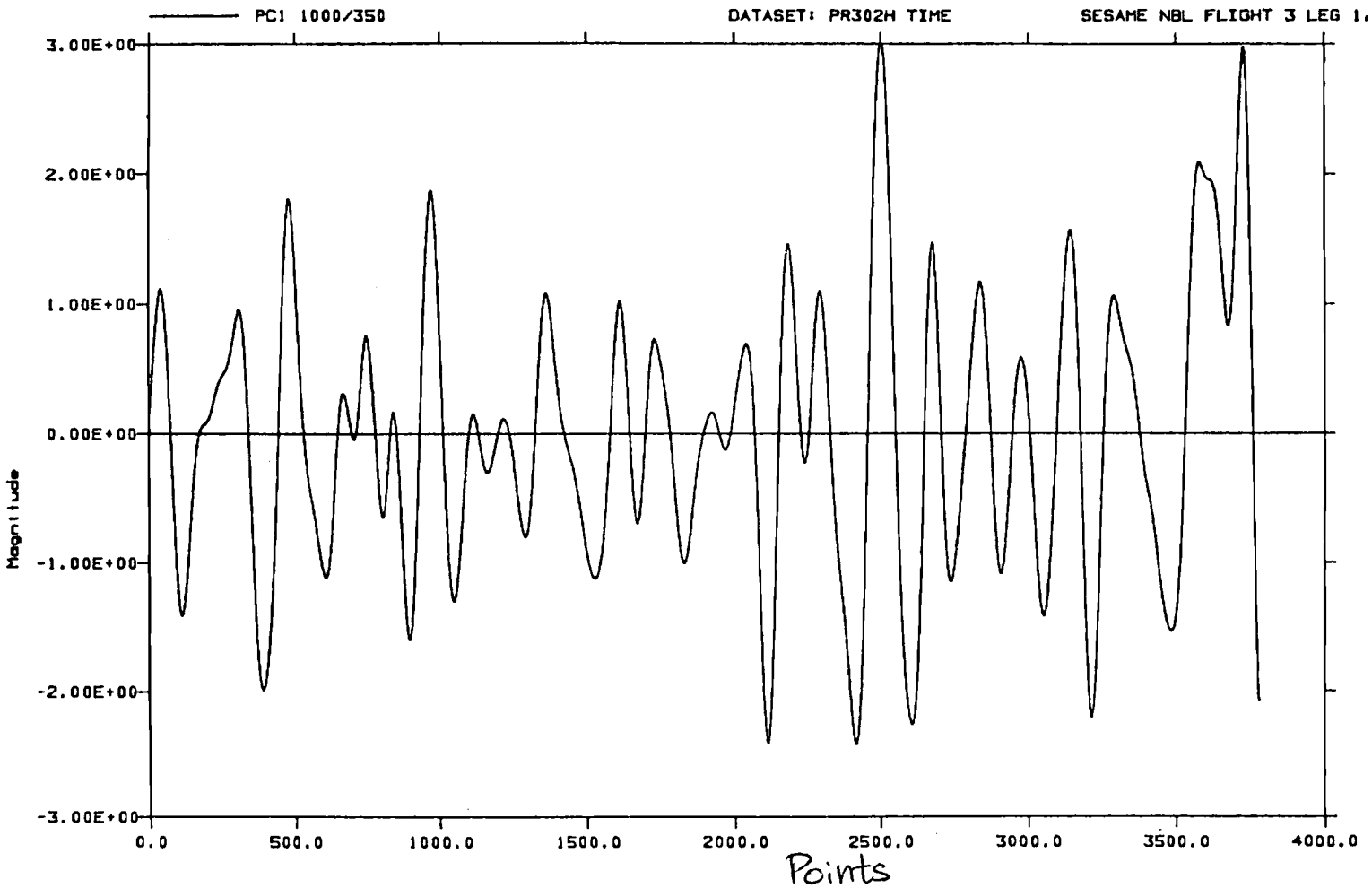

Figure 4.1. Time series of the first principal component for leg 1, flight 3, smoothed with a low pass filter with a cutoff wavelength of 350 m.

Table 4.1

Sample Statistics by Flight Leg

Flight	Leg	Samples Taken	Samples Rejected	Scaling Distance (m) N	Scaling Distance (m) S	Composite width (m)	% of leg in samples
3	1	20	1	7.3	7.8	528.5	79.9
3	2	25	2	7.1	7.3	505.7	91.5
3	3	19	5	7.1	7.8	522.6	70.4
3	4	19	0	6.3	5.9	424.8	89.8
3	5	22	5	7.2	7.5	513.4	82.9
3	6	20	6	6.3	6.2	437.3	73.1
3	9	26	1	6.2	6.9	459.3	90.1
3	10	20	3	6.8	7.2	490.9	81.9
3	11	29	2	6.5	6.4	451.1	93.1
5	3	16	0	7.0	7.1	495.0	83.6
Total		216	26				
Weighted average				6.8	7.0	481.2	84.4

Scaling distance is listed in terms of observational points; **N** refers to northern end of composite and **S** refers to southern end of composite.

selection of a sampling criteria based on statistics gathered from the original data; some degree of subjectivity is common for the selection criteria. Use of an intermittency factor is common (e.g., Khalsa, 1980, Shaw, 1983), where the data is considered only if the parameters or a given variable exceed a threshold value fixed by the investigator; the fluid is either turbulent or it is not.

Some other methods of conditional sampling include the Variable Integration Time Averaging (VITA) method (e.g., Blackwelder and Kaplan, 1976, Chen and Blackwelder, 1978, Schols, 1984) and the continuous weighting technique of Mahrt and Frank (1987). These methods are more sophisticated than those involving simple on/off intermittency factors, but they also require some subjective selection of the sampling criteria. If it can be said that information contained in the principal components represents physical structure in the data, then utilizing them to define the sampling criteria would represent a more objective data analysis procedure. This is especially useful under conditions of strong static stability when turbulent events are not so distinct (i.e., from wave modes, etc.) and specification of semi-objective selective sampling criteria might be difficult.

Let the independent variables x and k represent, respectively, position within a sample and sample number. We can then express the value of any high-pass filtered function Φ by

$$\Phi(x,k) = \phi(x,k) + \phi_o(k) \ , \tag{1}$$

where

$$\phi_o(k) \equiv \frac{1}{X} \int_0^X \Phi(x,k) \ dx \ . \tag{2}$$

Thus ϕ represents a variable whose sample mean (ϕ_o) has been removed.

We will now decompose ϕ into two parts — a composite ($\phi_c(x)$) or average of samples at each of the twenty points and the deviation series ($\phi''(x,k)$). These variables are formally defined as

$$\phi_c(x) \equiv \sum_{k=1}^{K} \phi(x,k) \ , \tag{3}$$

$$\phi''(x,k) \equiv \phi(x,k) - \phi_c(x) \ , \tag{4}$$

where K is the total number of samples taken. Note that

$$\sum_{k=1}^{K} \phi''(x,k) = 0. \tag{5}$$

Based upon definitions (2) through (4), the (biased form of the) variance of the function ϕ may be written

$$\mathrm{Var}(\phi) = \frac{1}{K} \sum_{k=1}^{K} \frac{1}{X} \int_0^X [\phi_c(x) + \phi''(x,k)]^2 \, dx \, , \tag{6}$$

with X the sample width as used above. This variance includes two terms which have rather simple interpretations. The variance of the composited structure is

$$\mathrm{Var}(\phi_c) \equiv \frac{1}{X} \int_0^X \phi_c^2(x) \ dx \ . \tag{7}$$

which is independent of k by (3). The variance due to deviations of a given sample structure from the composited structure is

$$\mathrm{Var}\left(\phi''(k)\right) \equiv \frac{1}{X} \int_0^X \phi''^2(x,k) \, dx \, . \tag{8}$$

The remaining term,

$$\frac{1}{X} \int_0^X \frac{2}{K} \phi_c(x) \left[\sum_{k=1}^{K} \phi''(x,k) \right] dx \ , \tag{9}$$

vanishes due to (5).

As a practical measure, there will only be a finite number of points per sample taken

(J = 20 here). For the discrete case,

$$\frac{1}{X}\int_0^X \varphi \; dx \Rightarrow \frac{1}{J}\sum_{j=1}^{J} \varphi \quad . \tag{10}$$

Substitution of (7) and (8) into (6) and use of (5) results in

$$\mathrm{Var}(\phi) = \mathrm{Var}(\phi_c) + \frac{1}{K}\sum_{k=1}^{K} \mathrm{Var}\left(\phi''(k)\right) \quad . \tag{11}$$

A study of the partition of the variance in (11) is a classical analysis of variance (Panofsky and Brier, 1968). Before this is done, however, we may wish to study the influence of each individual sample on the suitability of the final composite. In order that our composite be most meaningful, we must maximize the variance of ϕ_c and minimize the sample deviation (sometimes called the within-sample) variance. The ratio of within-sample variance to composite variance for a given sample will be called the *sample relative variance*,

$$\Re_k = \frac{\mathrm{Var}\left(\phi''(k)\right)}{\mathrm{Var}\left(\phi_c\right)} . \tag{12}$$

$\Re$ can be computed for each of the four variables for each sample. The $\Re$'s could be tracked in an iterative procedure whereby any sample which has a disproportionate share of the deviation (within-sample) variance could be discarded, forcing a recalculation of the composite. We could then calculate the composite again with less samples, until an acceptable ratio of composite to sample deviation variance ($\sim\Re^{-1}$) is obtained. This is but one method which might be used to enhance our understanding of the composite and the role that individual samples play in its determination. In fact, it will be tested shortly.

The importance of each variable in the leading principal component will likely determine this final sample rejection procedure. For example, horizontal flight legs with unimportant vertical motion in the leading eigenvector have been selected. Most of these legs are from the morning of 5 May, but one leg from the morning of 6 May falls into this

category. Small values of $\Re$ for u and v are desirable if the loadings of u and v are large in the first principal component; we need not consider the impact of w. Recall that in each of the flight legs chosen for further analysis here, the second eigenvector is dominated by w.

Table 4.2 illustrates the results of the analysis of variance computation for the leg composites (in plain type). The results are basically as we would expect from examining the coefficients of the eigenvectors. Since the leading eigenvector is dominated by u, v, and T, the percent of variance explained by the composite for w should be much lower than for these variables. Only about one-fifth of the total variance is explained by the composite for the other three variables. This fairly low signal-to-noise ratio is a characteristic of turbulence.

It should be noted here that the composites are an inhomogeneous collection of samples based on a principal component which is trying to maximize percent of variance explained. The method might be improved by further eigenvector decomposition, or by a less sophisticated approach, involving elimination of samples from the composite which have the least in common. For example, the results could be greatly improved by omitting the samples with largest values of $\Re$. To illustrate the wide disparity from one sample to the next, the percent of variance explained for each sample of one flight leg (leg 1 of 5 May) is shown in Table 4.3.

A semi-objective method of sample elimination can be developed by constructing the frequency distribution of $\Re_u$ and $\Re_v$ and using the value at which the relative frequency drops off to near zero as a cutoff value. This distribution for all 216 samples from flight 3 is shown in Figure 4.2. The maximum value allowable for $\Re$ will be 7, above which samples will be eliminated from the newly constructed composite. Using this criteria for omission of samples, we would expect to find improvement for leg 1, for example, if samples 7, 11, and 15 were eliminated (see Table 4.3).

The analysis of variance results for the second phase of the analysis are also shown in Table 4.2 in italics. Some improvement is noted, but not in all legs. While the new composite is substantially improved, for legs 1, 4, and 9, in particular, in terms of the

Table 4.2

Percent Variance Explained by Composites: Leg Averages

		% variance explained for each variable				
Flight	Leg	u	v	w	T	K
3	1	19.98 *22.94*	36.92 *37.29*	3.14 *1.91*	27.10 *32.76*	20 *17*
3	2	18.21 *23.16*	34.73 *30.61*	3.77 *5.05*	20.89 *15.50*	25 *21*
3	3	15.59 *18.49*	20.34 *20.29*	8.38 *12.06*	11.98 *13.56*	19 *16*
3	4	12.55 *13.78*	21.58 *26.15*	12.55 *9.38*	21.97 *27.71*	19 *14*
3	5	24.96 *21.26*	30.32 *26.69*	9.42 *9.01*	15.38 *13.38*	25 *20*
3	6	25.33 *24.74*	28.36 *26.36*	9.70 *6.48*	17.71 *15.49*	20 *19*
3	9	14.56 *21.22*	16.80 *20.11*	3.74 *6.32*	4.42 *3.57*	26 *20*
3	10	19.09 *20.49*	23.33 *17.68*	4.14 *5.73*	28.62 *24.38*	20 *15*
3	11	15.63 *16.15*	15.21 *12.00*	6.05 *9.14*	14.39 *10.77*	29 *18*
5	3	27.32 *30.14*	20.67 *22.96*	8.40 *8.63*	21.30 *22.32*	16 *15*

Table 4.3

Sample Relative Deviation Variance, $\mathfrak{R}$: Leg 1, 5 May

Sample#	$\mathfrak{R}_u$	$\mathfrak{R}_v$	$\mathfrak{R}_w$	$\mathfrak{R}_T$
1	5.477	1.924	29.400	3.174
2	0.733	1.960	19.499	0.873
3	0.898	1.006	62.408	1.061
4	2.538	2.180	78.864	2.519
5	1.962	3.567	11.301	2.054
6	5.070	1.819	24.218	0.957
7	13.366	0.495	29.578	4.487
8	1.976	1.092	30.229	2.641
9	6.079	1.001	29.175	2.527
10	1.675	1.048	18.885	1.892
11	8.124	1.933	25.118	5.441
12	4.160	2.012	40.713	6.151
13	1.805	1.430	15.376	6.761
14	3.785	1.236	43.881	2.989
15	7.428	3.885	43.241	2.556
16	5.558	4.101	29.731	2.057
17	1.195	0.537	3.463	0.795
18	1.634	0.514	25.731	1.504
19	1.681	0.760	12.991	1.746
20	4.952	1.664	43.782	1.603

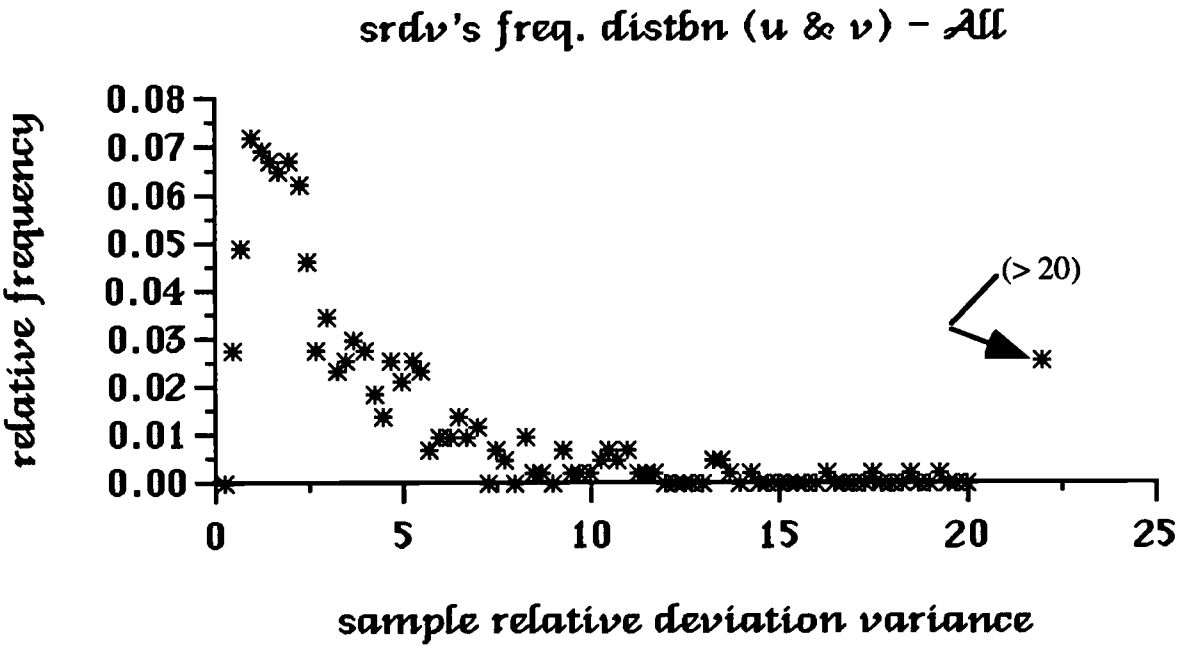

Figure 4.2. Relative frequency distribution of sample relative deviation variance ($\Re$) for u and v for all 216 samples from all ten horizontal flow legs.

percent of variance explained by the composite, for legs 1, 4, and 9 in particular, the results are actually deteriorating for legs 5 and 6. The remaining legs have mixed results. The overall lack of improvement could be explained by noting that even by eliminating one sample with a large fraction of the overall leg variance, the composite can be altered enough such that the newly formed composite can explain less variance than it does initially.

In spite of these mixed results, the compositing procedure is isolating a feature present in a large fraction of the flight legs, particularly on the morning of 5 May. Typically this flow feature explains 20 to 25 percent of the total variance of the variables u, v, and T. In order to better evaluate the importance of the composites, their structure and their dynamical significance are examined in the next section.

2. Analysis of composited structures

In this section, the composited structures are presented and their importance to the boundary layer flow description is examined. Fluxes and variances for the composites are presented and compared to the leg-averaged fluxes and variances, and conclusions are drawn about the type of features present and their dynamical significance. The composites will strongly suggest a dominant regular two-dimensional flow structure which sometimes contains sharp transitions suggestive of microfronts.

The compositing was performed for nine flight legs from the morning of 5 May and one leg from 6 May. There were 216 samples of structures obtained, with 25 other potential samples being rejected either because their length exceeding 1 km (the original cut-off for the low-pass filter) or because the length of either half of the sample was extremely small (< 100 m).

Figures 4.3 illustrate the composited fields for u, v, w, and T and the leading principal component for the legs. These figures clearly suggest the presence of some regular or periodic component of the flow. Its horizontal scale is about 500 m in the composites. Arrows just to the right of the figures indicate the horizontal flow field in plan view (x-y plane). The other set of arrows is the flow field in a longitudinal cross section (y-z plane). There is a weak vertical motion field; it appears to be about 180° out of phase with temperature, corresponding to downward heat flux. The horizontal components are also out of phase. The horizontal wind vector sometimes rotates gradually and other times shifts nearly 180° across narrow transition zones. These transition zones are apparently zones of convergence on the northern end of the composite and are divergent on the southern end, although this is with respect to only one component. Much of the detail in the sampling procedure has been lost, however, because these zones do not always occur at the same relative position (based on the PCA sampling criteria). By averaging over many samples, the zones are averaged in at various locations with respect to position within a sample.

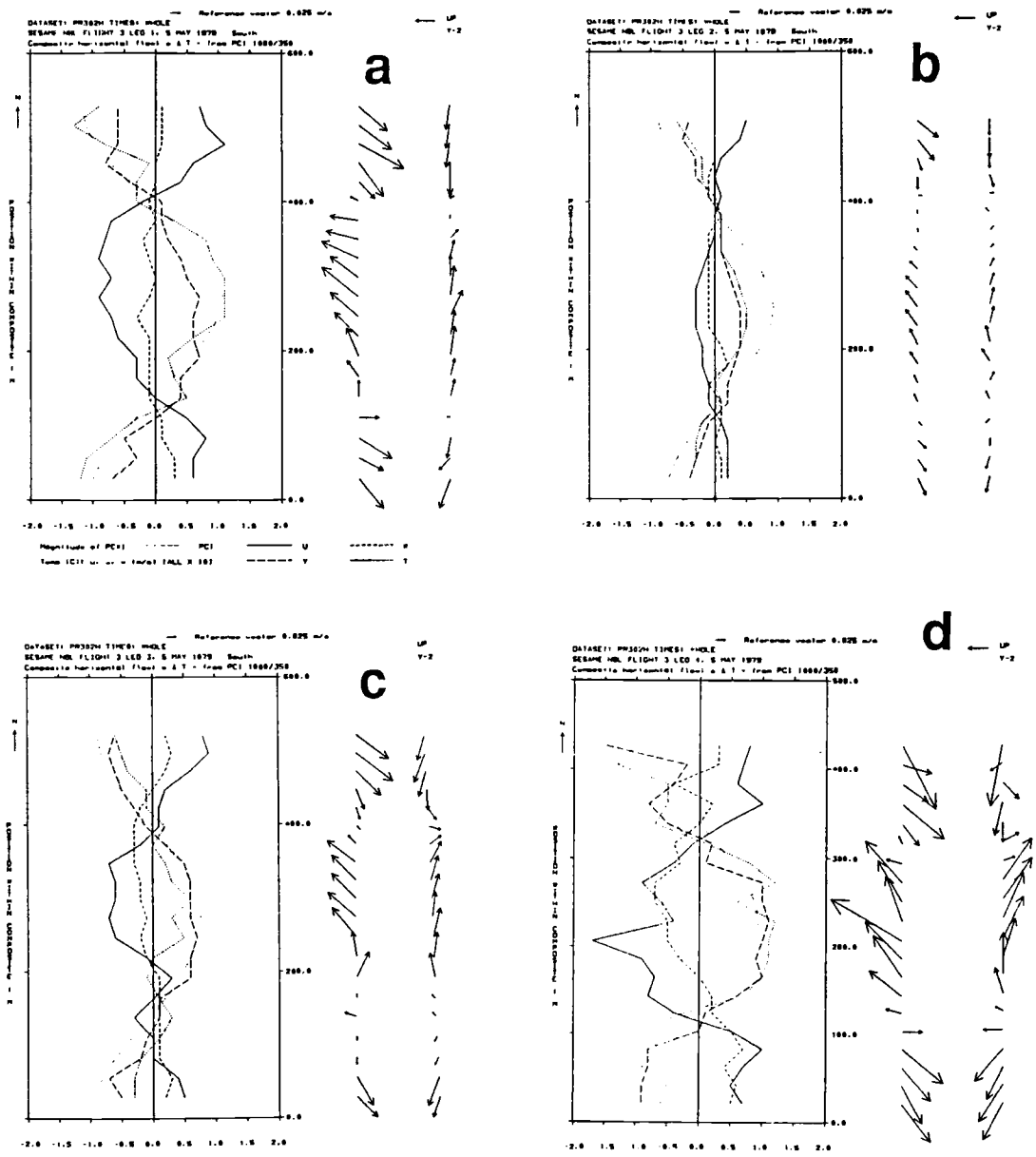

Figure 4.3. Composited horizontal flow (u and v), temperature (T), vertical motion (w), and leading principal component (PC1) for selected legs of flight 3. Arrows at left indicate horizontal flow in "map-view." Arrows to the right indicate a longitudinal cross-section of the flow. Reference vector has a magnitude of 0.25 m/s. Southbound legs are indicated by the word South.

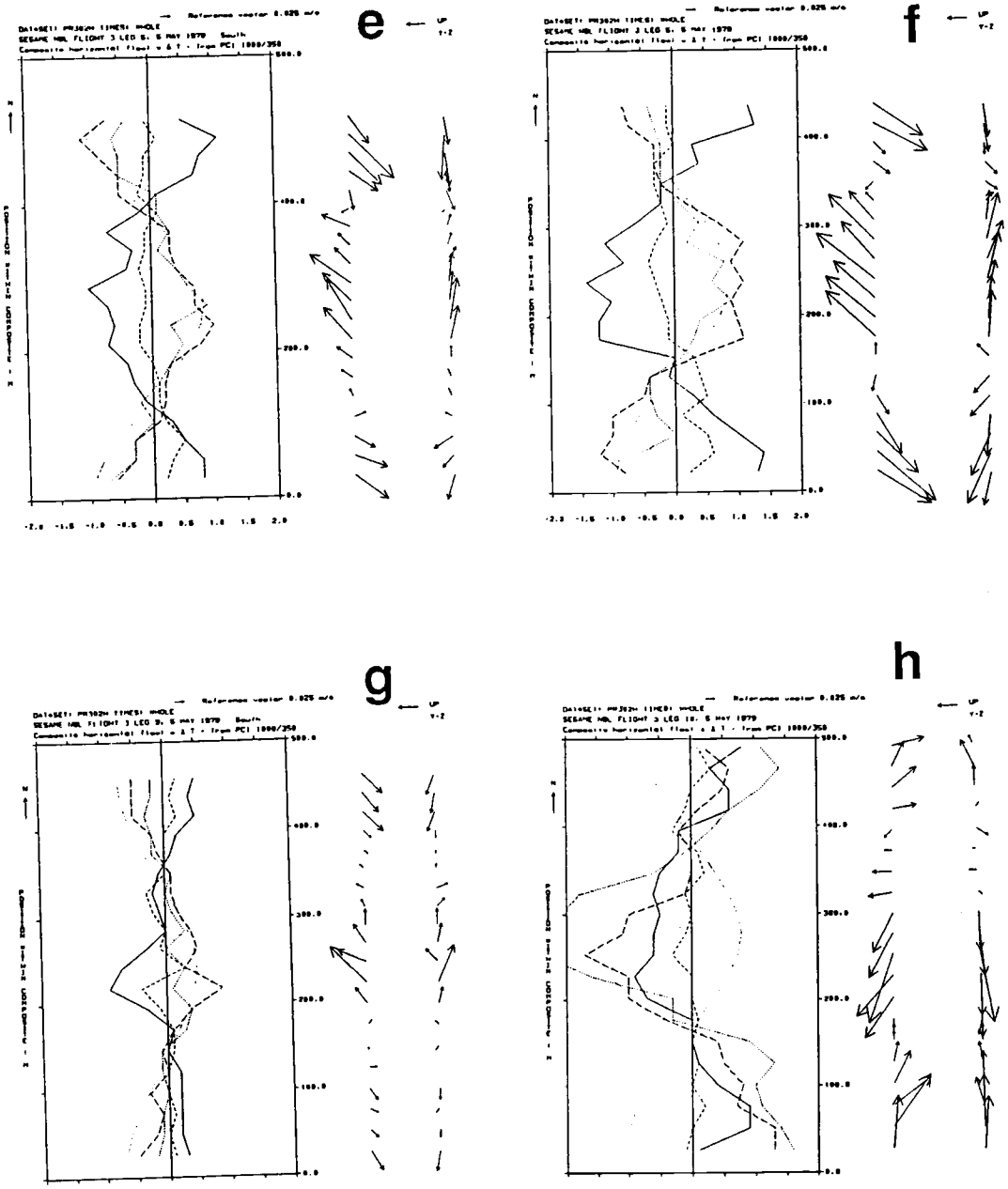

Fig. 4.3. Continued.

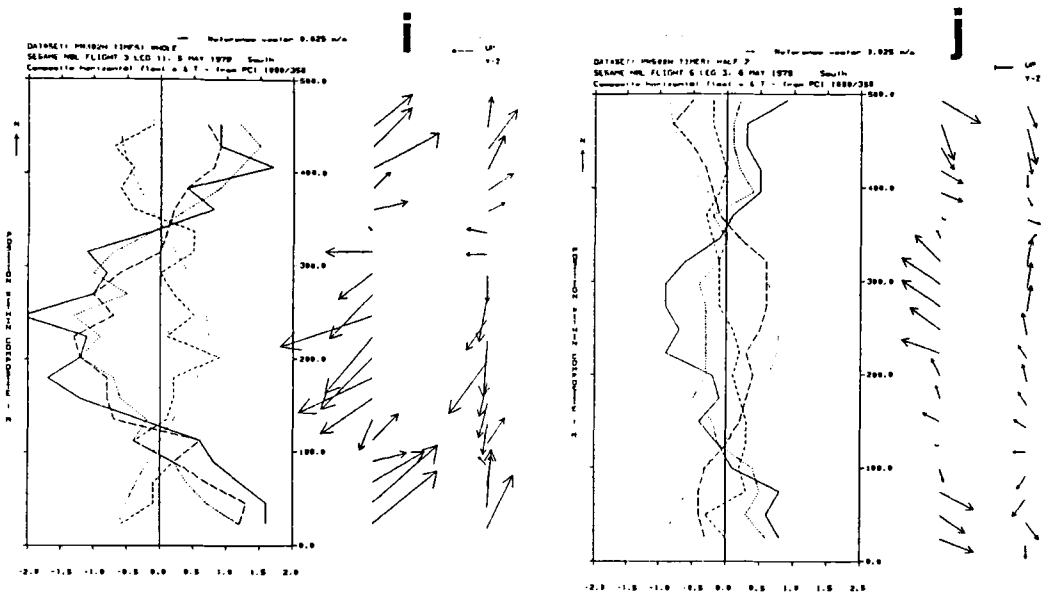

Fig. 4.3. Continued.

For leg 1 (fig. 4.3a), the northern zone exhibits strong changes in the horizontal motion field, while the southern zones illustrates apparent rotation. The cross sections of the flow, shown in the arrows at the far right, illustrate little vertical motion. Across the transition zones we also note that there is a very large temperature change. Leg 3 is a leg with a similar EOF pattern to other legs early on 5 May (fig. 3.9), except vertical motion is not so weak. Vertical motion concentrates in the transition zone (fig.4.3c), and is out of phase with the other variables. This might suggest gravity wave motion although the transition zones are very nonlinear. The temperature change is also quite large across the transition zone. The northern zone exhibits substantial shear in the v component in particular, while the southern zone exhibits little horizontal shear.

It appears that the composites can be classified in two categories based on the relationship between w and T, as is common for studies involving gravity waves. Simple

linear gravity waves would have a 90° phase lag between vertical motion and temperature, such as exists in two legs (figs. 4.3c, 4.3j). However, in most of the legs, composited vertical motion is so weak that it is difficult to determine a preferred phase relationship. It is generally observed that where vertical motion is present, it is often found to be upward in the zones of divergence and downward in the convergence zones (figs. 4.3a, 4.3d). Phase lags of 45° seem to be more apparent here in the composites. There is also substantial asymmetry present in the composites, where the transition zones might be dominated by changes in only one horizontal component (fig. 4.3e). Those legs which have very small values of the composited parameters may be suffering from sampling problems due either to very weak ambient flow or very turbulent flow.

The composites over the individual legs indicate some type of regular significant flow feature of. Certainly some detail is lost in the averaging procedure; this is shown in Figs. 4.4 and 4.5, which show the composites for the first seven legs of 5 May and the last two legs, respectively. These figures illustrate some semblance with Figs. 4.3 but again, the detail is lost. They are quite different from each other, of course, because drainage flow had been almost completely eliminated by leg 10. The transition zones are still in evidence, however.

Some understanding of the flow feature can be qualitatively interpreted by partitioning decaying turbulence in stratified flow into two components (Riley *et al.* (1981); Lilly (1983); and Holloway (1983)). These components are a gravity wave mode which is characterized by little vertical motion and no vertical vorticity; and a vortical mode characterized by its vorticity and lack of horizontal divergence (Müller, 1984).

In many studies of turbulence under stable conditions, oscillations such as the ones shown in fig. 3.1 are often characterized as gravity wave motion, with little further comment. As Müller (1984) suggests, the vortical mode is equally-likely and should be considered more seriously as a possibility; the dynamical implications are quite different. Both gravity waves and the vortical modes are thought to result from collapse of three-dimensional turbulence; whereas the gravity waves may propagate away from the region of

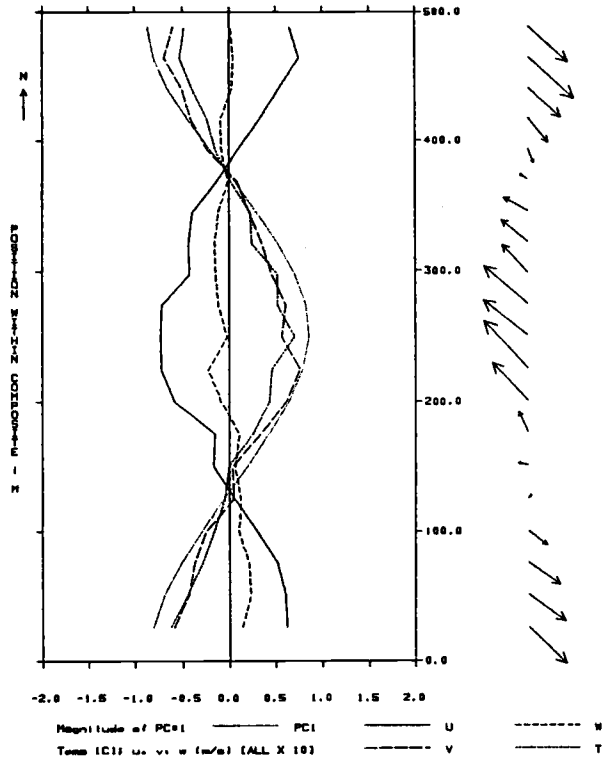

Figure 4.4. As in Figs. 4.3 but for all 151 samples of flight 3 legs 1 through 6 and 9.

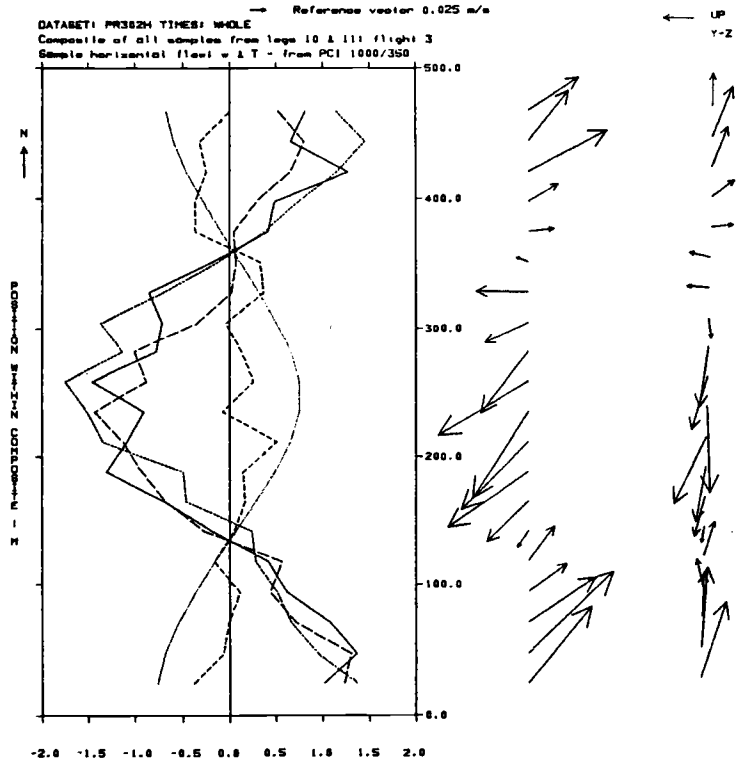

Figure 4.5. As in Figure 4.4 but for the 49 samples of legs 10 and 11.

collapse, the vortical mode may persist with the flow meandering about in the local region. Temperature variations in the present observed flow are significant and strongly related to the horizontal flow field, even though vertical motion is not important, at least in the first principal component, consistent with vortical modes. The present debate in the oceanographic literature about the nature of "fossil turbulence" (Gibson, 1981, 1987; Dillon, 1984; Caldwell, 1986) may be relevant here.

The vertical motion dominates the second principal component, however, indicating that it does play an important role in motions of secondary importance. One might expect to find down-gradient transfer of heat for any vertical circulation present, however, inspection of fig. 3.11a indicates that transport is counter to the gradient for those legs under present study. This is strongly suggestive of the latter stages of shear-driven overturning, as suggested by Mahrt and Frank (1987) in their examination of stronger bora turbulence. In that study, however, vertical motion was very important in the first eigen mode, in contrast to this examination.

Although the aircraft only takes observations in one flow direction (meaning one can only obtain one of two terms for relative vorticity [$\zeta = \partial v/\partial x - \partial u/\partial y$] and horizontal divergence [$\nabla_H \cdot \mathbf{V} = \partial u/\partial x + \partial v/\partial y$]), the two flows are quite different and one can interpret the aircraft data in terms of the differences between these two kinematic régimes. We must also consider active turbulence in the form of transverse overturning circulations induced by the shear at the boundary layer top; this will be explored further in Chapter V.

We will restrict our attention for the moment to the transition zones on the north side of the principal component maximum, where southerly flow converges with northwesterly flow. In the composites of any of Figs. 4.3a-h, we note that the zone is characterized by $\partial u/\partial y > 0$ and $\partial v/\partial y < 0$. If the flow is dominated by simple gravity waves, the flow would also have to be irrotational, requiring $\partial v/\partial x > 0$, which would indicate a need for increasing southerly winds (decreasing northerly winds) as we moved towards the east, as in the idealized gravity wave of figure 4.6. The horizontal scale of a simple gravity wave

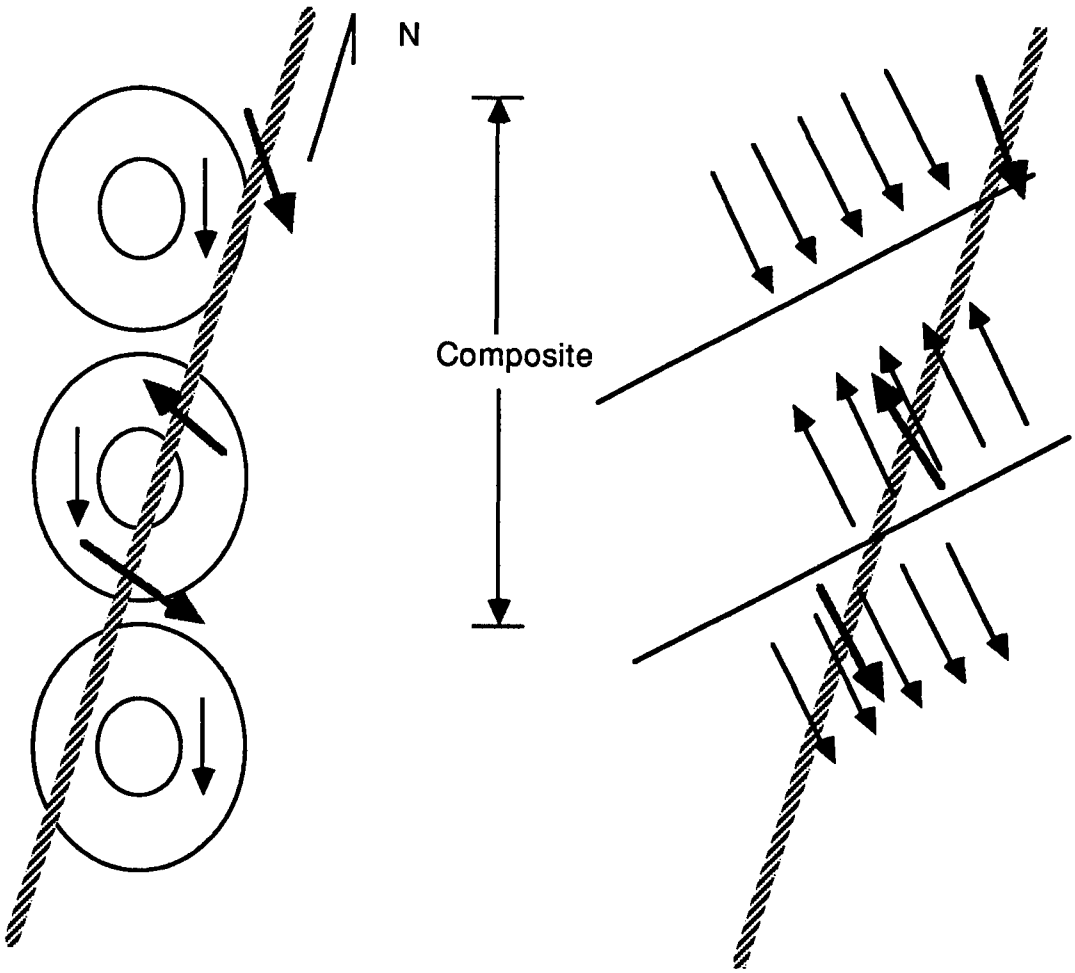

Figure 4.6. Sketch of idealized two-dimensional flows at the top of the stratified PBL. At left is an illustration of the vortical mode, one which can be associated with two-dimensional turbulence and/or meandering. On the right a gravity wave is indicated; this picture could also represent the tops of three-dimensional turbulent eddies driven by shear. The aircraft flight track as in flight 3 is indicated by the heavy dashed line; solid arrows represent relative horizontal flow; dotted arrows indicate relative horizontal flow measured by the aircraft sensors.

can be determined from mass continuity scaling (Gossard and Hooke, 1975):

$$\frac{L}{D} \approx - \frac{V}{W} \quad , \tag{13}$$

where L is the horizontal scale, D is the vertical scale, V is the longitudinal velocity component scale, and W is the vertical motion scale; the last three parameters can be estimated from the data as D ≈ 40 m (flight altitude), V ≈ 0.1 m/s, and W ≈ 0.01 m/s, giving L ≈ 400 m, a value consistent with the composite analysis.

Two dimensional vortical modes would be characterized by horizontal non-divergence and non-zero relative vorticity. With $\partial u/\partial y > 0$, non-zero vorticity would require that $\partial v/\partial x$ be negative, implying the existence of decreasing southerlies to the east (to the right on figs. 4.3). This is completely opposite to what we would expect for simple gravity wave dominance, and yet fig. 4.6 shows a sketch of a possible vortical mode which could be used to justify labelling similar composites vortical modes.

Although some of the composites shown have a clearly identifiable phase lag between temperature and vertical motion of about 90°, as predicted by linear theory for gravity waves, most indicate a much more complicated phase relationship with sharp transitions, probably with waves, transverse overturning, and horizontal vortical motion.

The relationship between the composite function and the flight leg is further studied by examining the magnitude of the various composite fluxes and comparing them to the total leg fluxes. A straightforward method of carrying out this comparison is to plot the composite flux versus the leg flux and analyze these results. This was done for the ten combinations of variables (figures 4.7). The line on each graph is a by-eye fit to the plotted data, the small slopes indicate weak fluxes and variances for the leg composites as a whole, compared to the corresponding flight leg averages. The variances are about an order of magnitude smaller for the composited structure; while the composite fluxes are of the same sign but also quite small. This would seem to indicate either the flow feature being sampled contributes little flux or variance or the averaging procedure washes out much of

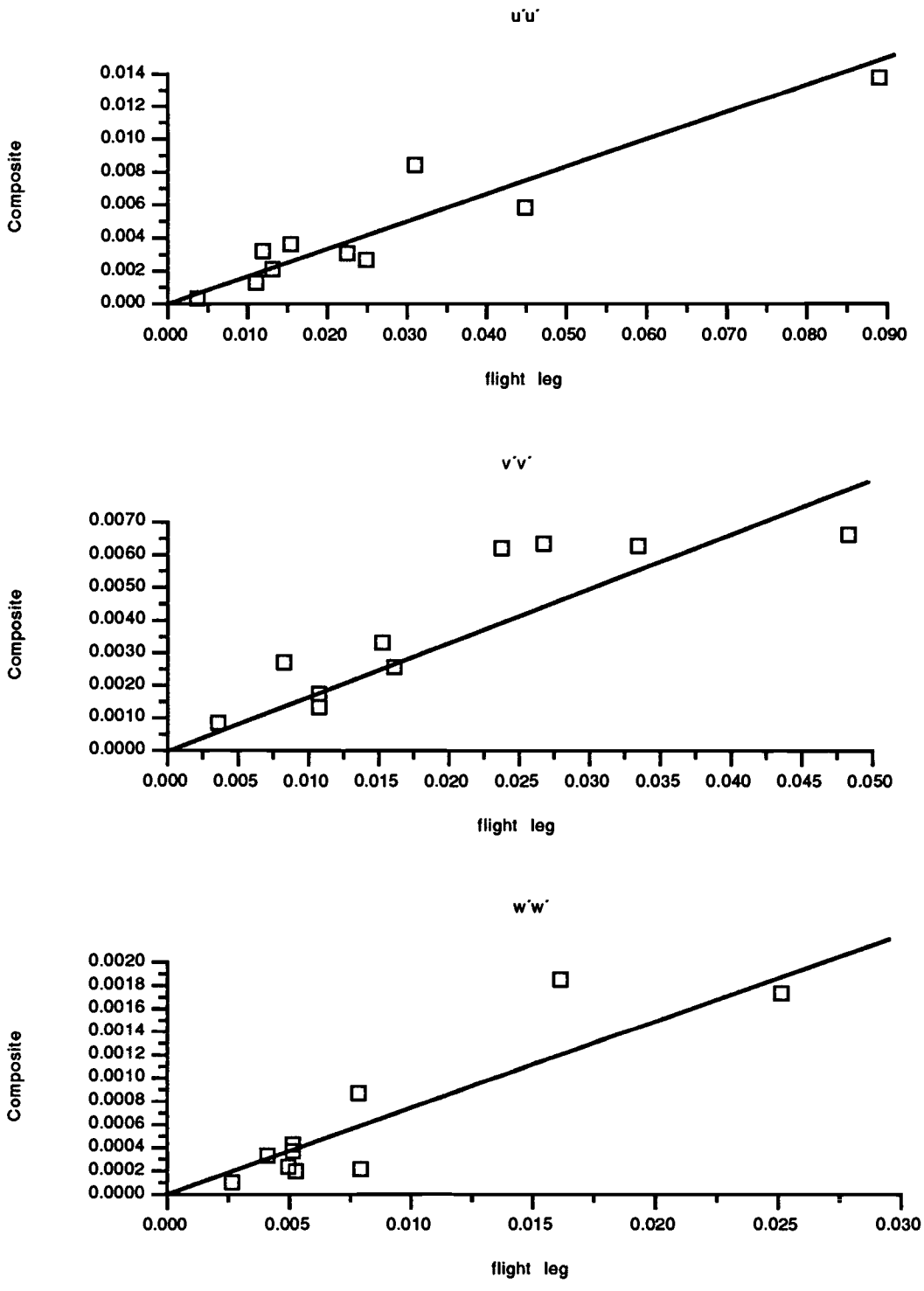

Figure 4.7. Flight leg fluxes plotted against composite fluxes (a cutoff wavelength of 1 km was used for the high-pass filter). The line is a by-eye fit to the plotted data.

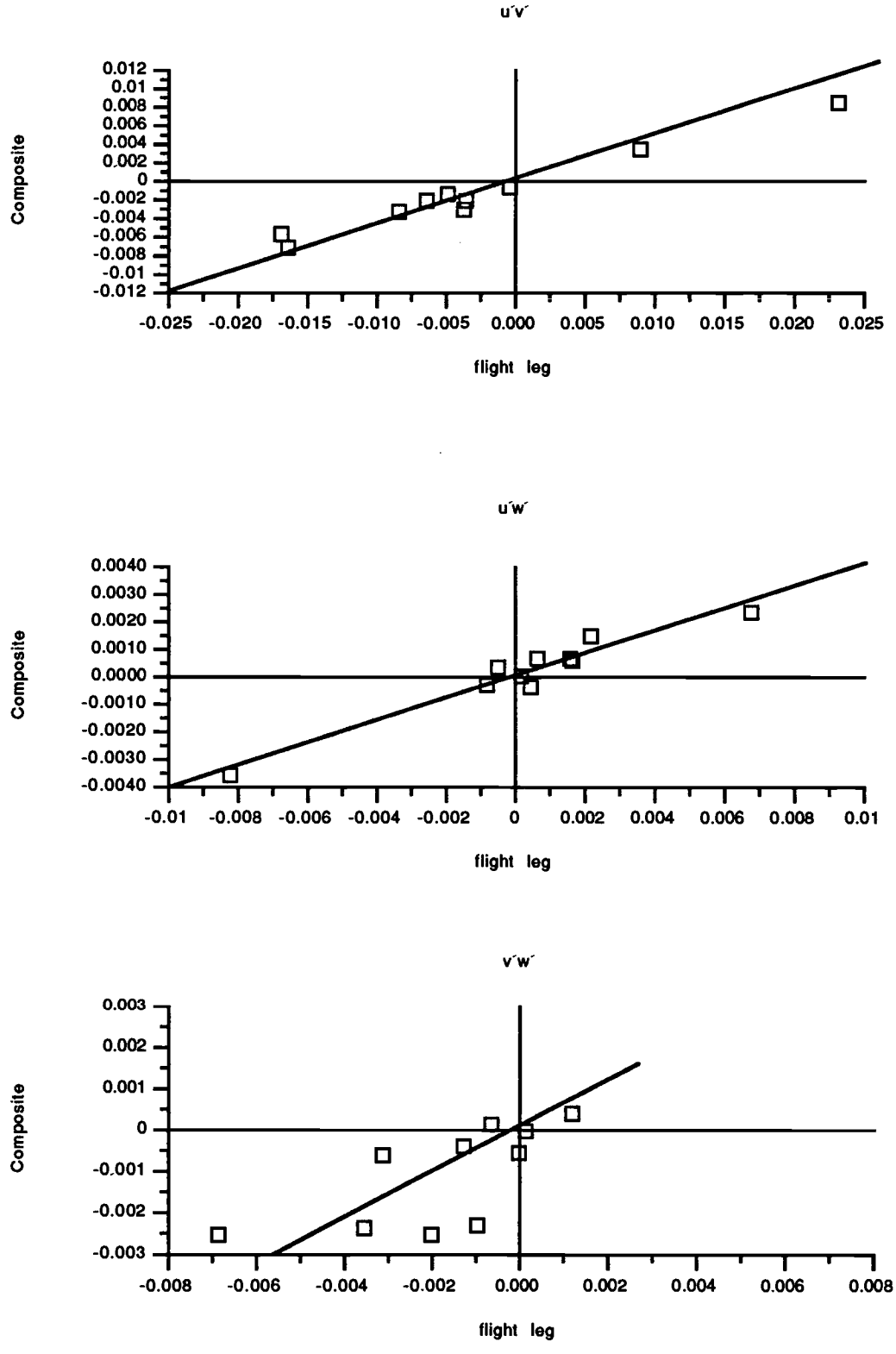

Figure 4.7/continued

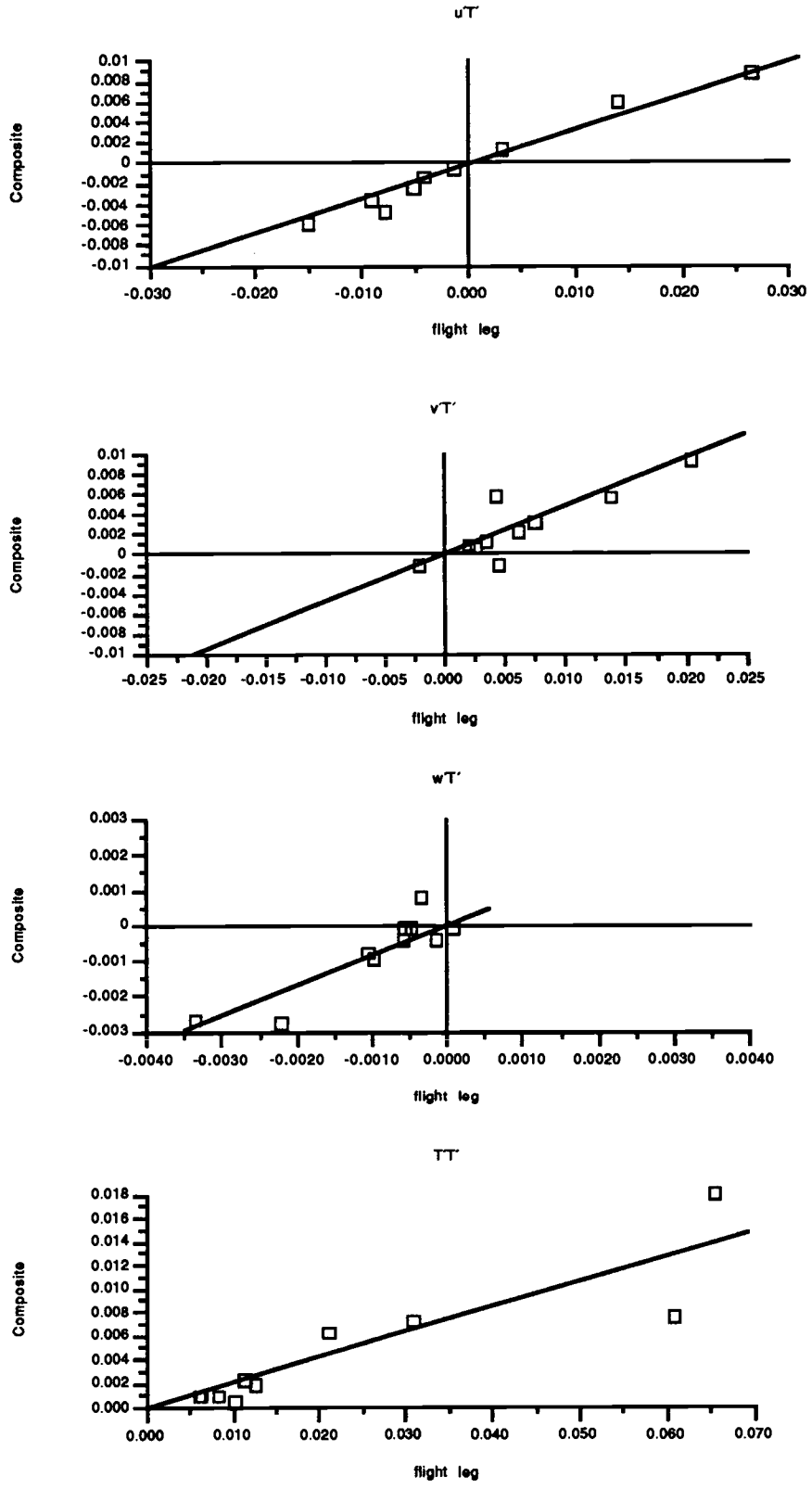

Figure 4.7/continued.

the important variability from one sample to the next. If indeed the structure being composited is typical of two-dimensional eddies, then the bulk of the eddy would merely redistribute properties of the fluid; mixing would take place at the edges of the eddies. The analysis of Chapter V will support this interpretation.

The composites of Figs. 4.3a-h can be viewed as comparatively cool northwesterly flow with an intrusion warm southeasterly boundary-layer flow. At the boundaries of the two flows, there is often strong horizontal shear. These transition zones are also characterized by varying degrees of asymmetry. Table 4.4 illustrates this apparent velocity jump for each leg by computing a horizontal velocity shear across the jump zones in a manner analogous to computation of the ξ^2 statistic to be described later in Chapter V. The shear variance is calculated as

$$\xi_u^{\,2}(j) = \left[u(j+1) - u(j-1)\right]^2 , \qquad (14)$$

where the sample endpoint values (j=1 and j=20) will have a value of zero. The horizontal shear is concentrated in these transition zones (the calculation for each leg is not shown here).

This observation of a sharp transition is not usually noted in a conceptual model of a simple gravity wave, nor is it emphasized as a property of two dimensional vortical modes or turbulence in strongly stratified flow. Further complicating the analysis is the observation that the jump zones do not always appear to be symmetric (see Table 4.4). Shear is often concentrated in the convergent[4] zone, for example, and negligible in the divergent zone. For example legs 2, 3, and 5 appear to be quite symmetric between the northern and southern transition zones. Other legs, such as 1, 6, and 10, show a great deal of asymmetry.

Another feature of interest which is illustrated in Table 4.4 is horizontal anisotropy. In particular, legs 1, 5, 6, and 11 of 5 May and leg 4 from 6 May are characterized by the

[4]In speaking of divergence and convergence here, it of course refers only to the one resolvable flow direction.

Table 4.4

Horizontal Velocity Shear ($m^2 \cdot s^{-2}$) Across Transition Zones for the Leg Composites

		u-component		v-component		total horizontal shear	
Flight	Leg	N	S	N	S	N	S
3	1	0.006	0.010	0.002	0.008	0.008	0.018
3	2	0.001	0.001	0.001	0.001	0.002	0.002
3	3	0.001	0.001	0.001	0.002	0.002	0.003
3	4	0.009	0.005	0.002	0.010	0.011	0.015
3	5	0.005	0.004	0.003	0.003	0.008	0.007
3	6	0.014	0.008	0.005	0.001	0.019	0.009
3	9	0.000	0.000	0.001	0.004	0.001	0.004
3	10	0.007	0.002	0.008	0.007	0.015	0.009
3	11	0.028	0.052	0.023	0.001	0.051	0.053
5	4	0.010	0.008	0.001	0.003	0.011	0.011

horizontal shear variance ($\xi_h^2 = \xi_u^2 + \xi_v^2$) being concentrated in the u-component. There is little indication of compensating dominance of v over u in the other composites except for leg 4 of 3 May. If horizontal or fully three-dimensional eddies are indeed present in this boundary layer as we surmise, they are being stretched out in the direction of the mean shear, about 40-45° off the direction of the flight path. We therefore would not expect to find such a pronounced anisotropy as described above for the turbulent eddies. No explanation for this observation will be attempted here.

This chapter has illustrated the complexity of very stable nocturnal boundary flow by conditionally sampling over 200 distinct observations of a structure or group of structures characterized by horizontal motion in the first principal component. A few of the leg composites have features quite similar to simple gravity waves, while most indicate very nonlinear behavior.

Analysis of individual samples in the next chapter will suggest the presence of vortical modes and shear-induced overturning. This analysis will suggest new directions for parameterization of turbulence in the SBL; these will be discussed in Chapter VI.

Chapter V

Analysis of Selected Samples

1. Selection of samples

The samples from the ten flight legs of interest were inspected individually for the presence of zones of sharp transition in the horizontal flow field. This analysis is motivated by the analysis of the composited flow features of Chapter IV. There we saw composites formed which contained interesting dynamic features but which were characterized by weak fluxes and variances. Although it is difficult to assign the coherent structures identified in that analysis to a particular type of flow régime (i.e., linear gravity wave, transverse eddy, two-dimensional vortical mode), it is clear that these eddies[5] are robust features of the flow.

Several features about the compositing procedure were noted, however, which are important to reconsider here. First, it was shown that the partition of the total variance of the horizontal velocity components could be significantly changed by removing one or two samples from the family of samples that originally formed the composite. Typically, the composite explained about 25% of the total variance for the horizontal velocity components and temperature; the influence of stratification greatly limited the impact of vertical motion on the analysis. Because the individual samples are quite noisy, much detail is lost in the compositing procedure. There is much information in the samples which is not being captured by the compositing procedure.

This would be especially apparent at the locations of the cross-over zones, where the u and v components of velocity reverse their sign (recall that they are 180° out of phase). The samples are fixed by interpolation to a one-dimensional grid of twenty points,

[5]I will use the term eddy here for convenience, with the understanding that the feature observed could be a result of nonlinear interaction of waves, vortical modes, and eddies.

with the anchor points being the maxima and minima of the leading principal component. Because this principal component is dominated by u and v (and T), it will vanish as u and v approach zero; the samples are not at all symmetric, however. Although u and v are negatively correlated, individual samples are seen to occur with u and v not changing sign at the same point in the flow. The composite would smooth out any form of asymmetry which did not have a particular preference for one variable leading another through the transition zone. Because u, v, and T all vanish approaching the cross-over zone, the fluxes will not be maximized there.

Active, fully-developed turbulence and large fluxes are not expected for a strongly stratified flow; the composites verify this but they may be bringing out only smoothed structures of the large eddies. As pointed out in previous studies of stratifed turbulence (e.g., Chen and Blackwelder, 1978; Schols, 1984) gradients and fluxes are often concentrated at the edges of these large eddies. The eddies themselves have a very small aspect ratio (ratio of depth scale to length scale), and mainly mix fluid horizontally. It is believed careful analysis of the individual samples would lead to a better understanding of the small-scale dynamics, especially at the cross-over zones, which are believed to be the edges of the coherent structures. Indeed, velocity gradients are quite large.

We will now see that there is evidence of strong mixing at the cross-over zones, which could be termed jump zones and may actually be analogous to turbulent microfront zones (e.g., Kaimal and Businger, 1970).

The 216 samples involved in the definitions of the composites for the flight legs suggested a great variety of flow possibilites. Recall that one leg in particular had a composite indicative of a simple linear gravity wave (leg 3), while for many others the composited vertical motion was too weak as to determine its structure. Some samples with apparent jump zones at the cross-over point are shown in fig. 5.1; these jump zones are present in many samples and are identified subjectively from the plots of the horizontal velocity vectors. A total of 339 jump zones were obtained from the 216 samples.

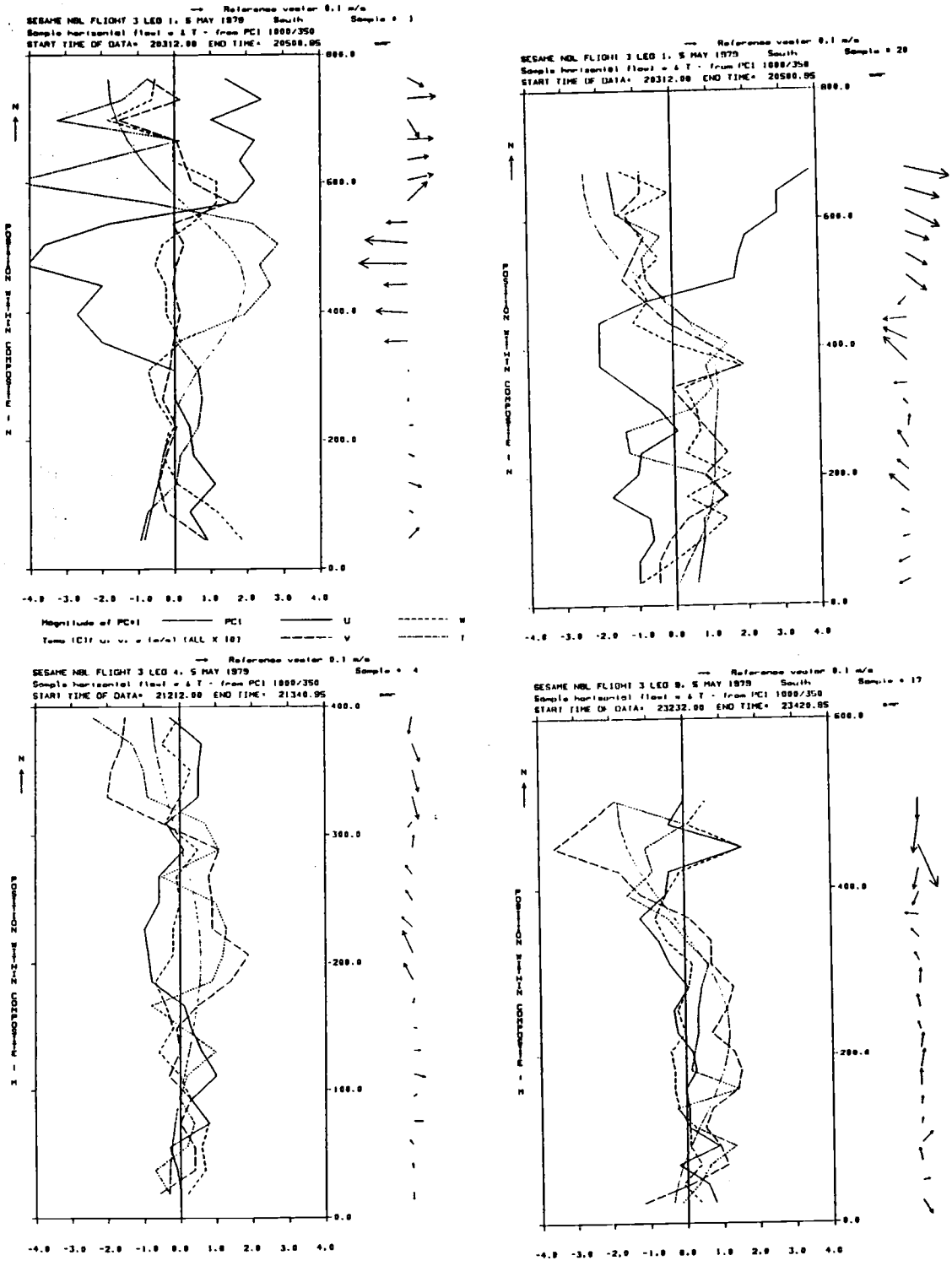

Figure 5.1. Examples of individual samples which illustrate pronounced horizontal shear which is concentrated at the cross-over zones. See text for explanation.

As was pointed out in Chapter III, the structure function has long been utilized in the analysis of turbulence data and should provide a quantitative measure of the importance and character of these narrow zones of transition. The horizontal shear of horizontal velocity variance, or more simply, *shear variance* is defined as

$$\xi^2 \equiv \left[\left(u(y+\Delta y) - u(y)\right)^2 + \left(v(y+\Delta y) - v(y)\right)^2\right], \qquad (1)$$

where the separation distance is Δy; where y refers to position within a sample. For the analysis presented here, $\Delta y = 42$ m. The purpose of this analysis is to determine the frequency with which these jump zones appear in the samples, and to determine the structure of the zones.

Towards this end, a simple ratio of the percent of shear variance occurring in the jump zone to the percent of the sample occupied by the jump zone will be used to demonstrate significance. The validity of this statistic was tested by computing the shear variance for one jump zone per sample, chosen on a random basis, without consideration of the actual shear. The results indicated that for flight 3 (205 random samples), the ratio was 1.14 (with a standard deviation, s = 1.2) and for flight 5 (32 samples) it was 0.82 (s = 0.47). A value close to unity is expected for randomly drawn samples.

Not all samples exhibited apparent jump zones. Many samples contained weak motion everywhere, while others were indicative of horizontal meandering or rotation with no apparent zones of convergence or divergence (fig. 5.2). We might expect two jump zones per sample if they are at the edges of the large eddies. We find in the individual samples, however, as many as five jump zones in one sample. Here we must be careful about sampling problems, of course, as there are only twenty points for each sample (see fig. 5.3).

The method used to carry out this analysis was to roughly define the jump zone boundaries for each subjectively-located jump zone, compute ξ^2 across each zone and for the entire sample, and then exactly define the end points of the jump zone by forcing their

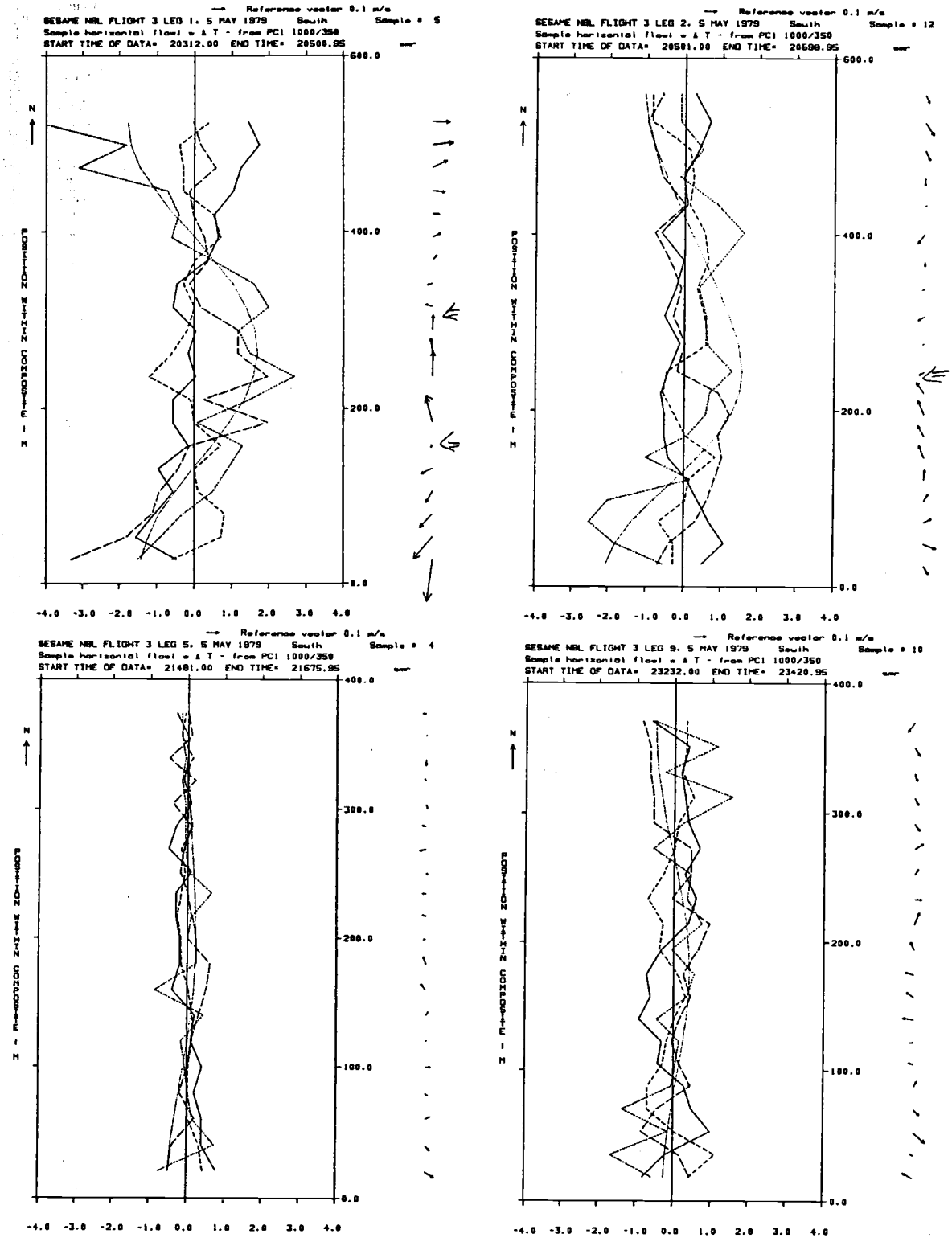

Figure 5.2 Examples of samples which do not illustrate large horizontal shear concentrated at the cross-over zones.

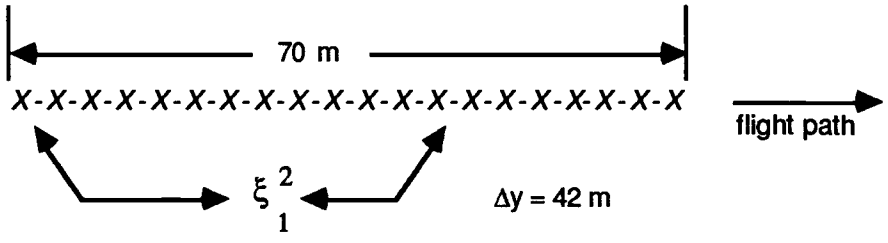

Figure 5.3. Schematic of the computation of ξ^2 in a jump zone. The figure indicates a jump zone which is 20 points wide. With a lag of 42 m, there will only be 8 values of ξ^2 computed. Fluxes are computed at each of the 20 data points, indicated by *X*.

end points to have a value of ξ^2 at least twice the average value for the entire sample. In addition, there must be at least four consecutive points with ξ^2 greater than twice the sample average of ξ^2 for the zone to be included for further study. This procedure is important because for some zones, the jump zone may be quite narrow so that the value of Δy may be too large to provide a representative value for ξ^2. Some narrow zones indeed yield larger ratios for Δy = 28 m, for example, but the overall results were not improved. There were also some places within a sample which contained large ξ^2 values, due to speed change only with no changed direction. Although these zones seem interesting, they were also not included in the analysis as they likely belong to a different type of flow regime.

The next section will concentrate on analysis of some particularly interesting dynamical features of the cross-over zones which exhibit strong horizontal shear. In addition to large values of the ξ^2 statistic, very large fluxes will be found at these shear zones, supporting the contention that strong mixing is occurring at the edges of organized coherent structures. In section 3 an attempt is made to elucidate more quantitative understanding of these jump zones through an analysis which includes compositing of the strongest jump zones.

2. Jump zones at coherent structure boundaries

There are 137 jump zones from legs 1 through 6 and also leg 9 from 5 May which will be analyzed in this section. There is a great deal of variability in the width and intensity of the jump zones, so no compositing will be attempted at this phase of the analysis.

Table 5.1 gives statistics about the sample and jump fluxes and variances for this period. Included in the table are all the kinematic fluxes and variances possible, as well as the horizontal and vertical eddy kinetic energy, defined here by

$$e_h \equiv \frac{1}{2}(\overline{u'^2} + \overline{v'^2}) \ , \tag{2}$$

and

$$e_v \equiv \frac{1}{2}\overline{w'^2}, \tag{3}$$

respectively. In the table, sample values are indicated in plain type, while jump values are indicated by italic print.

There are several interesting aspects of the fluxes in the samples, compared to those in the jump zones. We find the sample fluxes have a great deal of variability. This is evident upon examining the standard deviation, maxima, and minima of the various fluxes and variances in Table 5.1. For example, the average kinematic heat flux for the samples under consideration was about –0.001 K m s^{-1}. This corresponds to a net downward heat flux[6] of only about 1.5 W m^{-2}. The range of values, however, extends from a maximum downward heat flux of -5.84×10^{-2} K m s^{-1} (–73 W m^{-2}) to a maximum upward heat flux of 1.03×10^{-2} K m s^{-1} (+15 W m^{-2}). The maximum values for most of the fluxes and variances are in fact at least an order of magnitude larger than the average values. The ratio of eddy vertical to horizontal kinetic energy is a measure of the degree of influence the

[6]To make the conversion of kinematic to energy units requires multiplication by the air density, $\rho \approx 1.25$ kg m^{-3} and the specific heat of air at constant pressure, c_p = 1004 J kg^{-1} K^{-1}.

Table 5.1

Flux and variance[7] statistics for samples and jump zones

STATISTIC	$\underline{u'v'}$	$\underline{u'w'}$	$\underline{v'w'}$	$\underline{u'u'}$	$\underline{v'v'}$	$\underline{w'w'}$	$\underline{u'T'}$	$\underline{v'T'}$	$\underline{w'T'}$	$\underline{T'T'}$	$\underline{e_h}$	$\underline{e_v}$
mean (10^{-3})	–7.57	2.08	–1.94	21.4	14.9	7.45	–6.22	5.60	–1.12	14.9	18.1	3.73
	–10.3	*1.22*	*–2.41*	*31.0*	*20.6*	*12.3*	*–8.46*	*8.32*	*–1.46*	*23.2*	*25.8*	*6.14*
std. dev. (10^{-3})	20.3	10.7	9.13	38.5	22.4	11.7	16.3	11.2	6.06	18.7	29.8	5.83
	27.0	*15.9*	*11.4*	*51.5*	*30.9*	*39.4*	*22.0*	*22.0*	*11.0*	*60.8*	*39.1*	*19.7*
maximum (10^{-1}).	0.176	1.03	0.093	2.88	1.34	0.790	0.264	0.805	0.103	1.44	2.11	0.395
	0.484	*1.39*	*0.420*	*3.61*	*2.62*	*4.18*	*0.328*	*1.73*	*1.04*	*7.19*	*2.74*	*2.09*
minimum (10^{-2})	–14.5	–1.48	–8.19	0.054	0.075	0.065	–12.4	–1.81	–5.84	0.158	0.084	0.032
	–18.2	*–9.36*	*–7.50*	*0.022*	*0.033*	*0.021*	*–14.5*	*–7.32*	*–5.96*	*0.003*	*0.082*	*0.011*

[7]In appropriate SI (Système Internationale) units; table values should be multiplied by scale factors indicated for each statistic.

stratification plays on suppressing turbulence. The average ratio is 0.11 for the samples and 0.18 for the jump zones, indicating the importance of vertical motion in the jump zones.

In general, there ought to be some correlation between vertical heat flux and the vertical component of TKE in a turbulent patch of fluid. For the samples, this is generally the case, as shown in fig. 5.4a. Here there is a tendency for two diagonals along which the sample points are clustering, indicating the presence of turbulence energy which is transporting heat downward for most events, but upward against the gradient for a significant number of other samples. This relationship is less clear for the jump zones, however (fig. 5.4b). Here, stronger turbulence levels would ultimately reduce the temperature gradient locally, providing a mechanism which reduces the vertical heat flux; it is possible that we are observing some of this second-phase of turbulence in some jump zones.

A statistic representing the ratio of the percentage of variance explained in the jump zone to the portion of the record occupied by the jump zone can be defined as

$$\wp \equiv \frac{\xi^2}{t_\delta}, \tag{4}$$

where ξ^2 is as defined in (1) and t_δ represents the time spent in the jump zone; its units are $m^2\ s^{-3}$. For all jump zones, the resulting value of $\wp$ is 3.44, much higher than unity, which would be expected for randomly-drawn samples. Because of the way samples were drawn here, we would probably expect $\wp$ to be at least 2.

The *structure ratio* for variable φ will be defined here as

$$\Im_\varphi \equiv \frac{D_\varphi^{jump}}{D_\varphi^{sample}} \times 100\%, \tag{5}$$

where

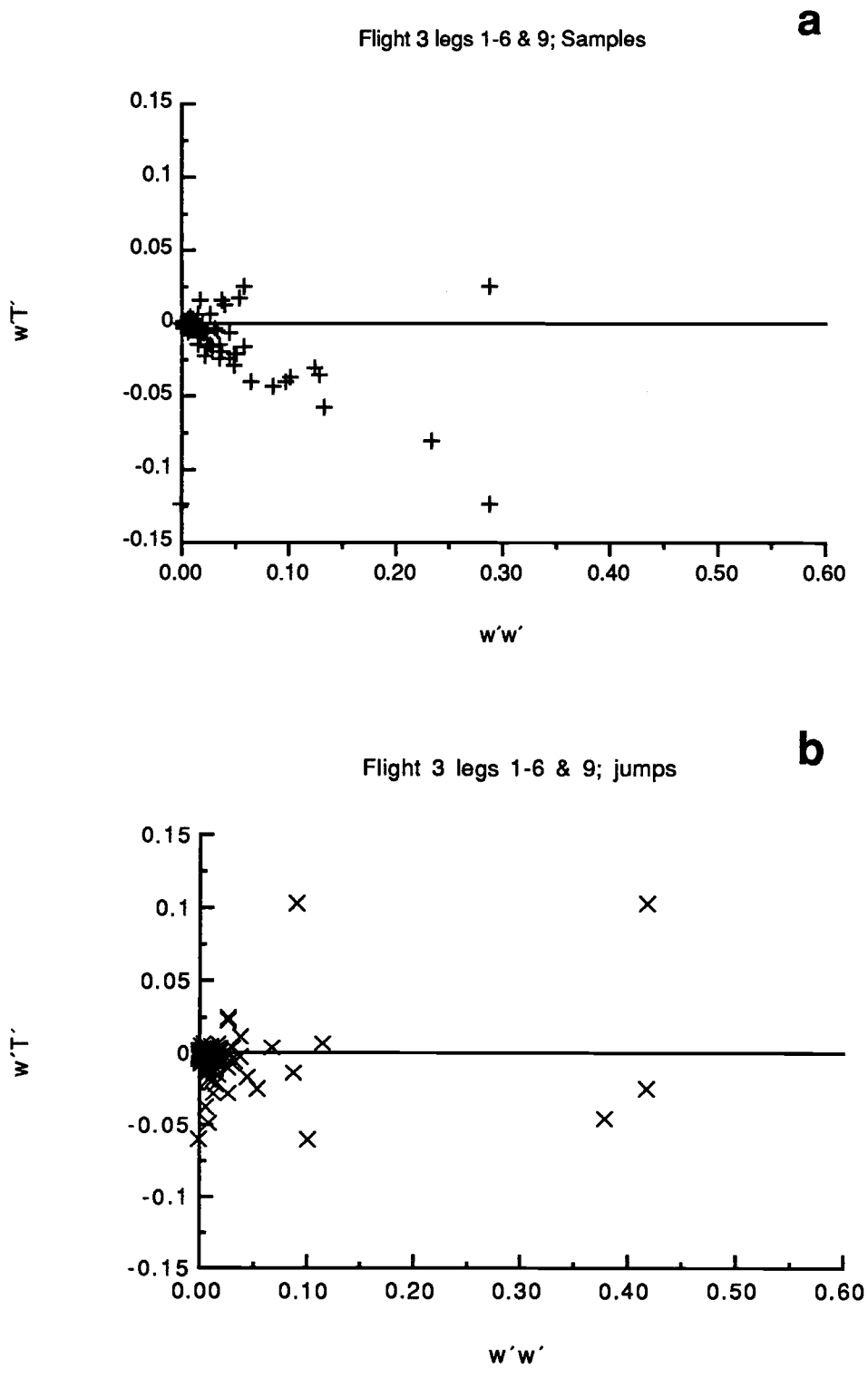

Figure 5.4. Average vertical velocity component variance ($m^2 s^{-2}$) and kinematic heat fluxes ($m K s^{-1}$) for (a) samples and (b) jump zones.

$$D_{\varphi}(\Delta y) \equiv \overline{\left(\varphi\,(y+\Delta y) - \varphi\,(y)\right)^{2}}\ , \qquad (6)$$

where the overbar is an average over the jump zone for D_{φ}^{jump} and a sample average for D_{φ}^{sample}. We compute values of $\Im$ for each variable for each sample.

The horizontal anisotropy of the structure ratio for samples' jump zones is illustrated in figure 5.5a. Structure function values are as much as an order of magnitude larger for the jumps than they are for the entire samples. Virtually the entire space between $\Im_u$ and $\Im_v$ is spanned, indicating how the jump zones are not dominated by gradients of only one horizontal velocity component, although the average ratio of $\Im_u$:$\Im_v$ for all of the jumps exceeds 2, indicating some preference for u. This may be related to an unintended bias in the subjective way jump zones were first identified.

The influence of stratification is much less for the stronger turbulence in the jump zone (fig. 5.5b) As would be expected, a fairly high aspect ratio is noted within the jump zones; the average ratio of $\Im_w$:$\Im_h$ is about 0.5. Another feature of the analysis is the apparent lack of importance of temperature, compared to vertical motion (fig. 5.5c, fig. 5.5d). This observation that temperature does not seem to have strong gradients runs counter to what might be expected for microfronts, which are characterized by sharp horizontal gradients of temperature and velocity on very small scales. Patches of oceanic finestructure for example, variously referred to as fossil turbulence and decaying turbulence as discussed earlier, are characterized by large temperature fluctuations and weaker velocity fluctuations. This is not seen here, but then by selecting samples based on horizontal shear, the importance of temperature could be reduced.

The jumps which are exhibiting the largest fluxes would also be expected to have the largest turbulent intensities. In addition, we would expect any three-dimensional anisotropy to decrease as the TKE increases. This is illustrated in figures 5.6, which are plots of e_h against e_v for the samples and jumps. While the TKE for the samples is completely dominated by e_h (fig. 5.6a), there is a tendency for increased values of e_v for

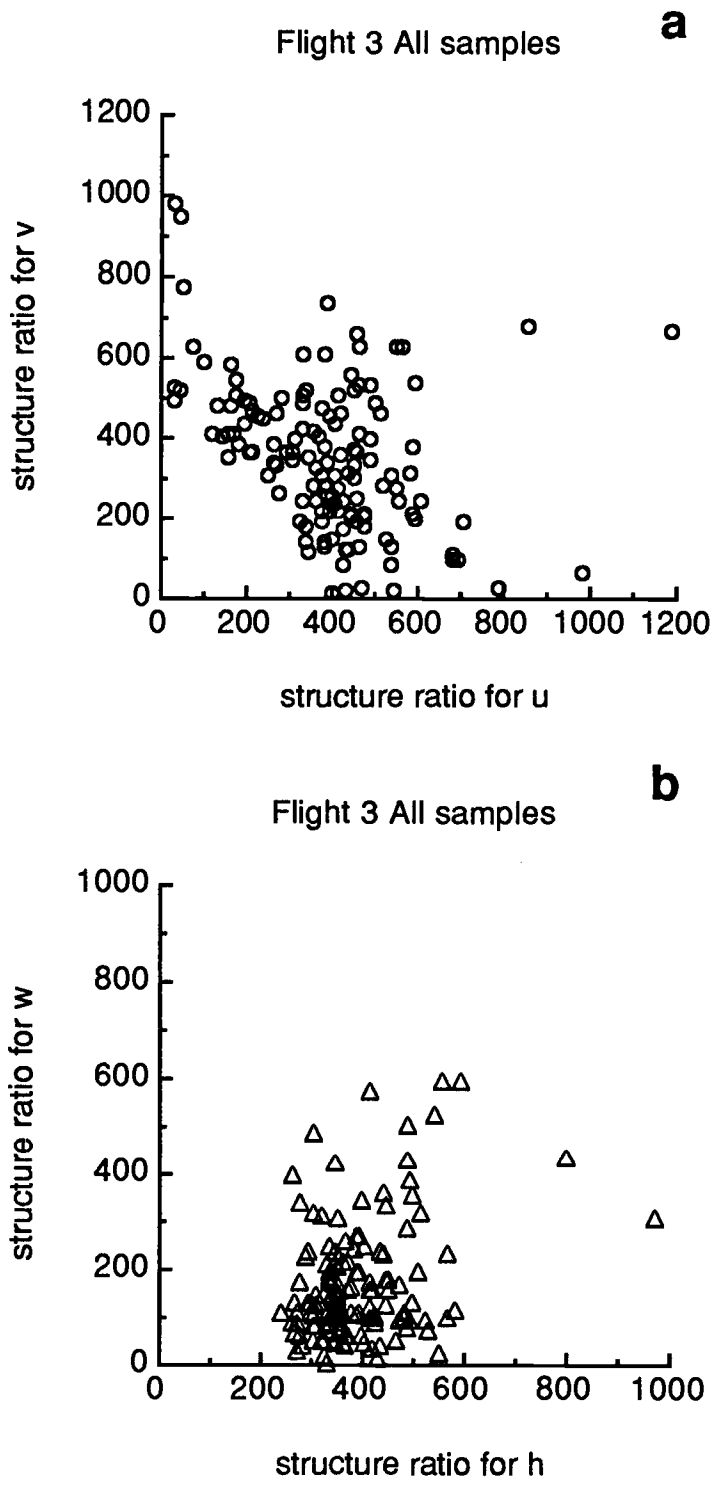

Figure 5.5. Scatter plots of structure ratios for the samples with jump zones. (a) $\mathfrak{I}_u$ vs. $\mathfrak{I}_v$; (b) $\mathfrak{I}_h$ vs. $\mathfrak{I}_w$; (c) $\mathfrak{I}_T$ vs. $\mathfrak{I}_w$; (d) $\mathfrak{I}_T$ vs. $\mathfrak{I}_h$.

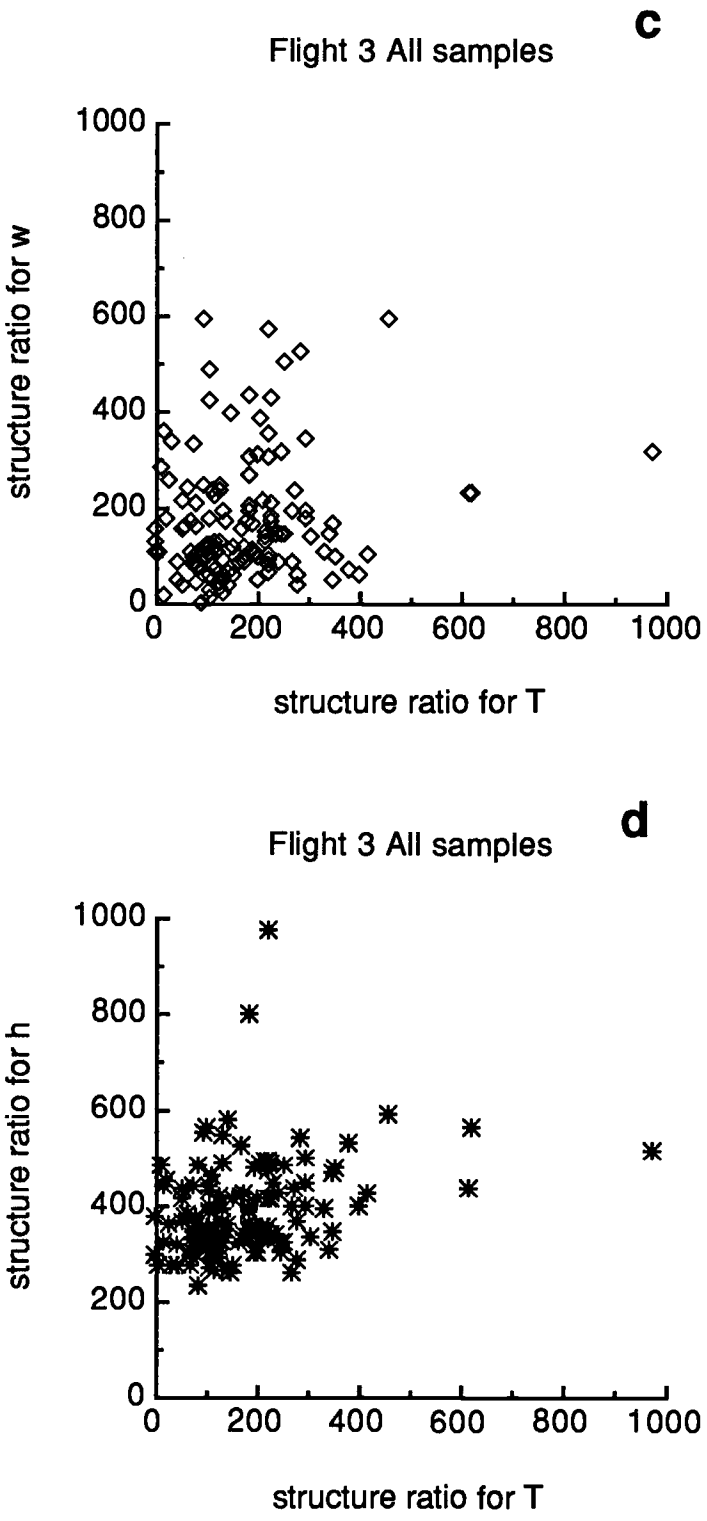

Figure 5.5/continued.

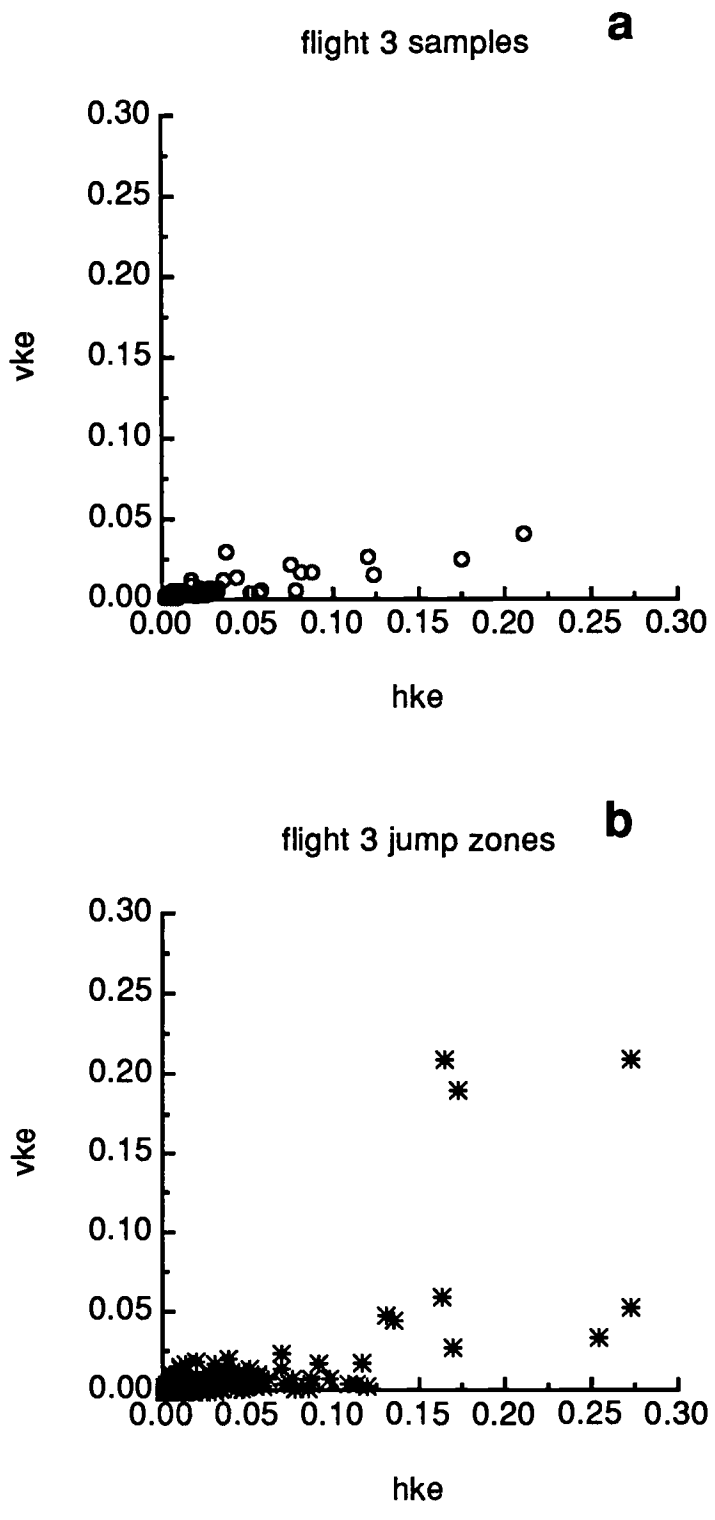

Figure 5.6. Horizontal (hke) and vertical (vke) eddy kinetic energy ($m^2\ s^{-2}$) for the (a) samples and (b) jumps.

the strongest few jumps (fig. 5.6b).

Up to this point, the analysis has verified the presence of strong turbulent transport regions at the cross-over points of the samples and composites examined in Chapter IV. In the next section, an analysis of the most intense jump zones will be carried out.

3. Analysis of strong jump zones

Here we will concentrate on the analysis of only those jump zones which exhibit the strongest gradients, identified by the horizontal structure ratio, $\Im_h$. A frequency distribution of $\Im_h$ (not shown) revealed that the among the 137 jump zones studied in section 2, about 1/4 of them had horizontal structure ratios well above 450%, the value at which the clustering appeared to end. As a selection criteria for the jumps to be analyzed here, "super-samples" were selected and defined to be those samples with jump zones having $\Im_h > 475\%$.

A subsample of 35 zones met this criteria. The structure ratios (fig. 5.7) exhibit much less clustering and the average structure ratios for the horizontal velocity components, $\Im_u$:$\Im_v$, increases by a factor of two, while the aspect ratio decreases slightly. This implies that the horizontal shear is primarily due to the u component, suggesting strong divergence and convergence.

Although vertical motion structure seems to be weaker in the strong zones, temperature seems to be more important, as the structure ratios for temperature, $\Im_w$:$\Im_T$ and $\Im_h$:$\Im_T$, decrease for these samples. As expected, $\wp$ increases here to a value of 5.5. To further analyze the importance of these jump zones and to avoid the complexities and sampling problems associated with the analysis of individual samples separately, the super samples' jump zones were composited. Twenty points were taken from each side of the center of the jump zone, corresponding to a width of 140 m. Because of the large variability of horizontal wind across the jump zone, the wind components were rotated so that the u-component was defined to lie along the shear direction for each individual jump. In choosing the shear direction, we are assuming that the shear is playing the main role in organizing the orientation of the coherent structures. The composite was carried out separately for convergent and divergent zones.

The convergent super jump zone is characterized by large gradients of temperature

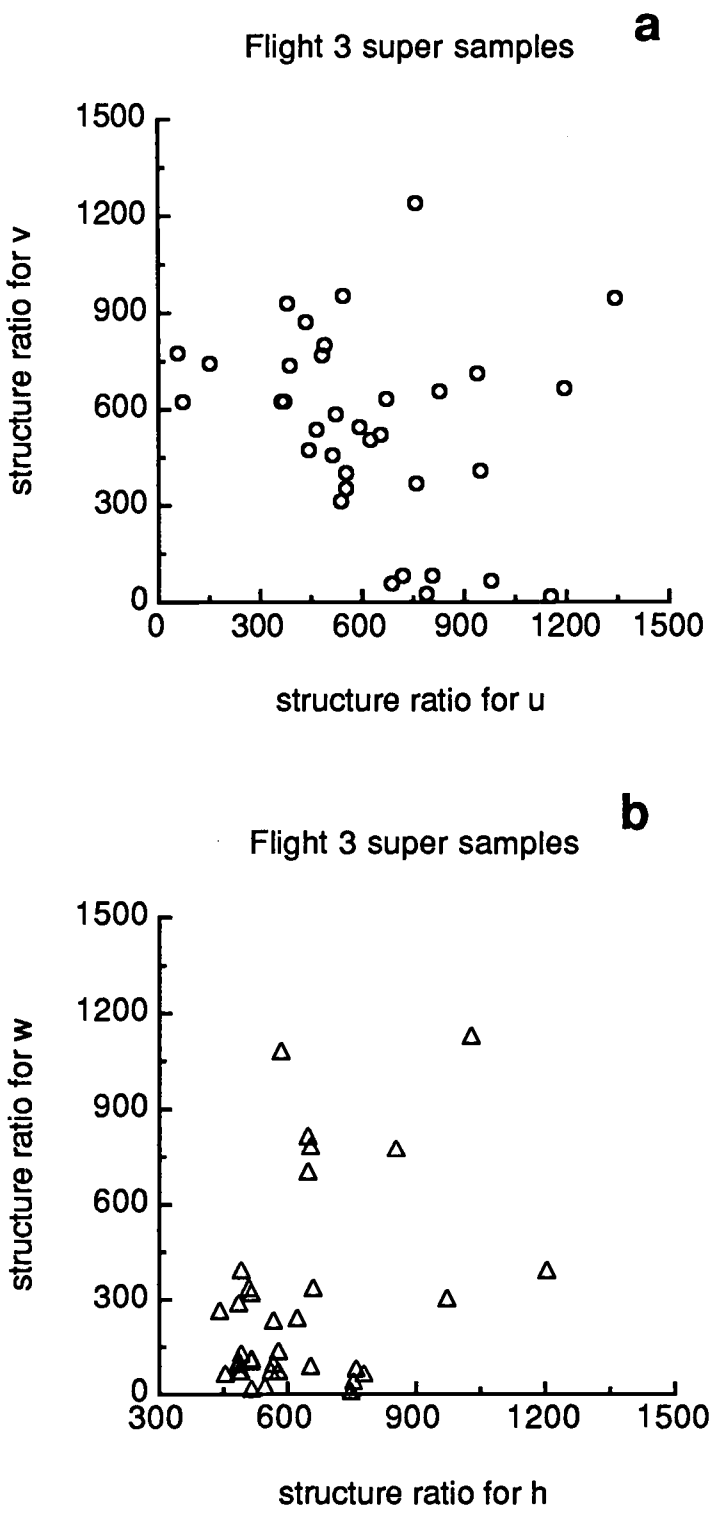

Figure 5.7. As in fig. 5.5 but for jump zones only.

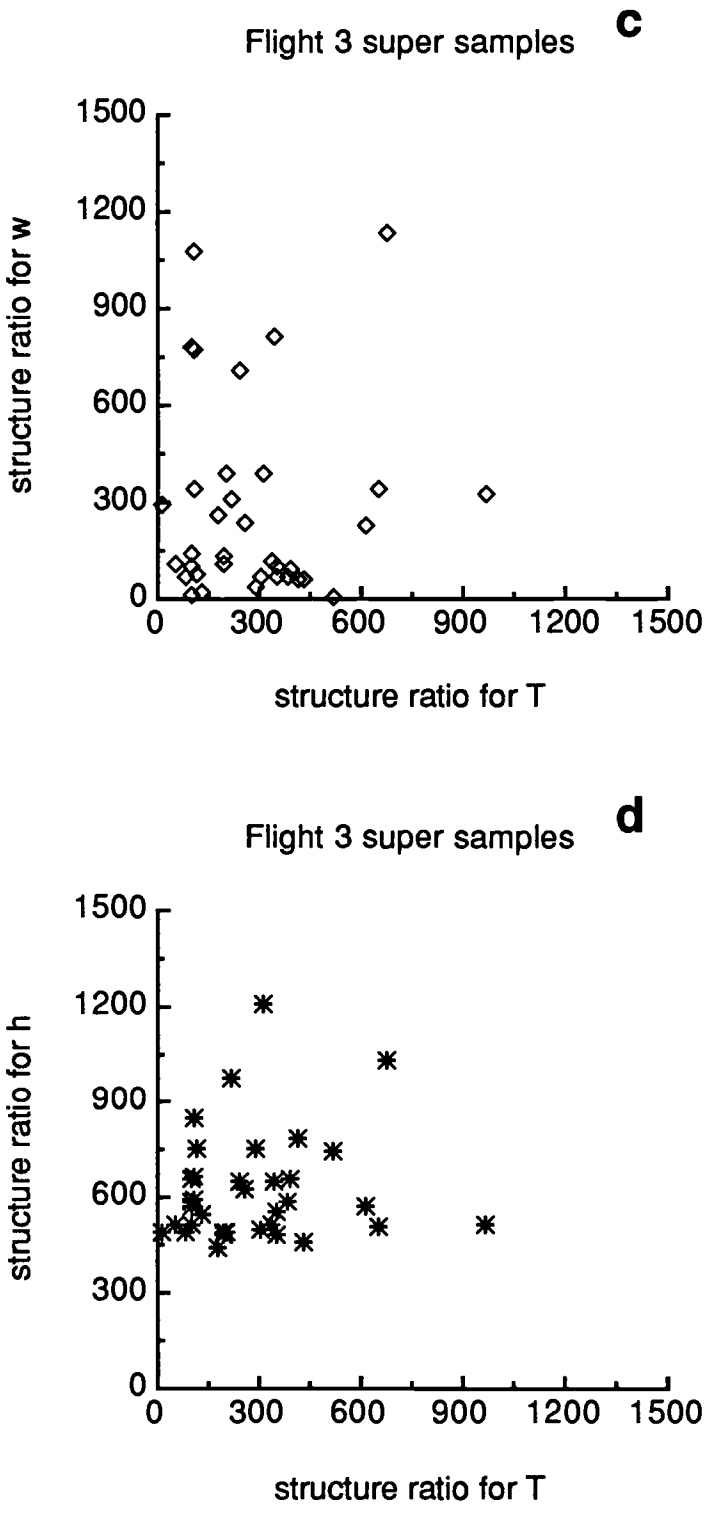

Figure 5.7/continued.

(fig. 5.8a), and weak rising motion, as opposed to weak downward motion for the entire collection of jump zones. The composite for divergent samples also illustrates large temperature gradients (fig. 5.8b), substantial horizontal shear across the jump zone, and significant rising motion. As a result of significant vertical motion, the divergent jump zones are regions of concentrated vertical heat flux and TKE (fig. 5.9). The ratio of e_v to e_h for these jump zones approaches 0.8, indicating weaker direct influence of the stratification. In general, stratification effects become less at smaller scales.

Interpretation of the above observations is made difficult by the one-dimensional nature of the direct observations, but based on previous studies of stratified turbulence, hypotheses regarding the nature of the circulations can be advanced. Focussing at first on the composite divergent jump zone structure shown in Fig. 5.8b, we note that vertical motion has a peak centered about the jump zone. The combination of rising motion at the center of the jump zone and apparent divergence supports the idea that the observations are of shear-driven overturning (fig. 5.10). The predominantly directional shear on 5 May and speed shear of 6 May would create transverse eddies with respect to the shear. With the x-axis chosen here as the shear direction, the vorticity component would be in the direction of the y axis,

$$\eta \equiv \frac{\partial u}{\partial z} - \frac{\partial w}{\partial x} \qquad (6)$$

In the vicinity of the observed divergent zone, we note that vertical shear of the horizontal component is present ($\partial u/\partial z > 0$). Additionally, vertical motion is decreasing to the north ($\partial w/\partial x < 0$), as required by (6) for η to be positive. As the composited flow feature also has sharp features at the convergent zone, our schematic can be extended to this part of the flow, as well. Note that the convergent zone is characterized by a much weaker vertical motion pattern (fig. 5.8a), perhaps indicating the degree to which the stratification is suppressing the expected sinking branch of the transverse eddy.

We can appeal to the Kelvin-Helmholtz instability mechanism (e.g., Turner,

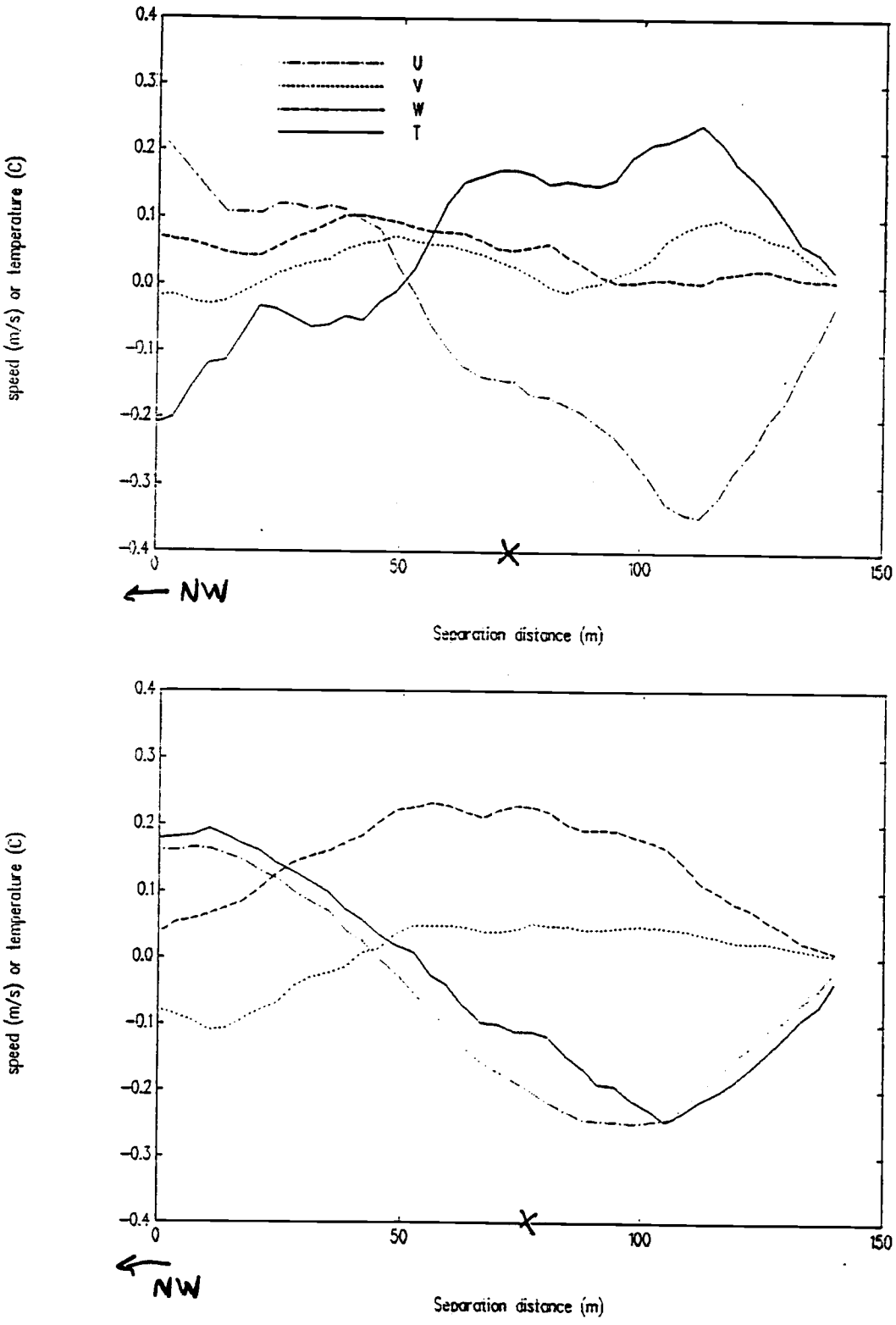

Figure 5.8. Composite of jump zones for the super samples (a) for those zones indicating convergence and (b) for those zones indicating divergence.

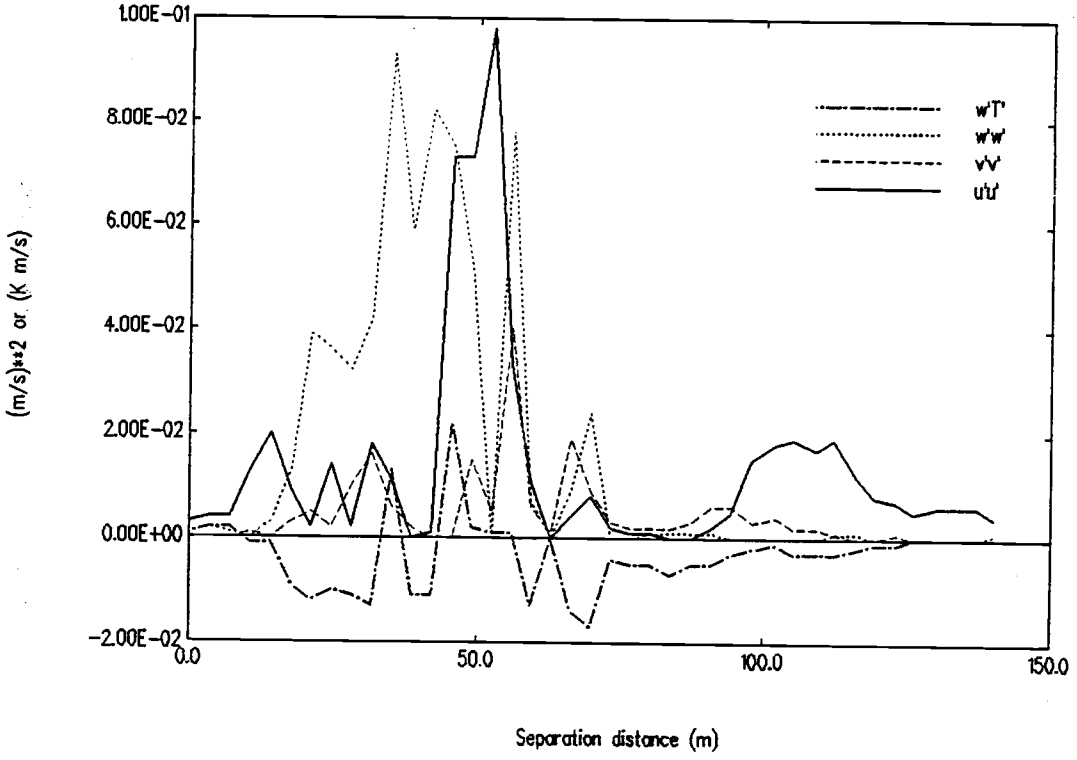

Figure 5.9. Fluxes and variances for those zones indicating divergence.

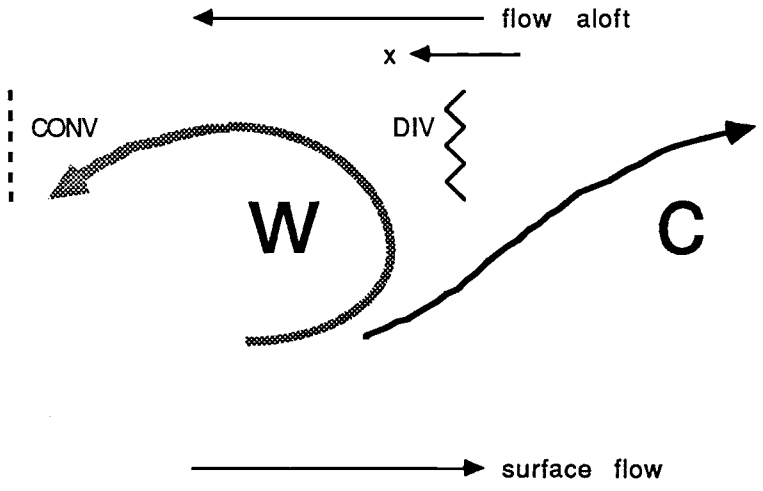

Figure 5.10. Sketch of composite flow pattern around super jump zones. Maximum temperature perturbation is indicated by a 'W' and the minimum by a 'C.' The jagged line indicates a horizontal shear zone and is coincident with the divergent zone. A microfront is indicated by the dashed line and occurs with horizontal convergence. The sign of the temperature gradient is also indicated. The true orientation of the x-axis here is about 320°, as the average direction of the flow aloft is about 140°.

1979), which is often applied when there is a marked density (potential temperature) jump at an interface. The situation here is more closely resembles continuous stratification, with buoyancy decreasing rapidly with height from the surface. At the flight level of the aircraft, there is a directional shear zone, but the presence of intermittent turbulence there mixes the fluid locally. This mixing results in a nearly-neutral sublayer in the boundary layer, as seen in fig. 3.2. The presence of mixed sublayers are common in the ocean (Woods *et al.*, 1969) and atmosphere (Li *et al.*, 1983). Turner (1979) summarizes many studies which predict that the most unstable wave which will develop on the interface will have a wavelength $O(10h)$, where h is the thickness of the turbulent layer. For our case, h is about 15 m (Mahrt, 1985), which would result in a horizontal dimension of about 150 m.

Turbulence under stratification is a very complicated process; for example, Turner (1979, p. 117) cites seven mechanisms by which mixing can take place in stratified fluids. For these processes, the turbulence is either created by a solid boundary or at an interfacial zone with sharp density and velocity gradients. Internal waves in the fluid become locally unstable for a variety of reasons, with small-scale turbulence as the result. The more complicated process of instability (creation of turbulence) under continuous stratification is also examined separately. The mixing we observe in this study is most likely related to this process, as the turbulence we observe is quite local, with no apparent connection to the surface. While there is a large change of velocity in the lowest 60 m or so, the largest vertical gradient of potential temperature is near the surface for the SBL under present study. Under such conditions, where the local Brunt-Väisälä frequency decreases with height, internal waves may become trapped beneath layers of very small N.

We must take care here not to place all our emphasis on waves, however. The vortical mode is equally-likely (from an energetic standpoint), and very little is known about its nature in stable flows. We cannot unequivocally categorize the present observations as being representative of one type of motion. The nature of the observations

and nonlinearity of the flow preclude such a division. The schematic (fig. 5.10) is an attempt to describe the nature of the flow about strong jump zones, which is a result of a variety of mechanisms, but which is clearly three-dimensional. Much more work needs to be done in understanding microscale geophysical flows under stable stratification, with modelling, nonlinear analysis, and further observational work all likely to play important roles.

4. Summary of diagnostic studies and implications for modelling

The analysis discussed in the first part of this thesis embodies efforts to describe some dynamical features of the horizontal structure of turbulence in the very stable boundary layer. We have been able to demonstrate the existence of coherent structures in the SBL with primarily horizontal motion. However, substantial turbulent mixing occurs at the edges of these structures. The sharpness of the edges of some of the coherent structures reduces the usefulness of spectral techniques, so we rely more heavily on principal component analysis and structure functions, which can resolve sharp features.

We find that the strongest of these jump zones have flow characteristics similar to shear-induced overturning and transverse modes. A linear treatment of the role of temperature gradients in generation of horizontal vorticity is invoked as a plausible explanation of the composite flow about the super jump zones.

The very stable boundary layer is seen in this and other studies to contain significant turbulence at bulk Richardson numbers well above the critical values often used (from 0.25 to 1.0). Because many models of the SBL arrest turbulent mixing when the critical Richardson number (or some other dynamical instability criterion) is exceeded, these models cannot accurately parameterize vertical mixing in the very stable case, leading to overestimation of the surface cooling and underestimation of the boundary layer height.

In the next chapter, an effort is made to incorporate some of the present observational work, other observational studies, and recent theoretical developments into a simple parameterization scheme of the stable boundary layer in a global numerical weather prediction model. These new parameterization efforts will improve forecasting of the very stable boundary layer and its impact on large-scale structure of the atmosphere.

Chapter VI

Parameterization of the Stable Boundary Layer

1. Introduction

In this study, the planetary boundary layer (PBL) model of Troen and Mahrt (1986; hereafter referred to as TM86) is examined to determine its response to specific parameterization changes. This model is currently used in a global spectral model (Brenner *et al.*, 1984). The modifications discussed below are motivated by examination of other model formulations as well as analysis of aircraft and tower data in the stable boundary layer (SBL). Any model improvements must be weighed against potential increases of computational costs and model complexity.

The parameterization of the very stable boundary layer is an important problem. For example, consider the forecasting problems of minimum temperature and pollution concentrations. Under very stable conditions with clear skies and calm winds at night, the minimum surface temperature can be determined to a large degree on the solution of the surface energy balance (Pan and Mahrt, 1987). With inadequate sensible heat transfer, the amount of nocturnal cooling of the surface can easily be overpredicted. The predicted formation of dew also plays an important role (Oke, 1978).

The more statically stable the lower atmosphere, the greater the potential for serious air pollution episodes. The meteorological conditions which favor serious air stagnations are well-known to be associated with synoptic scale high pressure, when large-scale subsidence acts as a cap to boundary layer growth. The presence of a capping temperature inversion on a statically stable PBL restricts vertical mixing of pollutants. In addition, horizontal advection of pollutants away from their source is not likely near the centers of high pressure systems, where winds are weak. The mechanism which is perhaps most important in this regard is the strength of the turbulence (parameterized through the eddy

diffusivity) which can diffuse the pollutants upward from the surface. With inadequate vertical mixing, the model would predict higher concentration values than might be expected.

The main changes studied here involve, firstly, the determination of the height of the PBL under stable conditions, where a critical Richardson number formulation is used. The second change involves application of a modified exchange coefficient for momentum, heat, and moisture, as discussed in Chapter IV and following Mahrt (1987). The final change, and perhaps the most significant one, involves the reformulation for the eddy diffusivity in the boundary layer for very stable conditions following Kondo *et al.*, (1978). The motivations for considering and ultimately implementing these changes will become apparent separately in each of the following sections.

These examinations involve running the one-dimensional version of the model of TM86, performing separate sensitivity tests of each of the new formulations. Finally, all three changes are included together. Initial conditions for this sensitivity experiment were specified for a 48 hour run, using latitude 20°N, longitude 10°E, 0800 GMT on 21 June. The soil and atmosphere are both taken to be dry, the modelled soil properties are those of sand, the atmospheric lapse rate is 6°C km^{-1} with an initial surface temperature of 20.7°C; the time step used in the model is 180 s and the vertical resolution is 20 m.

The suggested reformulations are described in detail in section 2. Section 3 presents the results of the sensitivity tests for the initial conditions listed above. In section 4, other tests of the 1-D model are discussed, including a simulation of conditions during the Wangara field experiment (Clarke *et al.*, 1971) and a winter snow cover situation over Manitoba using a new model package for surface snow cover. Finally, the results are summarized in section 5.

2. New Formulations

a. PBL height and the critical Richardson number

The Richardson number is viewed as the ratio of buoyancy destruction of turbulence to its production by shear, and in gradient form has a theoretical critical value of 0.25, according to many studies over the past fifty years (Panofsky and Dutton, 1984). Recently, however, the value of the critical Richardson number has again come into question. Miles (1987) (whose 1961 contribution had much to do with the instillation of the value $^1/_4$) gives an historical accounting of the Richardson number and its usage and finally suggests, based on recent advances in nonlinear hydrodynamic stability theory (e.g., Abarbanel *et al.*, 1986), a value of $Ri_c = 1$.

The Richardson number may take different forms, but in numerical models the layer Richardson number is the only type which can be used. It is defined as

$$Ri_L = \frac{g\ \Delta z\ \Delta\theta}{\theta_0 [\Delta U]^2}\ , \qquad (1)$$

with θ_o the mean potential temperature of the layer, $\Delta\theta$ the change in potential temperature across the model layer, Δz the thickness of the model layer, and ΔU the change in wind speed over the layer. If the bottom layer is the ground surface, ΔU becomes simply U, Δz becomes z, and Ri_B is called the bulk Richardson number. Because of the sensitivity of Ri to the depth over which gradients are measured, it is generally believed that the true critical Richardson number actually increases as the depth increases (Lyons *et al.*, 1964). In fact, turbulence is often observed, at least on an intermittent basis, for layer Richardson numbers much larger than 0.25. A critical value of 1.0 is often used in applications (Brutsaert, 1982), and this value will be used in the control experiment.

In the present model, the height of the boundary layer for the stable case is determined from

$$h = \frac{Ri_c \ \theta_0 \ U^2}{g \ \Delta\theta_v} , \qquad (2)$$

where h is the boundary layer height, U is the wind speed in the model layer, and $\Delta\theta_v$ is the virtual potential temperature change from the top of the layer to a point near the surface (see TM86), and Ri_c is the critical Richardson number. The determination of h is an iterative procedure, beginning at the surface. At each model level, the bulk Richardson number is calculated and compared to the critical Richardson number. When Ri_B exceeds Ri_c, the boundary layer height is found by a procedure which is illustrated graphically in Fig. 6.1

The proposed change to TM86 does not involve the format for determination of h but rather the value of the critical Richardson number. Because of the sensitivity of h to Ri_c, it is important that a critical value be chosen which simulates a realistic transition to suppressed turbulence (for $Ri > Ri_c$). TM86 chose a value of 0.5. It is clear from (2) that any change in Ri_c will force a direct response in the predicted value of h. Observations do support the notion that turbulence continues at layer Ri values well above 1 (e.g., Portman *et al.*, 1962; Webb, 1970; Kondo *et al.*, 1978; Kunkel and Walters, 1982; Louis *et al.*, 1983; Mahrt, 1987). In light of these observations and new theoretical developments, perhaps a value as large as 5 for a critical value of the *bulk* Richardson number may not seem unreasonable. Experiments will be carried out for several values of the critical Richardson number.

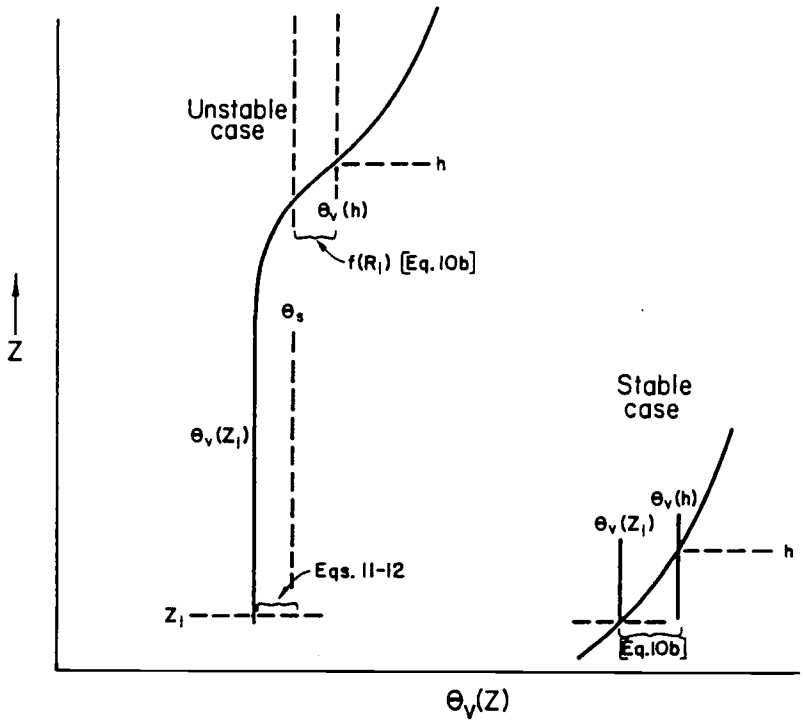

Figure 6.1. Determination of boundary layer height in the PBL model (Troen and Mahrt, 1986).

b. Surface exchange coefficients

As mentioned earlier, Mahrt (1987) has proposed that a modified exchange coefficient for heat be implemented in atmospheric PBL models. Such a change is motivated because present models underestimate the strength of heat transfer in the very stable case, due to typical subgrid-scale variations of surface conditions. Recently, the European Centre for Medium Range Weather Forecasts (ECMWF) modified the parameterization of surface processes in their operational model (Böttger, 1987), partly motivated in part by exaggerated nocturnal cooling under clear skies. Apparently PBL models often predict surface temperatures which are too cold at night due to erroneous elimination of downward heat flux in the strongly stratified surface inversion layer. Other corrections to compensate for the lack of sensible heat transport under statically stable conditions are sometimes used, or a stable layer may not be permitted to develop, in which case the exchange coefficient for the neutral case is used, ensuring continuation of sensible heat transport.

In TM86, the coefficients of Louis (1979) have been used for momentum, heat, and moisture. Sensitivity tests have been performed to compare this relationship with the one proposed by Mahrt for the stable case, namely

$$C_h = C_{ho}\, e^{-m\, Ri_B}, \qquad (3)$$

where C_h is the calculated heat exchange coefficient, C_{ho} is its value for neutral conditions as calculated in the Louis formulation, and m is an adjustable parameter thought to be about 1.

The heat exchange coefficient will be substantially larger for the Mahrt formulation, as can be seen in comparing fig. 6.2a to 6.2b. Also as m in (3) is decreased, the exchange coefficient decreases more slowly with increasing bulk Richardson number (fig. 6.2c). Results from experiments for a few values of the adjustable parameter m will be presented

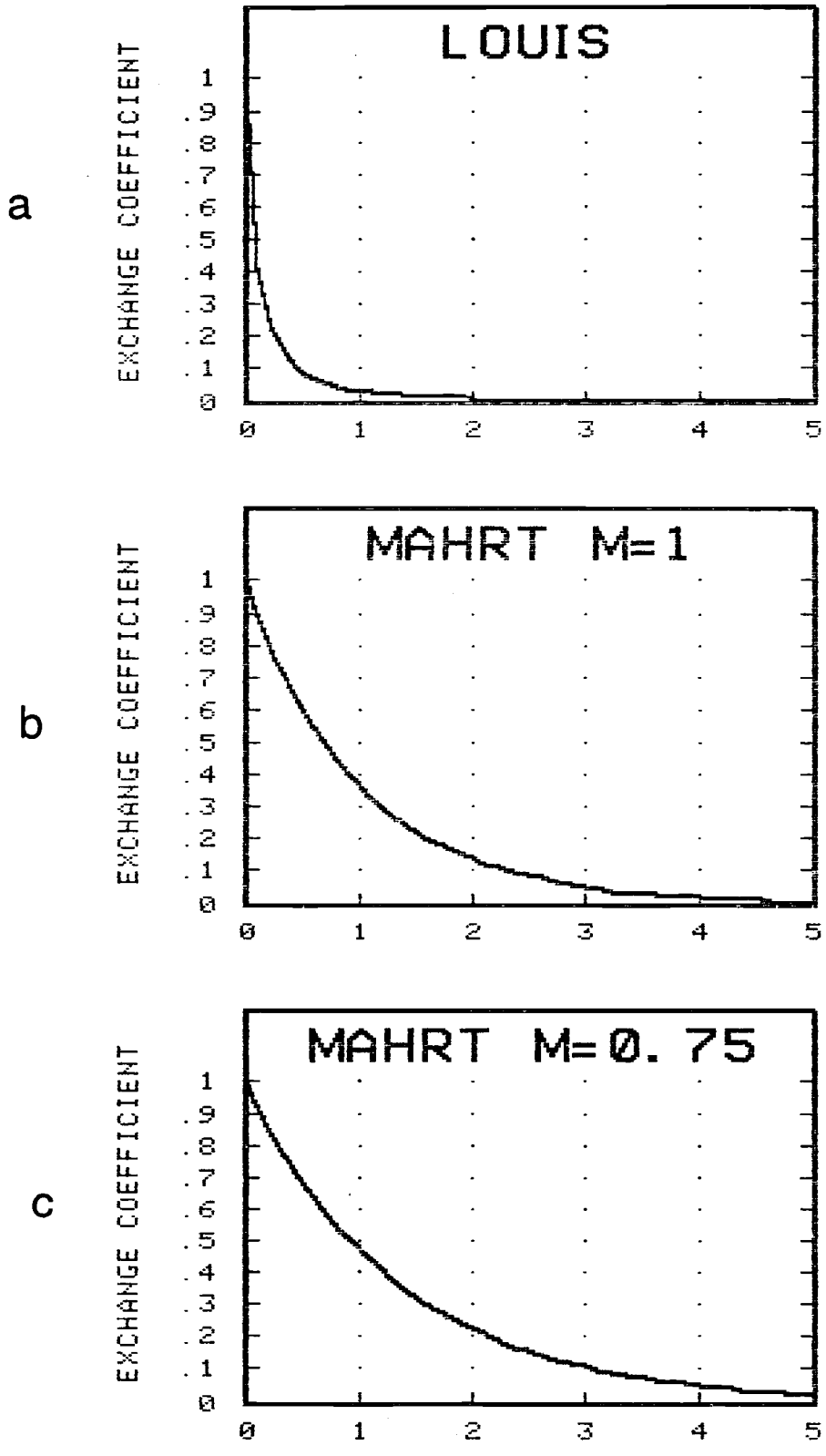

Figure 6.2. The effect of bulk Richardson number on the surface exchange coefficient. (a) $(1 + 4.7\ Ri_B)^2$, as in Louis (1979). (b) exp $\{-m\ Ri_B\}$, as in Mahrt (1987); m=1. (c) as in (b) but for m=0.75.

in section 3. The control run uses the Louis formulation for C_h.

c. Eddy diffusivity

Many simple models of the planetary boundary layer parameterize turbulence transport in terms of eddy diffusivities for momentum, K_m, and heat, K_h. Sommeria (1987) recently reviewed simple and complex parameterizations. Simple treatments suffer in the stable case because the turbulence in the so-called outer layer are governed by surface fluxes. Recent work in the stable case supports the notion of local scaling (Nieuwstadt, 1984) and applying a layer-by-layer approach (Lacser and Arya, 1986) to the turbulence parameterization. Such detail cannot be included in large scale models as in the present case.

In the present formulation, the eddy diffusivity for momentum is given as

$$K_m = \frac{u_* k z}{\phi_m}(1 - \frac{z}{h})^p \tag{4}$$

with u_* the surface friction velocity, given by

$$u_* \equiv \sqrt{C_m \left| V_H \right|^2} \quad , \tag{5}$$

k is von Kármán's constant, taken here to be 0.4, z the model height, ϕ_m the nondimensional shear function, and p=2. This follows the treatment of Brost and Wyngaard (1978). Following Businger *et al.* (1971), the shear function takes the form

$$\phi_m = (1 + 4.7\frac{z}{L}) \tag{6}$$

under stable conditions, where L is the Monin-Obukhov length

$$L \equiv - \frac{u_*^3}{g k \left(\overline{w'\theta_v'} \right)_s} . \tag{7}$$

Although (6) was intended for use in the surface layer, some PBL models simply use the same form in the parameterization for turbulence in the outer layer as well, with the $(1 - {}^{z}/_{h})$ factor included to allow for gradual decrease of K_m as the top of the boundary layer is approached.

TM86 show that in their model, K_m effectively reduces to

$$K_m = 0.09\ L\ u_* \left(1 - \frac{z}{h}\right)^p , \qquad \frac{z}{L} > 1 . \tag{8}$$

On dimensional grounds, the eddy diffusivity can be seen as the product of a velocity and length scale, so that

$$K_m \sim l\ U \quad . \tag{9}$$

Comparing (9) to (8) would seem to indicate L is one of the relevant length scales for turbulent mixing above the surface layer in TM86. However, the Monin-Obukhov length is a valid length scale only in the surface layer according to similarity theory; the surface layer may be only a few meters deep under very stable conditions. In some of our 1-D PBL sensitivity experiments, L is about 1 m, and therefore the surface inversion layer extends well above L. Brutsaert (1982) notes that for ${}^{z}/_{L} > 1$, observations support use of a constant value of ϕ_m, such as that suggested by Kondo *et al.* (1978),

$$\phi_m = 6 \quad . \tag{10}$$

Most recently Lacser and Arya (1986) and Sorbjan (1987) have, in observational and modelling studies, respectively, verified fairly constant vertical profiles of the nondimensional shear functions ϕ_m and ϕ_h.

Since K_m is *inversely* proportional to ϕ_m, a limitation of the maximum value on ϕ_m corresponds to substantially larger diffusivities, increased mixing in the PBL, and a deeper surface inversion layer, compared to TM86 and previous models. This constant ϕ_m formulation incorporates observations which virtually suggests a third regime for boundary

layer stability in the model, namely the *very* stable case. This tendency for three regimes of boundary layer stability based on the bulk Richardson number has been noted in observational studies in the past, including Portman *et al.*, (1962), Kondo *et al.*(1978), and Mahrt (1987).

In the changed model studied here, the third regime is enacted if $^{z}/_{L} > 1$ in the outer layer. The new eddy diffusivity is adopted here by modifying the nondimensional shear function as alluded to earlier:

$$\phi_m = \begin{cases} (1 - 7\frac{z}{L})^{-1/3} , & L < 0 \\ (1 + 4.7\frac{z}{L}) , & 0 \le \frac{z}{L} \le 1 \\ 6 , & \frac{z}{L} > 1 \end{cases} . \qquad (11)$$

d. Summary of sensitivity studies

The experiments performed and the parameters changed in the runs are summarized in Table 6.1; changes are indicated in italics. The three changes should show some improvement if incorporated into TM86 separately, but we might expect the results to be best if they are all coupled in one run. This makes sense in view of the results of Chapter V and other observational studies which have shown that although the large eddies in the SBL are important features of the flow, they do not contribute much to the overall mixing which is occurring. This mixing appears to be concentrated at the edges of the eddies. Such a small-scale feature cannot be adequately resolved in a global model, so horizontal averaging is implied.

The formulation of Mahrt (1987) was designed to represent the implied horizontal averaging. The increased surface exchange coefficient leads indirectly to increased vertical mixing through the parameter u_*, as seen in Fig. 6.3. This figure is a representation of only the "first-order" feedbacks of the parameters indicated; others of course are occurring which are not shown.

An increase in the surface temperature will result from these last two modifications described, and by increasing the critical Richardson number, we can increase the PBL height. This will produce mixing over a deeper boundary layer, perhaps further increasing the surface temperature. Such an increase of Ri_c is warranted also in view of the analysis of Chapter V, where very small-scale mixing zones are seen to exist despite overall very stable stratification on the larger scale. By allowing turbulence to continue in the model boundary layer under more stable conditions (through use of a larger critical Richardson number), we are effectively adding another facet to the parameterization of turbulence in the very stable boundary layer.

Table 6.1

Sensitivity Experiments

Run	Ri_c	C_h	K_h
CONTROL	1.0	Louis	TM86
TM86	*0.5*	Louis	TM86
RIC=3	*3.0*	Louis	TM86
RIC=5	*5.0*	Louis	TM86
MCH1.0	1.0	*Mahrt, m=1*	TM86
MCH0.75	1.0	*Mahrt, m=0.75*	TM86
MCH0.1	1.0	*Mahrt, m=0.1*	TM86
KONDOK	1.0	Louis	*new* ϕ_m
ALL	*5.0*	*Mahrt, m=1*	*new* ϕ_m

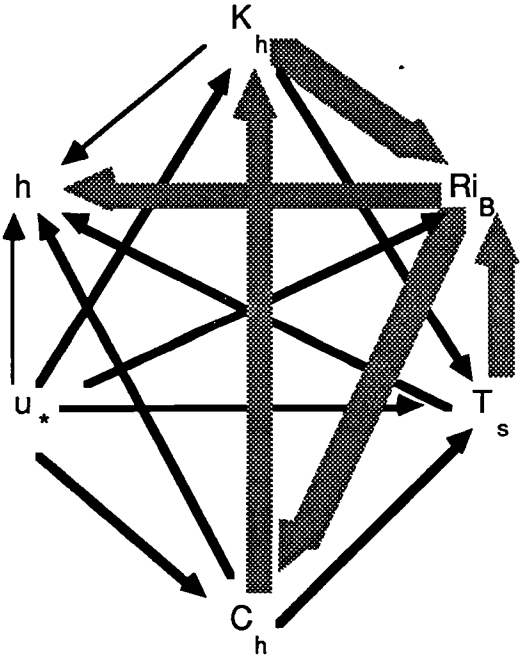

Figure 6.3. Interrelationships between several parameters in the proposed SBL treatment. Solid arrows represent positive feedback, large dotted arrows indicate negative feedback. The direction of the arrows show which variable is affected (at the head of the arrow).

3. Results

a. Specification of PBL height

In the model of TM86, a value of 0.5 for the critical Richardson number is used; the value in the present control run is 1.0. Runs of the model were also made for $Ri_c = 3$ and $Ri_c = 5$. The most pronounced impact of this change is expected to be found in the PBL height from (2), this is shown in fig. 6.4. The daytime boundary layer height depends very little on the critical Richardson number; it depends much more on the temperature profile. There is not a great impact on other variables, such as skin temperature (fig. 6.5), except that in the TM86 run, dew was predicted, and the additional condensational heating warmed the surface about 1.5°C.

The vertical temperature profile after 46 hr of integration time, roughly the time of minimum temperature is depicted in fig. 6.6. This figure will be referred to in the sections which follow involving other comparisons. The vertical temperature structure for the runs with other critical Richardson numbers are qualitatively similar to fig. 6.6, but there is some tendency for predicted boundary layer height to not match the inversion top, due to the sharpness of the initial potential temperature profile. The increased critical Richardson number does have the desired effect of deepening the SBL. This is important because predictions of SBL height for 5 m s^{-1} winds in the model of TM86 seem unrealistically shallow.

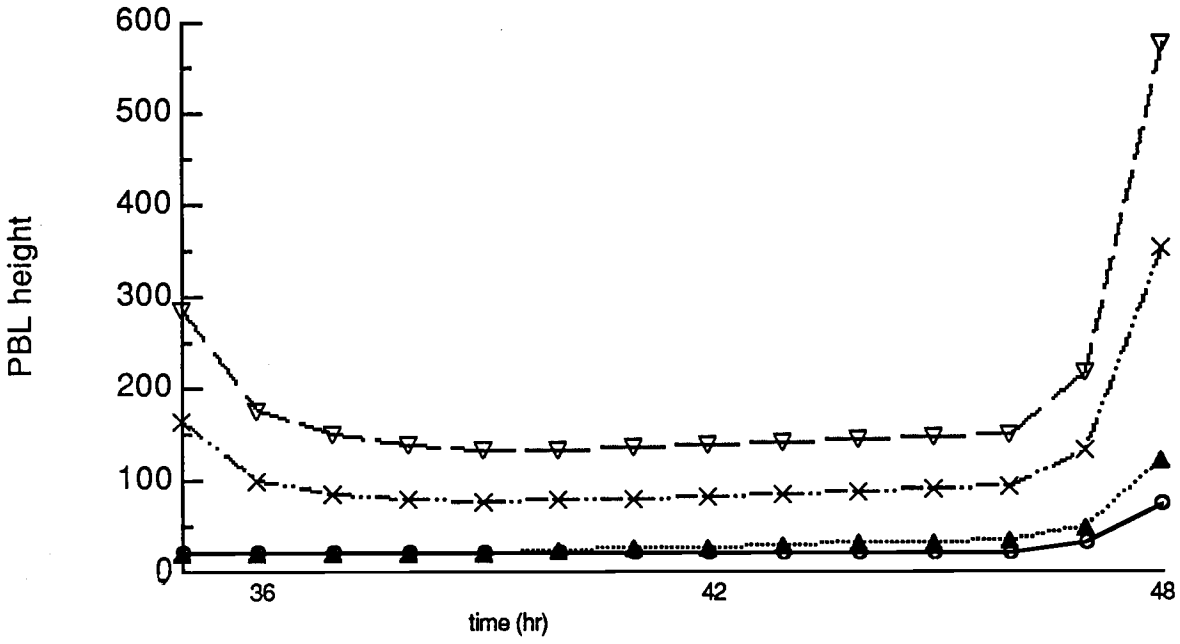

Figure 6.4. The effect of critical Richardson number on diagnosed boundary layer height for the control run (solid triangles); TM86 (open circles); $Ri_c = 3$ (×); $Ri_c = 5$ (inverted open triangles).

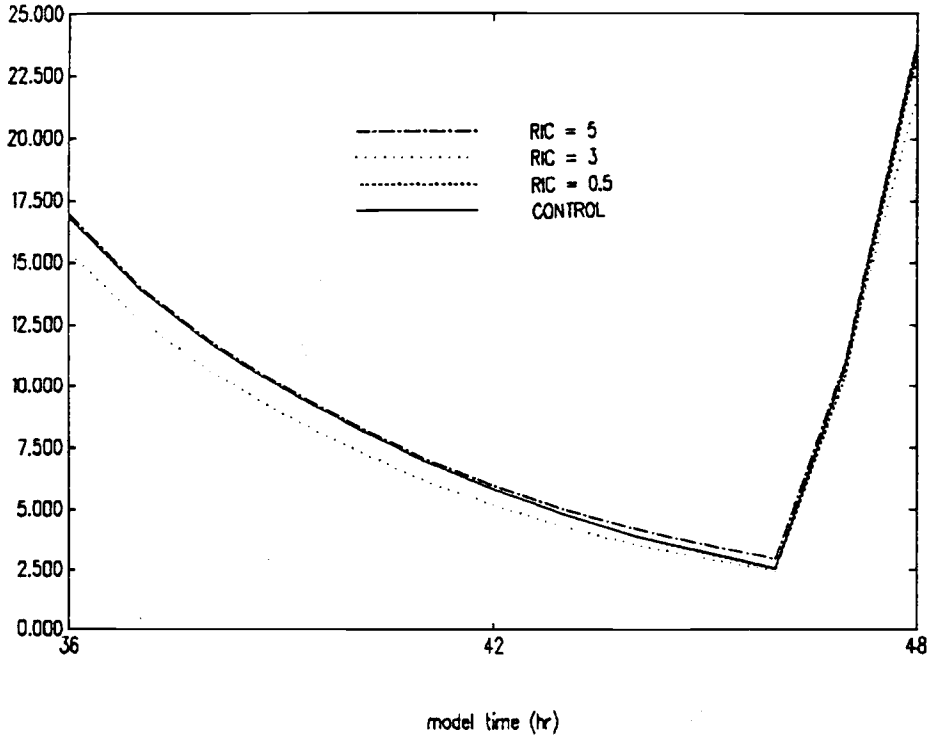

Figure 6.5. Effect of critical Richardson number change on skin temperature.

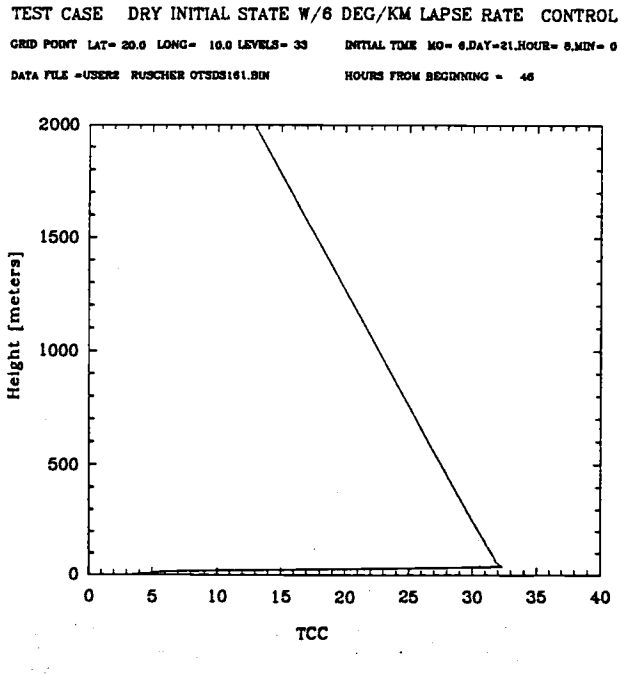

Figure 6.6. Predicted vertical temperature profiles for the control run after 46 hr.

b. Smooth exchange coefficient

This section discusses the impact on the SBL formulation of changing the formulation of the surface exchange coefficient. Mahrt (1987) recommends a value of m in Eq. 3 or order 1; here we test three values of m (1.0, 0.75, and 0.1). Because the new C_h falls off exponentially as $-m\ Ri_B$, a smaller value of m will enhance the exchange coefficient (fig. 6.2). Recall also the primary reason for this change; an attempt to represent the implied horizontal grid-area averaging of large subgrid scale variations of C_h, which presumably acts to increase the surface temperature.

Inclusion of the modified exchange coefficient increases the value of C_h by a factor of five, causing the skin temperature to increase, but only 0.1°C (fig. 6.7) The enhanced C_h (five times the value in the control run) more strongly mixes the lowest layer so as to *reduce* the 20 m temperature by 1.5°C (fig. 6.8). Even with m=0.1, the increase in skin temperature was a modest 0.6°C compared to the control run. Neither the PBL height nor the surface energy balance terms showed any appreciable difference for the various values of m and the control run.

Apparently the modified surface exchange coefficient to enhances downward mixing of heat when the model boundary layer is stably stratified, cooling the atmosphere but only slightly warming the surface skin temperature.

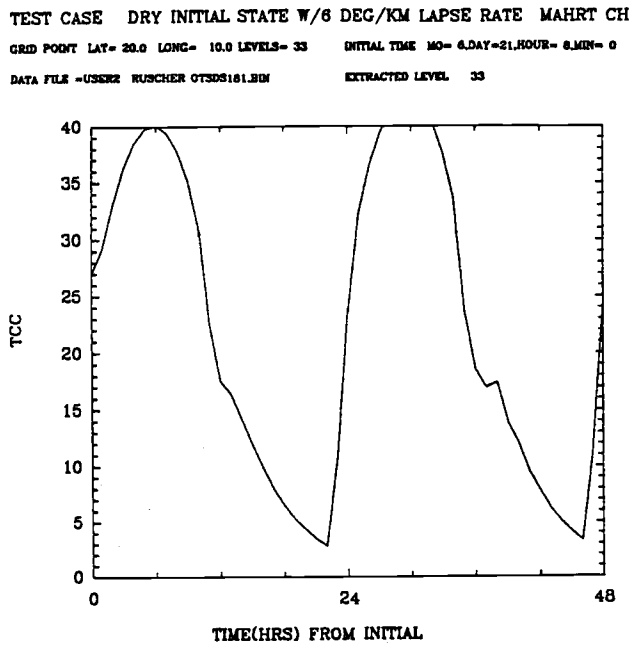

Figure 6.7. The time series of skin temperature for the modified exchange coefficient run with m = 1.

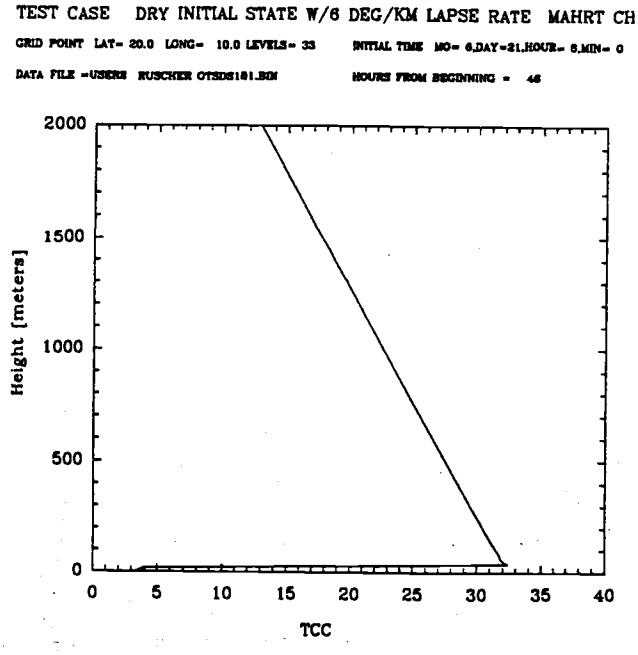

Figure 6.8. Predicted vertical temperature profile after 46 hr for the modified exchange coefficient run; m = 1.

c. Enhanced eddy diffusivity

This section describes the effects of the modified K_h, which is expected to enhance downward mixing of sensible heat at night, partially ameliorating the effects of longwave radiative heat loss from the earth's surface.

After 46 hr for the control experiment, the boundary layer depth is only 40 m (fig. 6.9a), so that there are only three levels which have non-zero heat flux. In addition, the heat flux at the surface and lowest model level are always taken to be equal.. The effect of increased diffusivity with the Kondo formulation causes the surface heat flux to decrease from -2.8 W m^{-2} for the control run to -10.5 W m^{-2} (fig. 6.9b).

The Kondo formulation for eddy diffusivity increases the predicted surface temperature by 0.6°C and increases the predicted air temperature by several degrees (fig. 6.10). As a result, the temperature difference between the inversion top and the surface is substantially reduced. Increased magnitudes of downward sensible heat flux lead to warming in the lower boundary layer, and cooling at the boundary layer top (fig. 6.11), as expected. The Kondo modification apparently exerts greater impact than the other two changes involving tunable parameters.

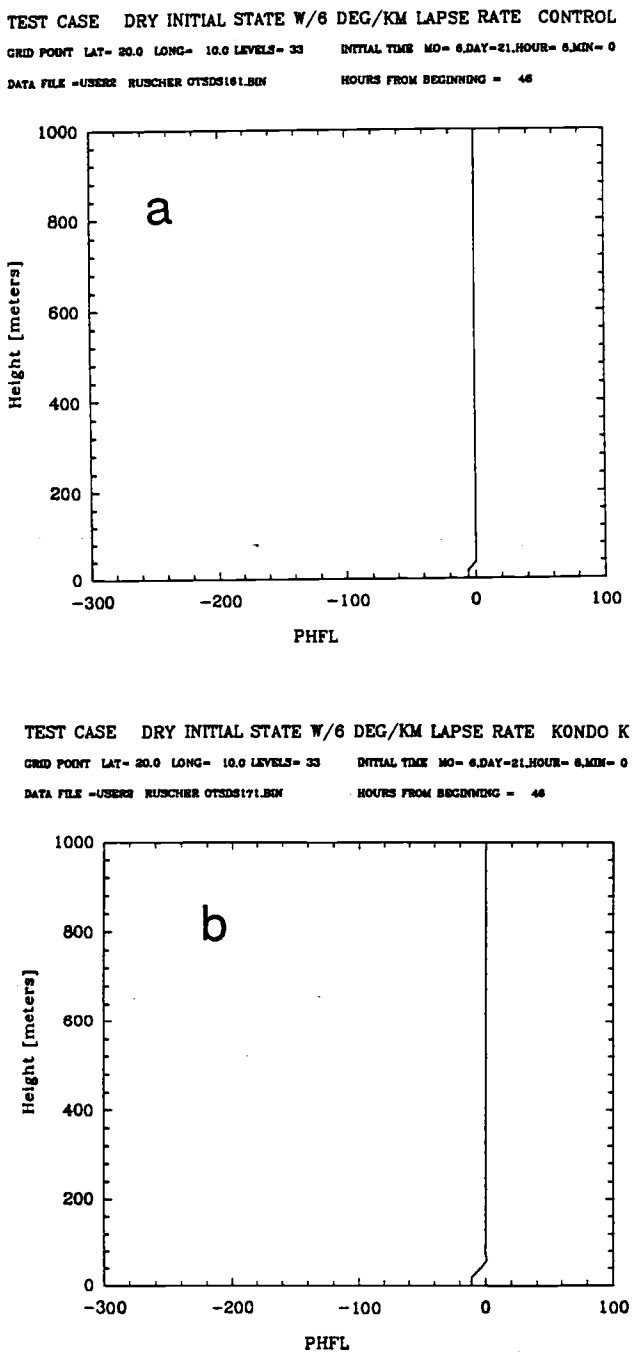

Figure 6.9. Vertical profile of heat flux after 46 hr: (a) for the control experiment; (b) for the enhanced eddy diffusivity experiment.

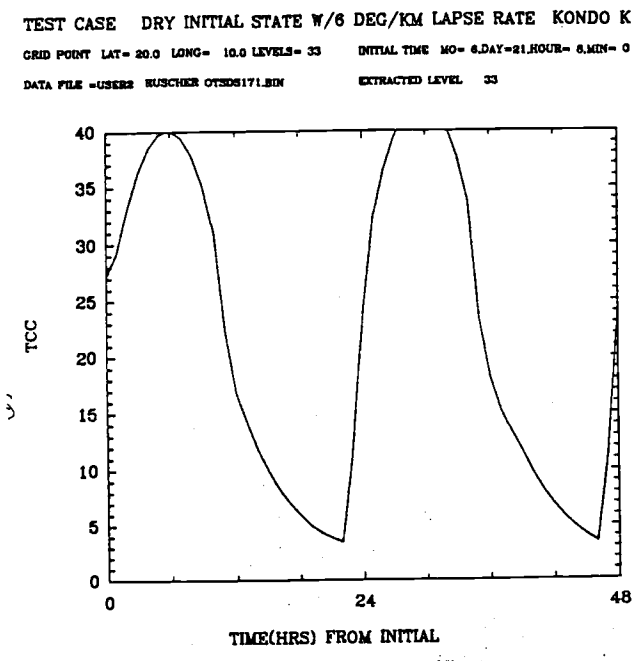

Figure 6.10. Time series of skin temperature for the enhanced eddy diffusivity experiment.

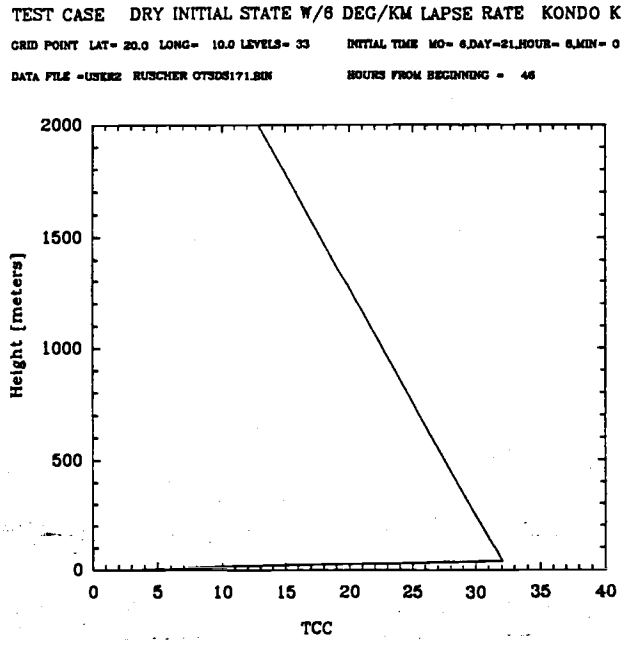

Figure 6.11. Vertical temperature profile after 46 hr for the enhanced eddy diffusivity experiment.

d. Summary and synthesis

The first two revised formulations for the SBL parameterization scheme lead to the desired effects, an increased PBL height and enhanced surface temperature, although the impacts seen in modified exchange coefficient experiments were quite small. It was decided that all three formulations would be incorporated into a final run; combined, these changes might be expected to work together in a synergistic effect.

By increasing the PBL height through the modification of the critical Richardson number, the Kondo-K modification affects a much deeper boundary layer, significantly changing the vertical temperature profile (fig. 6.12). The surface temperature is significantly changed, as well, increasing by nearly 5°C over the control run. The surface exchange coefficient modification plays a role here, as well. The effect of increasing the eddy diffusivity alone has the undesirable effect of reducing the exchange coefficient. Apparently by smoothing out the boundary layer temperature profile and momentum profile through increased mixing, u_* will be reduced, since it depends on the vertical difference of wind speed between the surface and lowest model layer. This reduction of the surface exchange coefficient does not occur when all three changes are made. This effect is seen in figure 6.13, a time series of the Kondo-K prediction of C_h and that of the control experiment. The way the Kondo-K formulation works with the other two changes is reason enough for recommending that all three changes be implemented in further tests of this revised SBL parameterization for the 1D model. Their minimal impact on daytime changes is important, as we do not wish to alter the character of the daytime PBL, which is controlled by a completely different set of equations due to the quite different dynamics involved.

The three modifications in concert lead to a more realistic boundary layer depth for 5 m s^{-1} winds (172 m compared to 20 m; fig. 6.14), matching the boundary depth with the inversion top during periods of boundary layer growth, and warmer temperatures due to

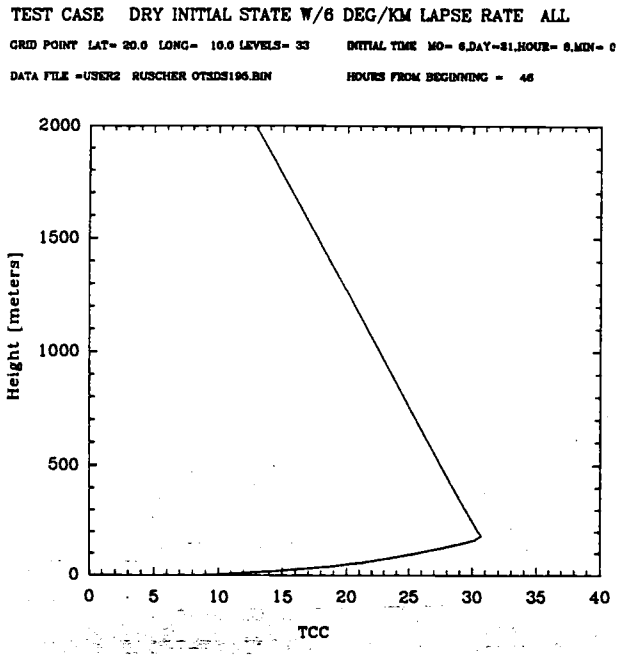

Figure 6.12. The vertical temperature profile after 46 hr for the experiment made using all modifications to the SBL parameterization.

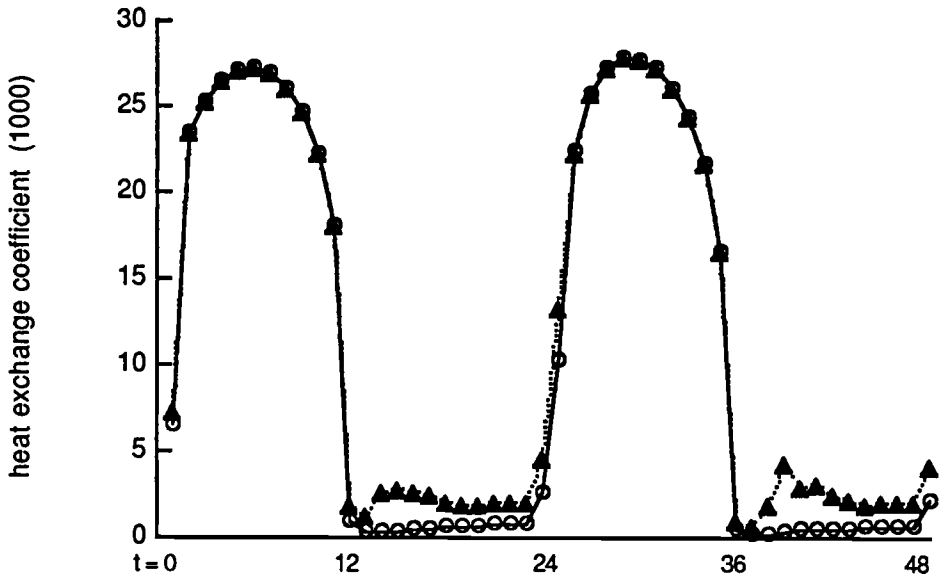

Figure 6.13 Time series of surface heat exchange coefficient for the MCH1.0 (solid triangles) and KONDOK (open circles) experiments.

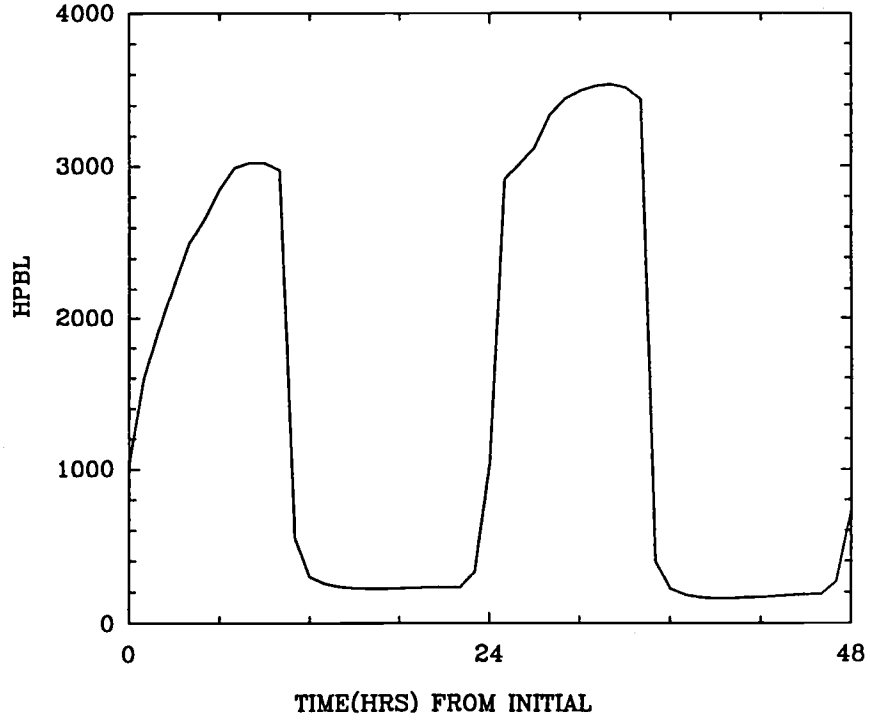

Figure 6.14. Time series of boundary layer height for the experiment with all modifications included.

increased downward heat flux.

The results of all experiments are summarized in Table 6.2 (z_i refers to the height of the inversion; T_2 is the air temperature at the lowest model level above the surface). Of course, the model initial conditions are highly idealized in this case. In the next section, Wangara day 33 is chosen as an initial condition for one run, while a winter snow cover simulation is carried out in a second simulation. For these comparisons, only the control run and the run with all changes are shown here.

Table 6.2
Results of Changes to Stable Layer Formulation for idealized dry sandy soil case

Run	h (m)	z_i (m)	T_S (°C)	T_2 (°C)
Control	40	38	2.7	5.0
TM86	20	38	4.3	9.1
RIC=3	142	38	2.5	6.3
RIC=5	172	38	3.0	8.4
Mahrt C_h, m=1	40	38	2.8	3.5
Mahrt C_h, m=0.75	40	38	2.9	3.6
Mahrt C_h, m=0.1	44	38	2.5	2.9
Kondo-K	42	38	3.3	11.3
ALL	191	181	8.0	14.0

4. Other tests

a. Wangara Day 33

The initial vertical temperature profile for 0610 EST (Eastern Australia Standard Time) on Wangara day 33 is shown in fig. 6.15a. The surface temperature is just below freezing and a strong radiation inversion develops under conditions of high pressure, clear skies, and modest winds. The modified model predicts much warmer surface temperatures than the control run (fig. 6.16). The observed surface temperature at 0604 on day 35 was 7.3°C. The control run predicted a surface temperature of 2.1°C, while the modified run yielded 7.6°C, quite close to the observed value.

The heat flux for the modified model run is much larger than the control run (fig. 6.17). Due in part to the increased heat flux, z_i for the modified run is 288 m, while it is only 122 m for the control; this is not a result of only the enhanced diffusivity as the increased Ri_c also plays a role. The observed inversion top at 0623 on Wangara day 35 was 400 m (fig. 6.15b); again the modified model results look superior. However, this is tempered by the observation that the strength of the inversion (measured here in terms of $T_{z_i} - T_{sfc}$) for day 35 was only 3.4°C; the modified run had a vertical temperature change of 7.3°C, while the control run had an inversion strength of 13.4°C! There is certainly room for improvement and runs which include prescribed vertical motion and perhaps the cloud model of Chu (1986) are indicated in future research. Nevertheless, the comparison indicates optimistic results for the three model changes.

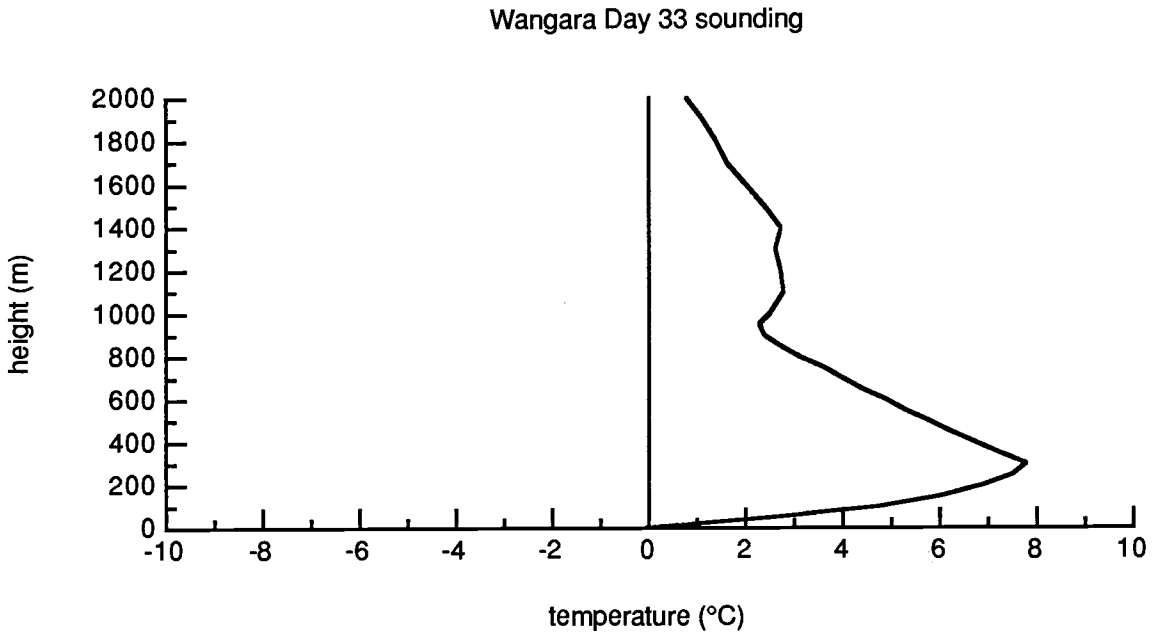

Figure 6.15a. Observed temperature from early-morning sounding for Wangara day 33.

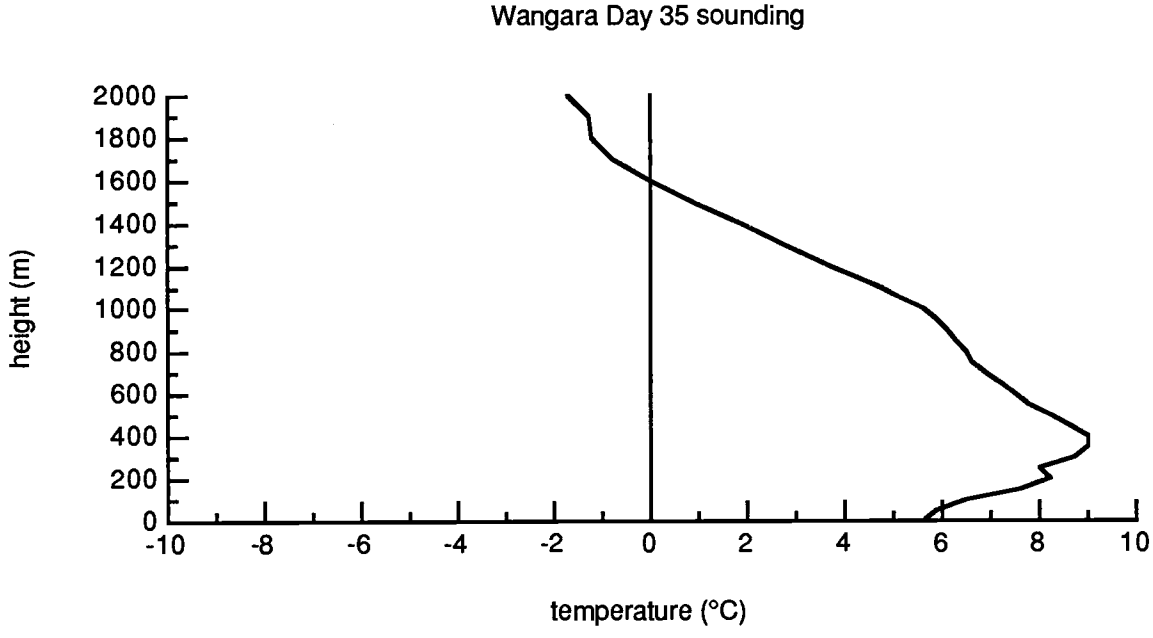

Figure 6.15b. As in Fig. 6.15a except for Wangara day 35.

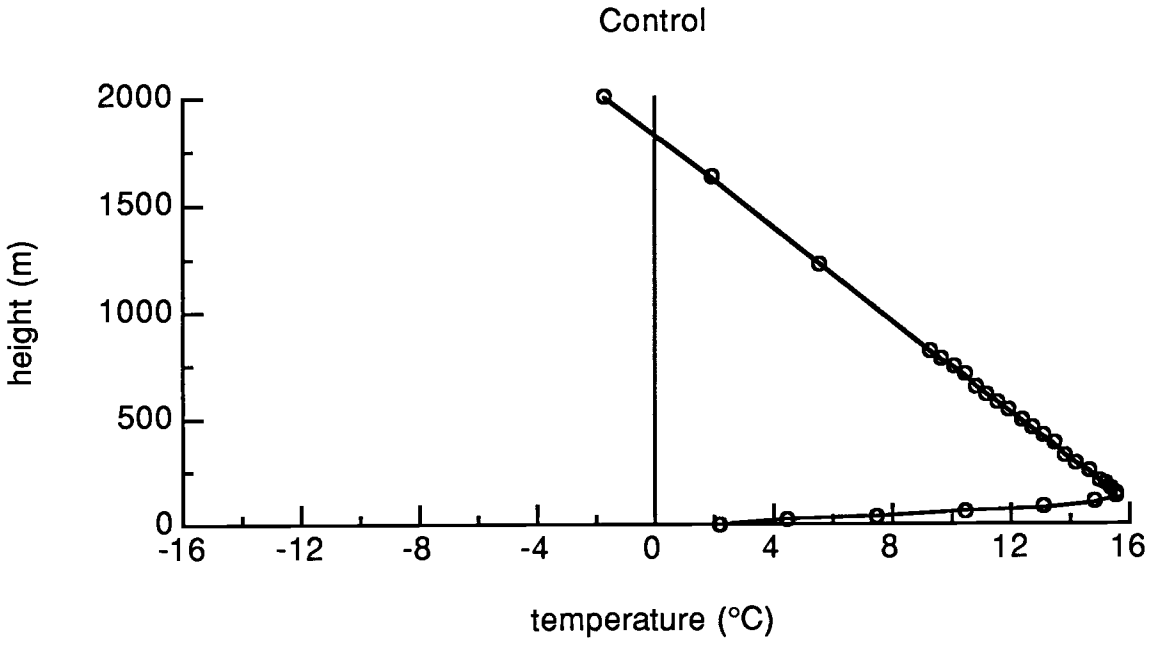

Figure 6.16a. Simulated Wangara temperature profile for control run after 48 hr.

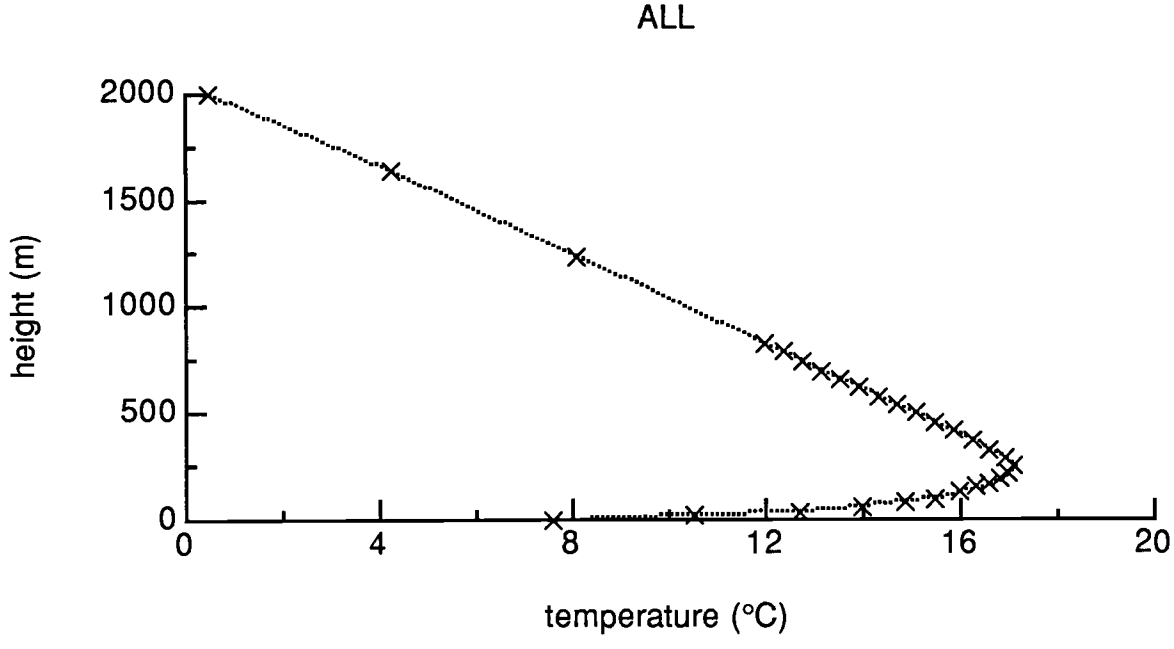

Figure 6.16b. As in Fig. 6.16a except for modified run.

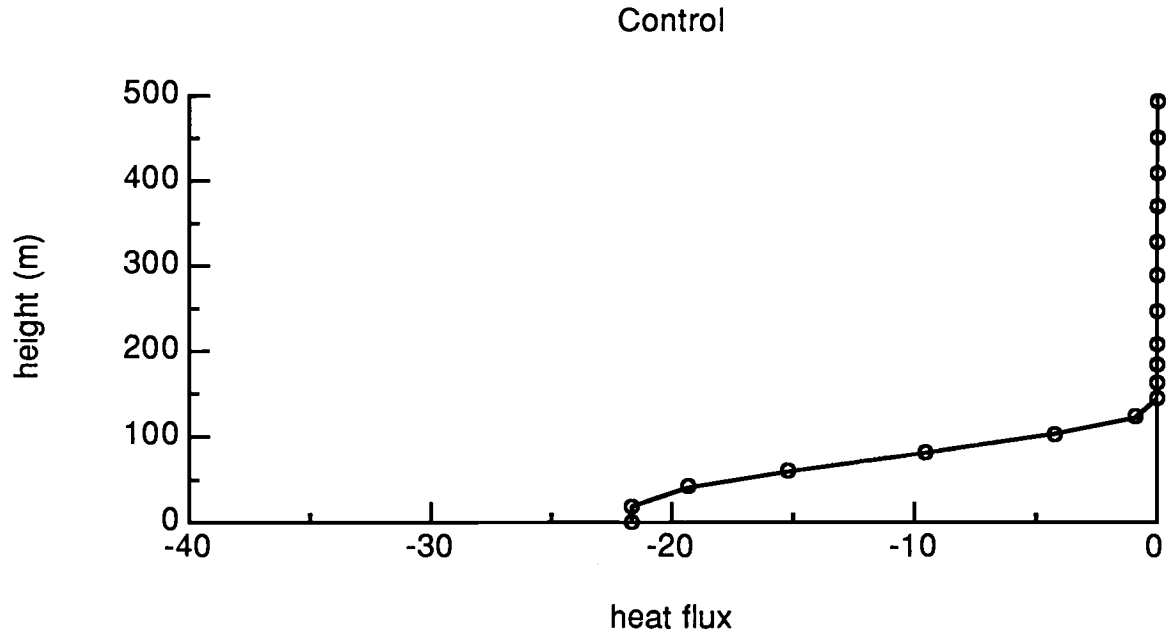

Figure 6.17a. Simulated vertically-integrated heat flux profile (W m^{-2}) after 48 hr for the Wangara control run.

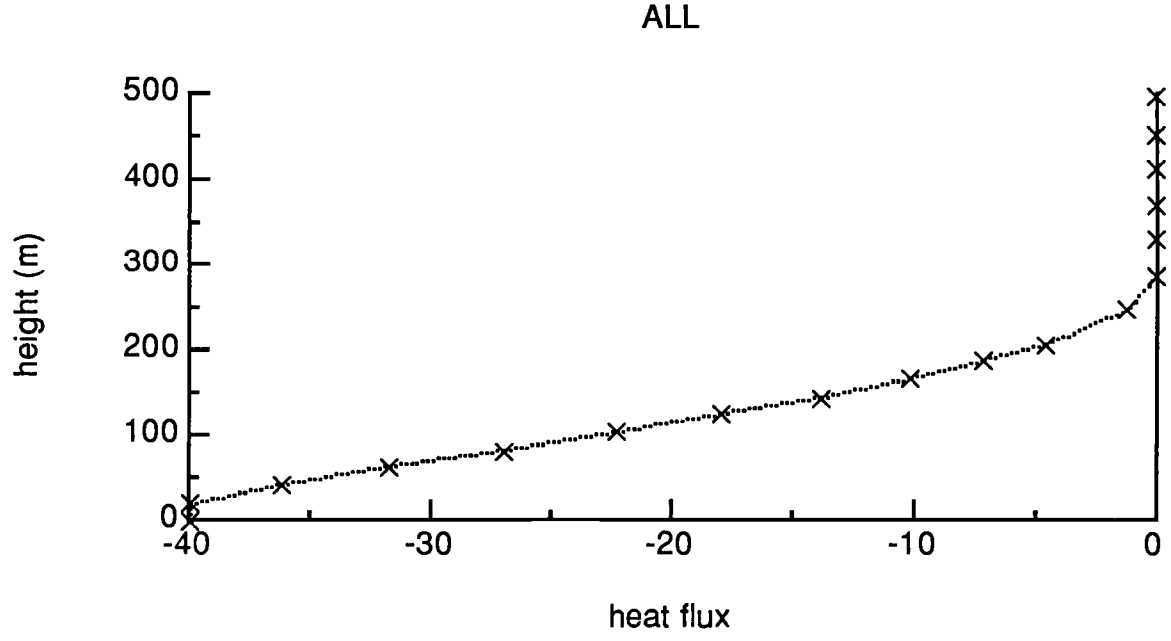

Figure 6.17b. As in Fig. 6.17a except for the Wangara modified run.

b. Winter snow cover simulation

Sensitivity tests were also performed for the 1-D model run with a surface snow cover, the surface snow cover model of Pan (1987) is included in this run. The initial conditions for this test are a 10 cm snow cover, and a 1200 GMT sounding taken from The Pas, Manitoba, during February of 1987. There were northwest winds of about 5 m s^{-1} near the surface; again, moisture effects are not included. Comparison to observations is of course an impossibility here because of the neglected large-scale forcing.

A pronounced inversion typical of the arctic or well-developed cP (continental polar) air mass is present in the initial temperature profile (fig. 6.18). The control run is colder at the surface than the modified run after 46 hr, as expected (fig. 6.19). The diagnosed PBL height is 160 m for the modified model, compared to 41 m for the control model; in each case the surface inversion has a deeper inversion overlying it, a manifestation of the original input data. The vertical temperature profile for the modified case (fig. 6.20) is quite typical of high-latitude wintertime inversions (Dalrymple, 1966). Sensible heat transport seems to be playing an important role in the maintenance of the inversion in this test.

Oke (1978) presents a typical surface energy balance over snow cover and a main feature is a negative sensible heat flux. The model-simulated sensible heat fluxes are -3.0 W m^{-2} and -16.7 W m^{-2} for the control and modified runs, respectively; Oke reports values of order -10 W m^{-2}. Other than these comparisons, we cannot make any definitive conclusions either about the abilities of the snow cover model or about the impact which the modifications will have on snow cover simulations.

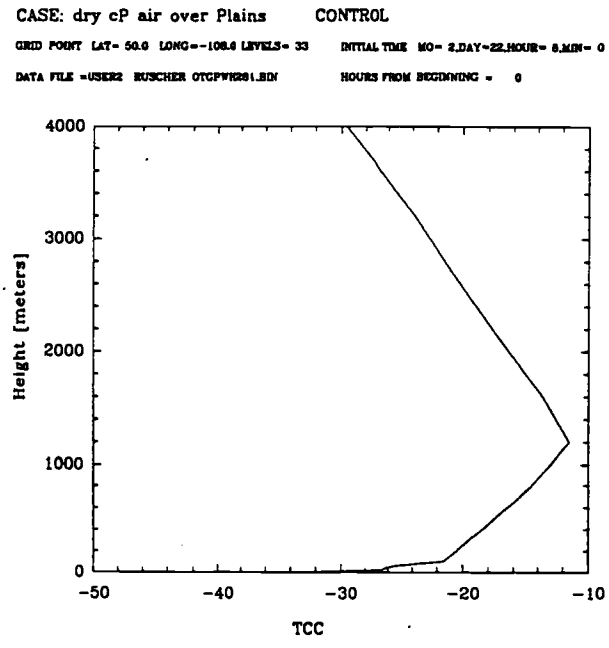

Figure 6.18. Initial temperature profile for snow cover simulation.

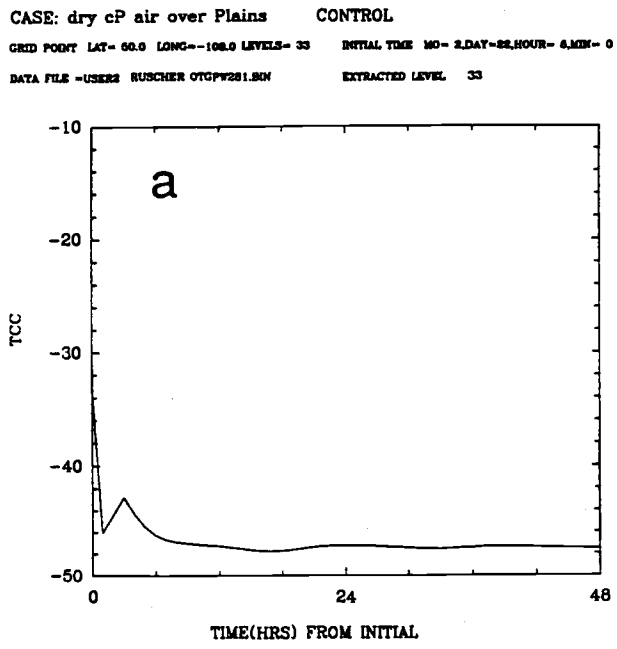

Figure 6.19a. Time series of skin temperature for the control run of the snow cover case.

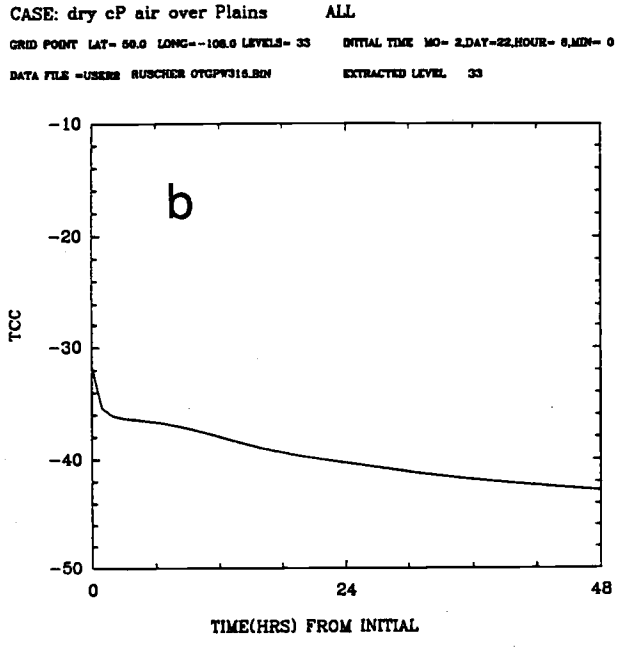

Figure 6.19b. As in Fig. 6.19a except for modified run.

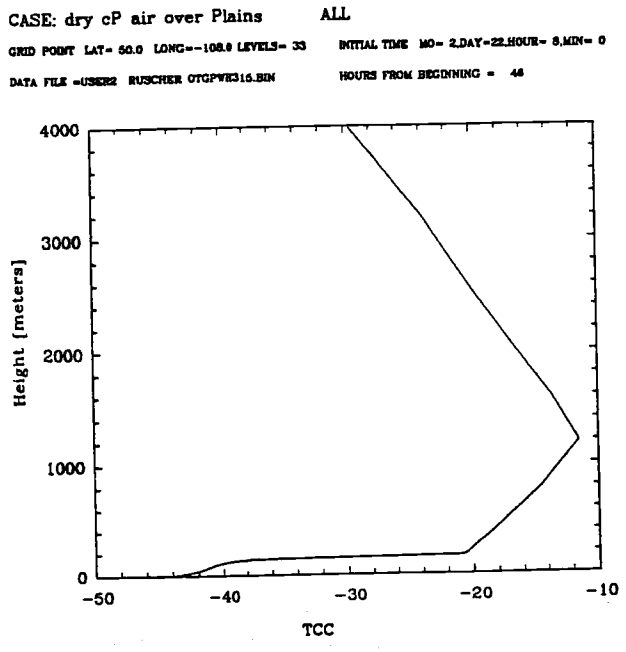

Figure 6.20. Temperature profile after 46 hr for the modified snow cover simulation.

5. Conclusions

Three changes have been made to the stable layer formulation of the model of TM86 which significantly improve the performance of the model. The critical Richardson number change involves strictly a "tunable" parameter, in that observations are not definitive. This is probably the hardest to justify based on observational evidence, but it seems necessary to provide for realistically deep stable boundary layers with moderate wind speeds. Strong support exists for the other two changes, however, enhancements to the surface exchange coefficients and boundary layer eddy diffusivity. In tests with an idealized atmosphere, the results indicate that the three proposed changes seem to work in a synergistic manner to improve the prediction of SBL physics, including PBL depth, surface skin temperature, and vertical temperature profile. Although improvements are noted for the changes tested individually, only the increased critical Richardson number change led by itself to a boundary layer significantly different from the control model.

The revised model was also tested for two very different conditions. One was a wintertime snow cover situation from February 1987 over the Canadian prairie, the other was for the Wangara field experiment. Although direct comparison with observations is not possible in either case because this simple model must neglect some large-scale processes, results of the revised SBL model are encouraging.

Once further tests of these formulations are made, which will be the subject of future research, other possible modifications to the stable layer formulation might be considered. For example, currently in TM86 and in the model calculations described in the present research, the ratio of the heat exchange coefficient (C_h) to the drag coefficient (C_m) is set to be 1.35 (this is also true for K_h/K_m), following Businger *et al.* (1971). This value (which corresponds to a Prandtl number $Pr = 1.35^{-1} = 0.74$) has been shown to be valid for near-neutral conditions, but its value in conditions far from neutral still seems to be somewhat controversial. For example, Kondo *et al.* (1978) suggest a ratio much

smaller than one. One might expect the logic behind this is that pressure fluctuations due to gravity waves, ubiquitous in the SBL, transport momentum but not heat (Finnigan and Einaudi, 1981, Caughey, 1982, and Hunt *et al.*, 1985). It could be noted here also that the pressure perturbations due to the turbulence itself may lead directly to momentum transport (Schols and Wartena, 1986). While these observations are valid for linear wave motions, the stably-stratified PBL is thought to contain highly nonlinear motions, as the analysis of Chapter V has shown; which would transport heat, as well. Parameterization of turbulence in the free atmosphere is another area which requires some research.

The results for the snow cover simulation in particular should be deemed very preliminary at this point. Comparison with observed data using a more realistic model (including vertical motion, advection, and clouds, for example) also needs to be performed. Still, the fact that these simple modifications are able to abate the nocturnal cooling is encouraging and they warrant further testing.

Chapter VII

Conclusions

This study has involved diagnosis and modelling of motions in the very stable boundary layer. Our attention here has focussed upon the analysis of coherent structures and their edges where shears may be quite large. Data from several aircraft flight legs from synoptically quiescent periods of the SESAME are used to identify these structures.

Several approaches were taken. Inferences based on spectral techniques alone were found not to be very reliable for very stable layers with intermittent turbulence. Sharp gradients are not resolved well with Fourier analysis. Rotary spectral analysis was used to better illustrate interrelationships between variables, but this technique is subject to the same sampling problems as any other spectral technique.

Other analysis tools better suited to studies of flows with sharp gradients include the structure function and principal component analysis. A new conditional sampling technique which requires little *a priori* specification of sampling criteria was developed in this research based on principal component analysis. Conditionally-sampled coherent structures 400 m to 500 m in width were found at the top of a surface-based nocturnal inversion layer, where weak northwesterly cold air drainage flows existed underneath weak southerly flow. Much of the flux is confined to narrow shear zones at the edges of the main coherent structures.

The significant fluxes present on very small horizontal scales, even under very strong ambient stratification, imply resolution problems for most numerical models. Because the stable boundary layer may be characterized by large vertical gradients over very short distances and intermittent turbulence and other motion types, any practical modelling will be a rather rough approximation, and therefore might as well be simple. Most simple approaches, however, have relied on observations of only the surface layer,

which typically represents only the lowest ten per cent of the stable boundary layer.

The observations reported here and elsewhere have suggested that there can be important vertical transport of heat as well as momentum under very stable conditions. Most parameterization schemes of the stable boundary layer incorrectly discontinue the modelled turbulent transport once the stratification reaches a specified critical level, leading to incorrect elimination of fluxes at large stability. A few new theoretical approaches involving the transition to turbulence and local similarity theory lead to maintenance of the turbulence to greater values of the static stability.

The three parameterization changes tested here appear to work in a synergistic manner to improve vertical mixing in the stable boundary layer. This appears to lead to improved forecasting of minimum temperature and boundary layer depth. Further tests of the new stable layer parameterizations need to be carried out for a variety of surface types and meteorological conditions. The one-dimensional model tests will be very important before incorporation of the changes into a large-scale dynamical model. Further refinement of the parameterizations is a possibility as well, using local similarity theory as a basis, provided the resultant changes remain computationally non-demanding.

This combined diagnostic and modelling study of the horizontal structure of the very stable boundary will hopefully provide useful information to those involved in designing experiments for field programs, which should be designed to take the data needs of turbulence studies into account. Also, it is hoped that the modelling community will take a serious look at the importance of specification of the complicated boundary layer physics as a high priority. However, for the short term, direct modelling of the very small scale features is out of the question for large-scale models, but existing treatments could be modified to improve the forecast parameters discussed above.

For future research, it is recommended that spectral analysis be used in conjunction with other techniques for flows of the very stable boundary layer, for the reasons cited by many other authors. Even for comparison with previous datasets and theoretical

expectations, serious sampling problems may develop; as the Fourier analysis attempts to resolve sharp gradients it spreads variance over the entire spectrum. Spectral analysis is a global approach and its use requires conditional sampling, with *a priori* specification of sampling criteria. In this study, a conditional sampling procedure with less subjective specification was developed which relied on principal component analysis to pick samples. Structure function analysis and eigen techniques are much more able to resolve sharp gradients with minimal sampling problems. Higher order structure functions would be of great interest, as pointed out by Frisch and Sulem (1978), provided that the sampling problems associated with higher-moment statistics can be worked out.

Bibliography

Abarbanel, H. D. I., D. D. Holm, J. E. Marsden and T. S. Ratiu, 1986: Nonlinear stability analysis of stratified fluid equilibria. *Phil. Trans. Roy. Soc. London*, **A318**, 349-409.

Alberty, R. L., D. W. Burgess, C. E. Hane and J. F. Weaver, 1979: *Project SESAME 1979 Operations Summary*. National Oceanic and Atmospheric Administration, Environmental Research Laboratory, Boulder, Colo., 253 pp.

André, J.-C. and L. Mahrt, 1982: The nocturnal surface inversion and influence of clear-air radiative cooling. *J. Atmos. Sci.*, **39**, 864-878.

Asai, T., 1970: Three-dimensional features of thermal convection in plane Couette flow. *J. Meteorol. Soc. Japan*, **48**, 18-29.

Axford, D. N., 1971: Spectral analysis of an aircraft observation of gravity waves. *Quart. J. Roy. Meteorol. Soc.*, **97**, 313-321.

Barnes, S. L., 1979: SESAME 1979 Field-Processed Rawinsonde Data from Supplemental Sites: April 10 — June 8. NOAA/ERL, Boulder, CO, 252 pp.

Blackwelder, R. F. and R. E. Kaplan, 1976: On the wall structure of the turbulent boundary layer. *J. Fluid Mech.*, **76**, 89-112.

Blumen, W., 1984: An observational study of instability and turbulence in nighttime drainage winds. *Bound.-Layer Meteorol.*, **28**, 245-269.

Bolgiano, R., Jr., 1959: Turbulent spectra in a stably stratified atmosphere. *J. Geophys. Res.*, **64**, 2226-2229.

Bolgiano, R., Jr., 1962: Structure of turbulence in stratified media. *J. Geophys. Res.*, **67**, 3015-3023.

Böttger, H., 1987: Changes to the operational forecasting system. *ECMWF Newsletter* No. 38 (June), 1-9.

Brenner, S., C.-H. Yang and K. Mitchell, 1984: The AFGL Global Spectral Model: Expanded Resolution Baseline Version. Rept. No. AFGL-TR-84-0308, Air Force Geophyics Laboratory, Hanscom AFB, MA, 72 pp.

Brock, F.V. and P.K. Govind, 1977: Portable automated mesonet in operation. *J. Appl. Meteorol.*, **16**, 299-310.

Brost, R. A. and J. C. Wyngaard, 1978: A model study of the stably stratified boundary layer. *J. Atmos. Sci.*, **35**, 1427-1440.

Busch, N. E., N. K. Vinnichenko, A. T. Waterman, Jr., C. Beard, R. W. Stewart and R. S. Scott, 1969: Waves and turbulence. *Radio Sci.*, **4**, 1377-1379.

Businger, J. A., J. C. Wyngaard, Y. Izumi and E. F. Bradley, 1971: Flux-profile relationships in the atmospheric surface layer. *J. Atmos. Sci.*, **28**, 181-189.

Caldwell, D. R., 1983: Oceanic turbulence: big bangs or continuous creation? *J. Geophys. Res.*, **88C**, 7543-7550.

Caldwell, P. C., D. W. Stuart and K. H. Brink, 1986: Mesoscale wind variability near Point Conception, California during Spring 1983. *J. Clim. Appl. Meteorol.*, **25**, 1241-1254.

Calman, J., 1978a: On the interpretation of ocean current spectra: I. The kinematics of three-dimensional vector time series. *J. Phys. Oceanogr.*, **8**, 627-643.

Calman, J., 1978b: On the interpretation of ocean current spectra: II. Testing dynamical hypotheses. *J. Phys. Oceanogr.*, **8**, 644-652.

Carruthers, D.J. and J.C.R. Hunt, 1986: Velocity fluctuations near an interface between a turbulent region and a stably stratified layer. *J. Fluid Mech., **165**,* 475-501.

Caughey, S. J., 1982: Observed characteristics of the atmospheric boundary layer. In *Atmospheric Turbulence and Air Pollution Modelling* (F. T. M. Driedonks and H. von Dop, eds.). Dordrecht: D. Reidel), 107-158.

Caughey, S. J. and C. J. Readings, 1975: An observation of waves and turbulence in the earth's boundary layer. *Bound.-Layer Meteorol.*, **9**, 279-296.

Caughey, S. J. and J. C. Wyngaard, 1979: The turbulence kinetic energy budget in convective situations. *Quart. J. Roy. Meteorol. Soc.*, **105**, 231-239.

Charnock, H., 1957: Notes on the specification of atmospheric turbulence. *Roy. Statist. Soc. Proc.*, **A120**, 398-408.

Chen, C.-H. P. and R. F. Blackwelder, 1978: Large-scale motion in turbulent boundary layer: a study using temperature fluctuations. *J. Fluid Mech.*, **89**, 1-31.

Chiba, O. and S. Kobayashi, 1984: Turbulent characteristics of the vertical wind velocity near the critical Richardson number. Memoirs, Nat'l. Inst. of Polar Res., Tokyo, Special Issue No. 34. , 62-69.

Chimonas, G., 1985: Apparent countergradient heat fluxes generated by atmospheric waves. *Bound.-Layer Meteorol.*, **31**, 1-12.

Chu, C.-T., 1986: Parameterization of shallow convection in the boundary layer. M.S. thesis, Department of Atmospheric Sciences, Oregon State University, Corvallis, Oregon, 83 pp.

Clarke, R. H., A. J. Dyer, R. R. Brook, D. G. Reid and A. J. Troup, 1971: *The Wangara Experiment: Boundary Layer Data.* Div. Meteorol. Phys. Tech. Paper No. 19, CSIRO, Melbourne, 316 pp.

Claussen, M., 1985: Model of turbulent spectra in the atmospheric surface layer. *Bound.-Layer Meteorol.*, **33**, 151-172.

Crum, T. D., R. B. Stull, and E. W. Eloranta, 1987: Coincident lidar and aircraft observations of entrainment into thermals and mixed layers. *J. Clim. Appl. Meteorol.*, **26**, 774-788.

Dalrymple, P. C., 1966: A physical climatology of the Antarctic plateau. In *Studies in Antarctica* (M. J. Rubin, ed.). Vol. 9 of the Antarctic Research Series, American Geophysical Union, Washington, 195-231.

de Baas, A. F. and A. G. M. Driedonks, 1985: Internal gravity waves in a stably stratified boundary layer. *Bound.-Layer Meteorol.*, **31**, 303-323.

Dewan, E., 1985: On the nature of atmospheric waves and turbulence. *Radio Sci.*, **20**, 1301-1307.

Dillon, T. M. and D. R. Caldwell, 1980: The Batchelor spectrum and dissipation in the upper ocean. *J. Geophys. Res.*, **85**, 1910-1916.

Dillon, T. R., 1984: The energetics of overturning structures: implications for the theory of fossil-turbulence. *J. Phys. Oceanogr.*, **14**, 541-549.

Dutton, J. A. and D.G. Deaven, 1969: A self-similar view of atmospheric turbulence. *Radio Sci.*, **4**, 1341-1349.

Dutton, J. A., 1970: Effects of turbulence on aeronautical systems. In *Progress in Aeronautical Science*, **11** (D. Kuchemann, ed.), Pergamon Press, New York, 67-109.

Dutton, J. A. and D.G. Deaven, 1971: *Simulation of Atmospheric Turbulence with Empirical Orthogonal Functions.* Statistical properties of turbulence at the Kennedy Space Center for aerospace vehicle design. NASA Contractor Report CR-1889.

Ehrendorfer, M., 1987: A regionalization of Austria's precipitation climate using principal component analysis. *J. Climatol.*, **7**, 71-89.

Einaudi, F. and J. J. Finnigan, 1981: The interaction between an internal gravity wave and the planetary boundary layer. I. The linear analysis. *Quart. J. Roy. Meteorol. Soc.*, **107**, 793-806.

Eymard, L., 1984: Radar analysis of a tropical convective boundary layer with shallow cumulus clouds. *J. Atmos. Sci.*, **41**, 1380-1393.

Eymard, L., 1985: Convective organization in a tropical boundary layer: An interpretation of Doppler radar observations using Asai's model. *J. Atmos. Sci.*, **42**, 2844-2855.

Finnigan, J. J. and F. Einaudi, 1981: The interaction between an internal gravity wave and the planetary boundary layer. II: Effect of the wave on the turbulence structure. *Quart. J. Roy. Meteorol. Soc.*, **107**, 807-832.

Finnigan, J. J., F. Einaudi and D. Fuà, 1984: The interaction between an internal gravity wave and turbulence in the stably-stratified nocturnal boundary layer. *J. Atmos. Sci.*, **41**, 2409-2436.

Fofonoff, N. P., 1969: Spectral characteristics of internal waves in the ocean. *Deep-Sea Res. (Suppl.)*, **16**, 58-71.

Frisch, U., and P.-L. Sulem, 1978: A simple dynamical model of intermittent fully developed turbulence. *J. Fluid Mech.*, **87**, 719-736.

Frank, H., 1986: Turbulent structure in the bora and stable boundary layer. M. S. thesis, Department of Atmospheric Science, Oregon State University, Corvallis, 54 pp.

Fuà, D., G. Chimonas, F. Einaudi and O. Zeman, 1982: An analysis of wave-turbulence interaction. *J. Atmos. Sci.*, **39**, 2450-2463.

Fuelberg, H. E. and P. J. Meyer, 1984: An analysis of the AVE-SESAME I period using statistical structure and correlation functions. *Mon. Wea. Rev.*, **112**, 1562-1576.

Gage, K.S., 1979: Evidence for a $k^{-5/3}$ law inertial range in mesoscale two-dimensional turbulence. *J. Atmos. Sci.*, **36**, 1950-1954.

Gibson, C. H., 1981: Fossil turbulence and internal waves. In *Nonlinear Properties of Internal Waves* (B. J. West, ed.). American Institute of Physics, New York, 159-179.

Gibson, C. H., 1987: Fossil turbulence and intermittency in sampling oceanic mixing processes. *J. Geophys. Res.*, **92C**, 5383-5404.

Gonella, J., 1972: A rotary-component method for analyzing meteorological and oceanographic vector time series. *Deep-Sea Res.*, **19**, 833-846.

Gossard, E. E. and Hooke, 1975: *Waves in the Atmosphere*. Elsevier Scientific Publishing Company, New York, 456 pp.

Gossard, E. E., D. R. Jensen, and J. H. Richter, 1971: An analytical study of tropospheric structure as seen by high-resolution radar. *J. Atmos. Sci.*, **28**, 794-807.

Halliwell, G. R., Jr. and J. S. Allen, 1987: The large-scale coastal wind field along the west coast of North America, 1981-1982. *J. Geophys. Res.*, **92C**, 1861-1884.

Hayashi, Y., 1980: A method of estimating space-time spectra from polar-orbiting satellite data. *J. Atmos. Sci.*, **37**, 1385-1392.

Holland, J. Z., 1973: A statistical method for analyzing wave shapes and phase relationships of fluctuating geophysical variables. *J. Phys. Oceanogr.*, **3**, 139-155.

Holloway, G., 1983: A conjecture relating oceanic internal waves and small scale processes. *Atmos.–Ocean.*, **21**, 107-122.

Holtslag, A. A. M. and F. T. M. Nieuwstadt, 1986: Scaling the atmospheric boundary layer. *Bound.-Layer Meteorol.*, **36**, 201-209.

Hunt, J. C. R., 1982: Diffusion in the stable boundary layer. In *Atmospheric Turbulence and Air Pollution Modelling* (F. T. M. Nieuwstadt and H. van Dop, eds.). Dordrecht, D. Reidel, 231-274.

Hunt, J. C. R., 1985: Diffusion in the stably stratified atmospheric boundary layer. *J. Clim. Appl. Meteorol.*, **24**, 1187-1195.

Hunt, J. C. R., J. C. Kaimal, J. E. Gaynor and A. Korrell, 1985: Some observations of turbulence structure in stable layers. *Quart. J. Roy. Meteorol. Soc.*, **111**, 793-816.

Jenkins, G. M. and D. G. Watts, 1968: *Spectral Analysis and its Applications*. Holden-Day, San Francisco, 525 pp.

Kaimal, J. C. and J. A. Businger, 1970: Case studies of a convective plume and a dust devil. *J. Appl. Meteorol.*, **9**, 612-620.

Kaimal, J. C. and J. E. Gaynor, 1983: The Boulder Atmospheric Observatory. *J. Clim. Appl. Meteorol.*, **21**, 863-880.

Kaylor, R.E., 1977: *Filtering and Decimation of Digital Time Series*. Technical Note BN 850, Inst. Phys. Sci. Tech., University of Maryland, College Park, 42 pp.

Keyser, D. and T. N. Carlson, 1984: Transverse ageostrophic circulations associated with elevated mixed layers. *Mon. Wea. Rev.*, **112**, 2465-2478.

Khalsa, S. J. S., 1980: Surface layer intermittency investigated with conditional sampling. *Bound.-Layer Meteorol.*, **19**, 135-153.

Kitaigordoskii, S. A., M. A. Donelan, J. L. Lumley and E. A. Terray, 1983: Wave-turbulence interactions in the upper ocean. II: Statistical characteristics of wave and turbulent components of the random velocity field in the marine surface layer. *J. Phys. Oceanogr.*, **13**, 1988-1999.

Kolmogorov, A. N., 1941: The local structure of turbulence in compressible turbulence for very large Reynolds numbers. *Compt. Rend. Akad. Nauk SSSR*, **30**, 301-305.

Kondo, J., O. Kanechika and N. Yasuda, 1978: Heat and momentum transfers under strong stability in the atmospheric surface layer. *J. Atmos. Sci.*, **35**, 1012-1021.

Kunkel, K. E. and D. L. Walters, 1982: Intermittent turbulence in measurements of the temperature and structure parameter under very stable conditions. *Bound.-Layer Meteorol.*, **22**, 49-60.

Kushnir, Y., 1984: Subseasonal variability in a two-level atmospheric general circulation model. Ph.D. dissertation, Department of Atmospheric Sciences, Oregon State University, Corvallis, 170 pp.

Lacser, A. and S. P. S. Arya, 1986: A comparative assessment of mixing-length parameterizations in the stably stratified nocturnal boundary layer (NBL). *Bound.-Layer Meteorol.*, **36**, 53-70.

Lenschow, D. H. and P. L. Stephens, 1980: The role of thermals in the convective boundary layer. *Bound.-Layer Meteorol.*, **19**, 509-532.

Lenschow, D. H. and L. Kristensen, 1985: Uncorrelated noise in turbulence measurements. *J. Atmos. Ocean. Tech.*, **2**, 68-81.

Lesieur, M., 1983: Introduction à la turbulence bidimensionelle. In *Two-Dimensional Turbulence* (R. Moreau, ed.). *J. Méc. Théor. Appl.*, Spec., 5-20.

Levine, M.D., R. A. deSzoeke, P. P. Niiler, 1983: Internal waves in the upper ocean during MILE. *J. Phys. Oceanogr.*, **13**, 240-257.

Li, X.-S., J. E. Gaynor, and J. C. Kaimal, 1983: A study of multiple stable layers in the nocturnal lower atmosphere. *Bound.-Layer Meteorol.*, **26**, 157-168.

Lilly, D. K., 1983: Stratified turbulence and the mesoscale variability of the atmosphere. *J. Atmos. Sci.*, **40**, 749-761.

Lin, C. C., 1958: *Statistical Theories of Turbulence*. Princeton University Press, Princeton, N.J., 60 pp.

Loève, M., 1963: *Probability Theory*. D.Van Nostrand, Princeton, N.J., 685 pp.

Lorenz, E. N., 1956: Empirical orthogonal functions and statistical weather prediction. Sci. Rep. No. 1, Department of Meteorology, MIT, 49 pp.

Louis, J.-F., 1979: A parametric model of vertical eddy fluxes in the atmosphere. *Bound.-Layer Meteorol.*, **17**, 187-202.

Louis, J.-F., A. Will and D. Vidal-Madju, 1983: Dissipation length in stable layers. *Bound.-Layer Meteorol.*, **25**, 229-243.

Lu, N. and X. Li, 1985: Characteristics of wind direction fluctuations in the stable boundary layer. *Acta Meteorol. Sin.*, **43**, 35-44.

Lu, N.-P., W. D. Neff and J. C. Kaimal, 1983: Wave and turbulence structure in a disturbed nocturnal inversion. *Bound.-Layer Meteorol.*, **26**, 141-155.

Lumley, J. L., 1967: The structure of inhomogeneous flow. In *Atmospheric Turbulence and Radio Wave Propogation* (A. M. Yaglom and V. I. Tatarskii, eds.). Nauka, Moscow, 166-176.

Lumley, J. L., 1981: Coherent structures in turbulence. In *Transition and Turbulence* (R. E. Meyer, ed.). Academic, New York, 215-242.

Lumley, J. L. and H. A. Panofsky, 1964: *The Structure of Atmospheric Turbulence*. Wiley Interscience, New York, 239 pp.

Lyons, R., H. A. Panofsky and S. Wollaston, 1964: The critical Richardson number and its implications for forecast problems. *J. Appl. Meteorol.*, **3**, 136-142.

Mahrt, L., 1985: Vertical structure and turbulence in the very stable boundary layer. *J. Atmos. Sci.*, **42**, 2333-2349.

Mahrt, L., 1987: Grid-averaged surface fluxes. *Mon. Wea. Rev.*, **115**, 1550-1560.

Mahrt, L. and M. Ek, 1984: The influence of atmosphere stability on potential evaporation. *J. Cli. Appl. Meteorol.*, **23**, 222-234.

Mahrt, L. and N. Gamage, 1987: Observations of turbulence in stratified flow. *J. Atmos. Sci.*, **44**, 1106-1121.

Mahrt, L., R. C. Heald, D. H. Lenschow, B. B. Stankov and I. Troen, 1979: An observational study of the structure of the nocturnal boundary layer. *Bound.-Layer Meteorol.*, **17**, 247-264.

Mahrt, L. and H. Pan, 1984: A two-layer model of soil hydrology. *Bound.-Layer Meteorol.*, **29**, 1-20.

Mahrt, L. and J. O. Paumier, 1984: Heat transport in the atmospheric boundary layer. *J. Atmos. Sci.*, **41**, 3061-3075.

Miles, J. W., 1961: On the stability of heterogeneous shear flows. *J. Fluid Mech.*, **10**, 496-508.

Miles, J. W., 1987: Richardson's number revisited. In Preprints, Third International Symposium on Stratified Flows, California Institute of Technology, General Session, Pasadena, Calif.

Mooers, C. N. K., 1973: A technique for cross spectrum analysis of pairs of complex-valued time series, with emphasis on properties of polarized components and rotational invariants. *Deep-Sea Res.*, **20**, 1129-1141.

Müller, P., 1984: Small scale vertical motion. In *Proceedings, 'Aha Huliko'a Hawaiian Winter Workshop* (P. Müller and R. Pujalet, eds.). University of Hawaii, Manoa, 249-261.

Müller, P., G. Holloway, F. Henyey and N. Pomphrey, 1986: Nonlinear interactions among internal gravity waves. *Rev. Geophys.*, **24**, 493-536.

Mumford, J. C., 1982: The structure of the large eddies in fully developed turbulent shear flows. Part I. The plane jet. *J. Fluid Mech.*, **118**, 241-268.

Nieuwstadt, F. T. M., 1984: The turbulent structure of the stable, nocturnal boundary layer. *J. Atmos. Sci.*, **41**, 2202-2216.

O'Brien, J. J. and R. D. Pillsbury, 1974: Rotary wind spectra in a sea breeze regime. *J. Appl. Meteorol.*, **13**, 820-825.

Oke, T. R., 1978: *Boundary Layer Climates.* Metheun, London, 372 pp.

Orlanski, I., 1975: A rational subdivision of scales for atmospheric processes. *Bull. Amer. Met. Soc.*, **56**, 527-530.

Pan, H.-L., 1987: Modelling the snow cover. In *Boundary Layer Parameterization for a Global Spectral Model* (L. Mahrt, H.-L. Pan, P. Ruscher, C.-T. Chu, and K. Mitchell). Final contract report to Air Force Geophysics Laboratory, Department of Atmospheric Sciences, Oregon State University, Corvallis, 144-147.

Pan, H.-L. and L. Mahrt, 1987: Interaction between soil hydrology and boundary-layer development. *Bound.-Layer Meteor.*, **38**, 185-202.

Panofsky, H. A. and G. W. Brier, 1968: *Some Applications of Statistics to Meteorology*. Pennsylvania State University Press, University Park, Pennsylvania, 224 pp.

Panofsky, H. A. and J. A. Dutton, 1984: *Atmospheric Turbulence*. John Wiley & Sons, New York, 397 pp.

Petersen, E. L., 1976: A model for the simulation of atmospheric turbulence. *J. Appl. Meteorol.*, **15**, 571-587.

Portman, D. J., F. C. Elder, E. Ryznar and V. E. Noble, 1962: Some optical properties of turbulence in stratified flow near the ground. *J. Geophys. Res.*, **67**, 3223-3235.

Pratt, R. W., 1976: The interpretation of space-time spectral quantities. *J. Atmos. Sci.*, **33**, 1060-1066.

Richman, M. B., 1986: Rotation of principal components. *J. Climatol.*, **6**, 293-335.

Riley, J. J., R. W. Metcalfe and M. A. Weissman, 1981: Direct numerical simulations of homogeneous turbulence in density-stratified fluids. In *Nonlinear Properties of Internal Waves* (B. J. West, ed.). American Institute of Physics, New York, 79-112.

Schols, J. L. J., 1984: The detection and measurement of turbulent structures in the atmospheric surface layer. *Bound.-Layer Meteorol.*, **29**, 39-58.

Schols, J. L. J. and L. Wartena, 1986: A dynamical description of turbulent structures in the near neutral atmospheric surface layer: The role of static pressure fluctuations. *Bound.-Layer Meteorol.*, **34**, 1-15.

Shaw, W.J., 1983: Intermittency and the organization of turbulence in the near-neutral marine atmospheric boundary layer. In *Ext. Abs., Sixth Symposium on Turbulence and Diffusion*. American Meteorological Society, Boston, 356-359.

Shirer, H. N., 1986: On cloud street development in three dimensions: parallel and Rayleigh instabilities. *Beitr. Phys. Atmos.*, **59**, 126-149.

Sommeria, G., 1987: Parameterization of the planetary boundary layer in large-scale atmospheric models. To appear in *Physically-Based Modelling and Simulation of Climate and Climatic Change* (M. E. Schlesinger, ed.). D. Reidel, NATO ASI series, Dordrecht.

Sorbjan, Z., 1987: An examination of local similarity theory in the stably stratified boundary layer. *Bound.-Layer Meteorol.*, **38**, 63-71.

Stewart, R. W., 1969: Turbulence and waves in a stratified atmosphere. *Radio Sci.*, **4**, 1269-1278.

Tanaka, H., 1975: Turbulent layers associated with a critical level in the planetary boundary layer. *J. Meteor. Soc. Japan*, **53**, 425-438.

Tennekes, H. and J. L. Lumley, 1972: *A First Course in Turbulence*. MIT Press, Cambridge, Mass., 300 pp.

Thorpe, A. J. and Guymer, 1977: The nocturnal jet. *Quart. J. Roy. Meteorol. Soc.*, **103**, 633-654.

Thorpe, S. A., 1973: Turbulence in stratified fluids: a review of laboratory experiments. *Bound.-Layer Meteorol.*, **5**, 95-119.

Townsend, A. A., 1976: *The Structure of Turbulent Shear Flows* (Second Edition). Cambridge University Press, 429 pp.

Troen, I. and L. Mahrt, 1986: A simple model of the atmospheric boundary layer: Sensitivity to surface evaporation. *Bound.-Layer Meteorol.*, **37**, 129-148.

Turner, J. S., 1979: *Buoyancy Effects in Fluids* (Revised Edition). Cambridge University Press, 368 pp.

Vincent, D. G. and J. H. Homan, 1983: Mesoscale analysis of pressure and precipitation patterns during AVE-SESAME 1979, 10-11 April. *Bull. Amer. Meteorol. Soc.*, **64**, 23-28.

Wallace, J. M. and R. Dickinson, 1972: Empirical orthogonal representation of time series in the frequency domain. I: theoretical considerations. *J. Appl. Meteorol.*, **11**, 887- 892.

Webb, E. K., 1970: Profile relationships: The log-linear range, and an extension to strong stability. *Quart. J. Roy. Meteorol. Soc.*, **96**, 67-90.

Weinstock, J., 1984: Effect of gravity waves on turbulence decay in stratified fluids. *J. Fluid Mech.*, **140**, 11-26.

Wilczak, J.M., 1982: A study of the dry convective atmospheric boundary and surface layers. Ph.D. dissertation, Department of Atmospheric Sciences, University of Washington, Seattle, 228 pp.

Woods, J.D., V. Högström, P. Misme, H. Ottersten and O.M. Phillips, 1969: Fossil turbulence. *Radio Sci.*, **4**, 1365-1367.

Wratt, D. S. and L. F. Homes, 1984: Measurements on a thirty-meter tower at the New Zealand synthetic fuels corporation plant, Motunni, with applications to atmospheric dispersion. *Sci. Rept. N. Zea. Met. Serv.*, 70 pp .

Wyngaard, J. C., W. T. Pennell, D. H. Lenschow and M. A. LeMone, 1978: The temperature-humidity covariance budget in the convective boundary layer. *J. Atmos. Sci.*, **35**, 47-58.

Zhou, M. Y., D. H. Lenschow, B. B. Stankov, J. C. Kaimal and J. E. Gaynor, 1985: Wave and turbulence structure in a shallow baroclinic convective boundary layer and overlying inversion. *J. Atmos. Sci.*, **42**, 47-57.

Appendix

Table A.1

SESAME NBL Flight 3 (5 May 1979) — Level Legs

leg	time (CDT) start	time (CDT) end	tape time (sec.) start	tape time (sec.) end	height (m) start	height (m) end	aircraft heading
1	5:38:32	5:41:40	20312	20500	75.	84.	South
2	5:41:41	5:44:58	20501	20698	85.	67.	South
3	5:48:30	5:51:05	20910	21065	78.	56.	South
4	5:53:32	5:55:40	21212	21340	69.	64.	North
5	5:58:01	6:01:15	21481	21675	77.	71.	South
6	6:03:30	6:06:20	21810	21980	39.	71.	North
7	6:07:52	6:11:00	22072	22260	74.	42.	South
8	6:22:42	6:25:20	22962	23120	21.	19.	North
9	6:27:12	6:30:20	23232	23420	62.	55.	South
10	6:41:50	6:44:40	24110	24280	18.	17.	North
11	7:02:30	7:05:50	25350	25550	40.	40.	South
12	7:15:60	7:17:20	26160	26240	68.	97.	South

Table A.2

SESAME NBL Flight 3 (5 May 1979) — Slant Legs

leg	time (CDT) start	time (CDT) end	tape time (sec.) start	tape time (sec.) end	height (m) start	height (m) end	aircraft heading
1	5:36:20	5:38:32	20180	20312	286.	75.	South
2	5:47:50	5:50:17	20870	21017	134.	52.	South
3	5:51:05	5:51:50	21065	21110	56.	100.	South
4	6:02:55	6:03:28	21775	21808	160.	38.	North
5	6:12:25	6:13:16	22345	22396	129.	15.	North
6	6:13:17	6:13:44	22397	22424	15.	96.	North
7	6:13:45	6:14:37	22425	22477	95.	14.	North
8	6:14:38	6:15:01	22478	22501	14.	99.	North
9	6:15:02	6:15:35	22502	22535	97.	19.	North
10	6:17:20	6:18:33	22640	22713	163.	14.	South
11	6:18:34	6:19:43	22714	22783	13.	169.	South
12	6:19:44	6:20:30	22784	22830	167.	15.	South
13	6:31:60	6:33:19	23520	23599	240.	14.	North
14	6:33:20	6:34:51	23600	23691	16.	236.	North
15	6:35:50	6:36:42	23750	23802	187.	17.	South
16	6:36:43	6:38:06	23803	23886	18.	228.	South
17	6:38:07	6:39:24	23887	23964	226.	15.	South
18	6:41:00	6:41:50	24060	24110	198.	18.	North
19	6:46:31	6:47:53	24391	24473	231.	15.	South
20	6:47:54	6:49:54	24474	24594	15.	241.	South
21	6:52:55	6:54:20	24775	24860	227.	16.	North
22	6:54:21	6:56:01	24861	24961	18.	227.	North
23	6:56:02	6:57:42	24962	25062	228.	22.	North
24	6:57:44	6:58:50	25064	25130	17.	146.	North
25	7:00:43	7:02:30	25243	25350	143.	40.	South
26	7:08:03	7:09:23	25683	25763	174.	18.	North
27	7:09:25	7:10:34	25765	25834	20.	234.	North
28	7:10:35	7:12:07	25835	25927	234.	46.	North
29	7:12:25	7:13:48	25945	26028	21.	219.	North
30	7:14:60	7:15:60	26100	26160	235.	68.	South
31	7:17:04	7:17:49	26224	26269	46.	152.	South
32	7:18:51	7:19:33	26331	26373	129.	48.	South
33	7:19:38	7:20:30	26378	26430	48.	156.	South
34	7:20:31	7:21:26	26431	26486	155.	20.	South
35	7:23:31	7:25:00	26611	26700	184.	15.	North
36	7:25:01	7:26:18	26701	26778	15.	229.	North
37	7:26:19	7:27:50	26779	26870	229.	16.	North
38	7:27:51	7:29:30	26871	26970	14.	227.	North
39	7:31:07	7:33:03	27067	27183	225.	26.	South
40	7:33:06	7:34:09	27186	27249	26.	224.	South
41	7:34:12	7:35:23	27252	27323	225.	12.	South
42	7:35:24	7:37:00	27324	27420	12.	233.	South
43	7:38:12	7:40:08	27492	27608	225.	14.	North
44	7:40:13	7:41:47	24613	27707	14.	243.	North
45	7:41:48	7:42:30	27708	27750	243.	135.	North

Table A.3

Flight 3 Level Leg Segment Times and Locations

leg	times	latitude	longitude
1	20312/20500	35.10/34.98	-98.3
2	20501/20698	34.98/34.85	"
3	20910/21110	34.77/34.63	"
4	21212/21340	34.62/34.71	-98.29
5	21481/21675	34.76/34.63	-98.3/-98.29
6	21810/21980	34.64/34.74	-98.29/-98.3
7	22072/22260	34.76/34.64	-98.29/-98.3
8	22962/23120	34.63/34.73	-98.29/-98.3
9	23232/23420	34.76/34.64	-98.29/-98.3
10	24110/24280	34.64/34.74	-98.3
11	25350/25550	34.74/34.61	-98.27
12	26160/26240	34.79/34.74	-98.26

Table A.4

Flight 3 Slant Leg Segment Times and Locations

leg	times	latitude	longitude
1	20180/20312	35.20/35.11	-98.31
2	20870/21017	34.80/34.70	-98.30
3	21065/21110	34.66/34.63	-98.30/-98.29
4	21775 21808	34.61/34.63	-98.28/-98.29
5	22345/22396	34.62/34.65	-98.29
6	22397/22424	34.65/34.67	"
7	22425/22477	34.67/34.71	-98.29/-98.3
8	22478/22501	34.71/34.72	-98.3
9	22502/22535	34.72/34.74	"
10	22640/22713	34.76/34.71	"
11	22714/22783	34.71/34.67	"
12	22784/22830	34.67/34.64	" /-98.29
13	23520/23599	34.62/34.68	-98.29/-98.3
14	23600/23691	34.68/34.73	-98.3
15	23750/23802	34.76/34.74	-98.31/-98.3
16	23803/23886	34.74/34.69	-98.3
17	23887/23964	34.69/34.64	"
18	24060/24110	34.61/34.65	-98.28/-98.3
19	24391/24473	34.76/34.71	-98.3
20	24474/24594	34.71/34.64	-98.3/-98.28
21	24775/24860	34.60/34.66	-98.27
22	24861/24961	34.66/34.72	-98.27
23	24962/25062	34.72/34.79	-98.27
24	25064/25130	34.79/34.83	"
25	25243/25350	34.81/34.73	"
26	25683/25763	34.60/34.65	"
27	25765/25834	34.65/34.69	-98.27/-98.26
28	25835/25927	34.69/34.75	-98.26
29	25945/26028	34.76/34.81	-98.26
30	26100/26160	34.83/34.78	"
31	26224/26269	34.75/34.72	"
32	26331/26373	34.68/34.65	-98.26/-98.25
33	26378/26430	34.65/34.62	"
34	26431/26486	34.62/34.58	"
35	26611/26700	34.57/34.63	-98.27
36	26701/26778	34.63/34.68	"
37	26779/26870	34.68/34.74	"
38	26871/26970	34.74/34.80	"
39	27067/27183	34.81/34.73	"
40	27186/27249	34.73/34.70	"
41	27252/27323	34.70/34.65	-98.26/-98.27
42	27324/27420	34.65/34.60	-98.27/-98.26
43	27492/27608	34.58/34.66	-98.26
44	24613/27707	34.67/34.72	-98.27
45	27708/27750	34.72/34.75	-98.27/-98.26